THE FEASIBILITY OF USING MgF_2 FOR PHASE CHANGE HEAT STORAGE IN A SPACECRAFT SOLAR THERMAL POWER SYSTEM

by

CHARLES ALAN LURIO

S.M., Massachusetts Institute of Technology (1983)
S.B., Massachusetts Institute of Technology (1980)

Submitted to the Department of Aeronautics and Astronautics
in partial fulfillment of the requirements for the degree of

DOCTOR OF PHILOSOPHY
at the
MASSACHUSETTS INSTITUTE OF TECHNOLOGY
July, 1988

Signature of Author _____
Department of Aeronautics and Astronautics
July 22, 1988

Certified by _____
Professor Manuel Martinez-Sanchez, Thesis Supervisor
Professor of Aeronautics and Astronautics

Certified by _____
Professor John F. Elliott
Professor of Materials Science and Engineering

Certified by _____
Professor René H. Miller
Professor of Aeronautics and Astronautics, Emeritus

Accepted by _____
Professor Harold Y. Wachman
Chairman, Departmental Graduate Committee

THE FEASIBILITY OF USING MgF_2 FOR PHASE CHANGE HEAT STORAGE IN A SPACECRAFT SOLAR THERMAL POWER SYSTEM

by

CHARLES ALAN LURIO

Submitted to the Department of Aeronautics and Astronautics on July 22, 1988
in partial fulfullment of the requirements for the
Degree of Doctor of Philosophy in Aeronautics and Astronautics

ABSTRACT

For spacecraft operating in Low Earth Orbit (LEO) electrical power can be provided with lowered mass and drag area by the use of solar thermal dynamic rather than photovoltaic power conversion. The dynamic systems require a means of storing heat for operation during the eclipse portion of the orbit and past studies have selected LiF (melting point 1121°K) to provide such storage using heat of fusion.

A comparison shows that the use of MgF_2 (melting point 1536°K) instead will reduce the power system mass by about 16% and solar collector drag area by 22% due to increased energy conversion efficiency. A theoretical evaluation shows that MgF_2 should be compatible with refractory metals. While water contamination of the fluoride (100 ppm) can cause high initial pressures (up to 19 atm for Ta) in sealed containers, H_2 diffusion should result in final pressures well below one atmosphere.

The compatibility of molten MgF_2 with ASTAR 811-C (Ta-8W-1Re-0.7Hf-.025C) and W-25Re test capsules was tested for 2089 hours in a vacuum furnace ($\sim 10^{-6}$ torr). Metallographic and other tests showed no deterioration of the latter alloy. The ASTAR capsule wall was nearly penetrated by MgF_2 at isolated points due to contamination by Fe embedded in the wall during manufacture. Particles (~1 μm size) containing 71% Hf and none of the other metals available were found scattered throughout the frozen MgF_2 in the ASTAR container.

Corollary tests showed MgF_2 supercooling of ~10-30°K and ~50-90°K in the W-25Re and ASTAR 811C containers respectively.

Thesis Supervisors:

Professor Manuel Martinez-Sanchez (Chairman)
Associate Professor of Aeronautics and Astronautics

Professor John F. Elliott
Professor of Materials Science and Engineering

Professor René H. Miller
Professor of Aeronautics and Astronautics, Emeritus

Professor Harold Y. Wachman
Professor of Aeronautics and Astronautics

ACKNOWLEDGEMENTS

The work described here would not have been possible without the unfailing encouragement, assistance and understanding of Professor Manuel Martinez-Sanchez. I cannot imagine a better mentor.

Professor John Elliott provided invaluable guidance in the theoretical and practical aspects of materials science. Professor René Miller has given crucial support and direction during this project and over all the years I have spent in this department. Professor Harold Wachman's observations resulted in a much improved focus for this work.

Outside of MIT, the Oak Ridge National Laboratory provided both advice and material assistance. My particular gratitude goes to Mr. Jack DeVan, who patiently guided me through the intricacies of refractory metals over many long phone conversations. I am also grateful for the financial support provided for the first three years of this project by the NASA Lewis Research Center.

It is impossible to express the degree of thanks owed to my parents and family. Their unstinting help was the prerequisite to all that was accomplished.

I wish also to thank my friends, both at and away from MIT, who provided a steady reminder that research is not the start and finish of life. A few names should be cited (without implying lack of recognition of those omitted): Finley Shapiro, Lynne Haber, Dan Goodman, Elana Doering, Jean Sorber, Janine Adler and Rafi Sacks of the basement minyan; Dave Akin, Mary Bowden, Russ Howard and Dave Stuart of the Space Systems Laboratory:'the Harvard group', particularly Mark and Erica; George and Judith Whittinghill, 'Blackjack' Dan, Bill Lane, Kevin Nelson and Wayne Jefferson. In addition, I am grateful to Eric, Alex, Knox, Rodger, Sabri and others for willingly suffering permanent hearing loss for the advance of Science.

The MIT staff provided essential help during the experimental work. Some also gave particular encouragement: Paul Bauer, Don Wiener and Al Shaw.

TABLE OF CONTENTS

CHAPTER 1

BACKGROUND AND SYSTEMS LEVEL MOTIVATIONS

1.1 Introduction

Provision of sufficient electrical power for spacecraft operations is a major concern for the vehicle designer. The classical answer to this problem for the vast majority of spacecraft has been the use of silicon solar cell arrays with batteries for providing power when sunlight is unavailable. Exceptions to this rule have occurred in a few instances: spacecraft traveling to the outer solar system (where solar intensity is greatly reduced); equipment placed where sunlight is absent for long periods (the Apollo lunar surface experiments); and vehicles requiring high power in a small package (Soviet military radar satellites).

All of the exceptions noted above have relied upon nuclear heat sources and solid state energy conversion devices with efficiencies well under 10%. This has reflected a "no moving parts" approach to reliability. As power requirements increase, however, there is increased motivation to use a higher efficiency energy system. There is also widespread public fear of nuclear-based systems.

The proposed NASA space station would operate for 30 years in a Low Earth Orbit (LEO) and provide 75-300 kW of electrical power [1]†. In LEO, sunlight is available for about two-thirds of a ninety minute orbit, the rest of the time being spent in Earth's shadow. Also, at such altitudes, (200-300 miles), drag caused by large area solar arrays translates into increased fuel requirements for orbital maintenance. Alternatively, one could place the

†*Bracketed numbers refer to references; see list following final chapter.*

station at a somewhat higher altitude to start with, where drag is reduced; however, the payloads that can be carried to a higher orbit are lower.

There are alternatives to using either solar arrays or nuclear systems. These are the so-called solar-dynamic systems. Solar energy is collected by a mirror, concentrated, and used to heat a working fluid (liquid or gas). This fluid may be used to run a turbine (Brayton or Rankine cycles) or other heat engine (Stirling cycles), which in turn drives a generator. Like solar arrays, solar dynamic systems require some form of energy storage for the shadow portion of the orbit. Shutting down and restarting the thermal engine during each orbit may accelerate mechanical wear. The system could be kept running if some form of heat storage were used.

One possible method of such storage is to use the heat released when a substance undergoes a temperature change (sensible heat). However, a generally more effective method (on the basis of J/kg) which, also, is ideally isothermal, is to use heat liberated with phase change [2]. Heat of fusion (liquid to solid) is preferred over heat of vaporization due to the much smaller volume change that occurs with the former.

Figure 1.1 shows schematically the application of this method to an orbital power system. While in sunlight ("insolation"), heat gathered not only runs the heat engine, but also melts the heat storage material; during shadow this material freezes, releasing heat that allows the engine to continue operating.

The present work is concerned with examining the feasibility and desirability of using Magnesium Fluoride (MgF_2) as the phase change heat storage material in a space solar dynamic power system. This chapter

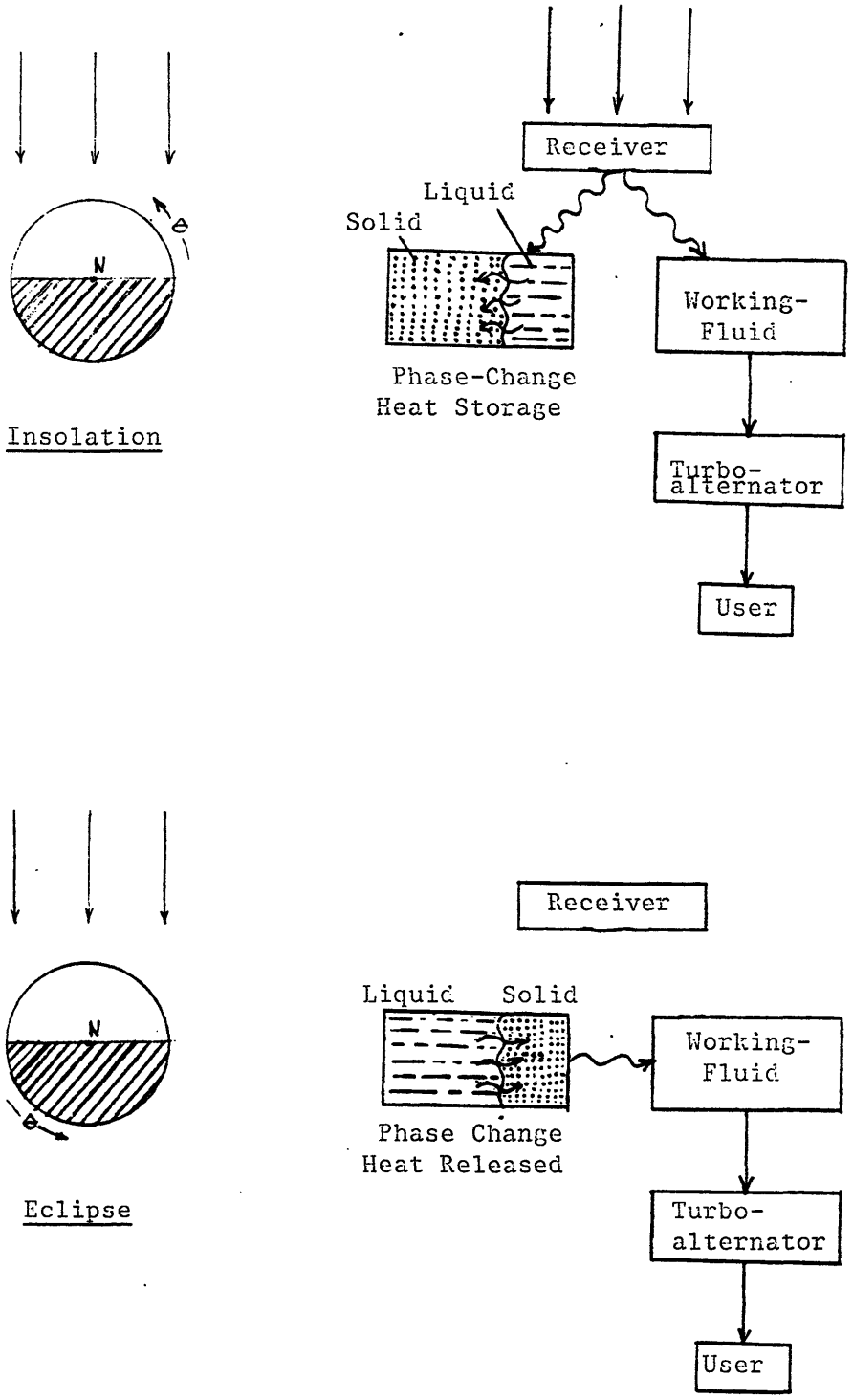

Figure 1.1 Solar Thermal Power System Operations Schematic

considers the systems level consequences of using MgF_2. Subsequent chapters describe the results of theoretical and experimental work. Finally, the consequences of these results are examined.

1.2 Solar Dynamic Versus Photovoltaic Power

It is illuminating to briefly consider a numerical comparison of photovoltaic and solar dynamic power systems. The basis of this comparison shall be a total orbit efficiency defined as

$$\eta_{tot} = \frac{\text{total energy used over orbit}}{\text{total solar energy input over orbit}} \tag{1.1}$$

where for both photovoltaic and solar dynamic systems, this may be restated as

$$\eta_{tot} = \frac{P_L(t_{sun} + t_{sh})}{P_s t_{sun}} \tag{1.2}$$

with

P_L = constant user power demand, kW

P_s = input of solar energy during insolation (kW)

t_{sun} = orbital time in sunlight, min.

t_{sh} = orbital time in shadow, min.

Now, for the photovoltaic and solar dynamic systems respectively, the following power balances may be defined, for the insolation period:

$$P_s \eta_A = P_L\left(1 + \frac{t_{sh}}{t_{sun}} \frac{1}{\eta_{sto}}\right) \tag{1.3a}$$

$$P_s \eta_e \eta_c = P_L\left(1 + \frac{t_{sh}}{t_{sun}} \frac{1}{\eta_{sto}}\right) \tag{1.3b}$$

where

η_A = array energy conversion efficiency

η_e = combined thermal/alternator conversion efficiency

η_c = solar energy collection efficiency

η_{sto} = energy storage efficiency

In Table 1.1, storage and conversion efficiencies have been gathered from a variety of sources as noted. The total orbital efficiencies are from combining equations (1.2), (1.3) to find

$$\eta_{tot} = \begin{cases} \left[\dfrac{t_{sun} + t_{sh}}{t_{sun} + \dfrac{t_{sh}}{\eta_{sto}}}\right]\eta_A & (1.4a) \\ \left[\dfrac{t_{sun} + t_{sh}}{t_{sun} + \dfrac{t_{sh}}{\eta_{sto}}}\right]\eta_e\eta_c & (1.4b) \end{cases}$$

for photovoltaic and solar dynamic systems respectively. Where a range is given in the table, the indicated intermediate values were used in the calculation of η_{tot}. The value of η_{tot} will be inversely proportional to the required mirror or array area and thus to the atmospheric drag. The value of solar dynamic coversion efficiency used is conservative.

1.3 Background of Solar Dynamic Systems

As pointed out by Baraona [7], the idea of using solar dynamic power generation in space well antedates the flight of *Sputnik 1* in 1957. During the early 1960s both NASA and the Department of Defense (DOD) carried out research under the Sunflower and ASTEC programs respectively [4]. In parallel, through the '60s, extensive work was done on turbogenerators for

Table 1.1

Total Orbit Efficiencies (η_{tot}) of Space Power Systems

		Silicon	GaAs	Solar Dynamic
	Conversion η (%)	7–22	12–24 (2)	20–45 (3)
	Storage η (%)	16* (1)	20*	30*
Regenerative fuel cells	62 (4)	13	17	
N_i-C_d Battery	77 (5)	15	18	
N_i-H_2 Battery	79 (6)	15	18	
Flywheels	85 (7)	15	19	
Phase-change heat storage	90 (8)			23

Solar dynamic collection efficiency η_{co} = .8 from [3].

NOTES:

(1) low value from [4]; others from a survey of papers in [5]

(2) same as note (1)

(3) low value from [4]

(4) [6], Table 2, pg. 37

(5) [1], derived from Table 2.2.3-10, p. 2-66

(6) [1], Table 3.2.9, p. 3-45

* *indicates actual value used*

application to space nuclear reactors (such as the SNAP-8 90 kW_e mercury rankine device [8]).

Brayton cycle technology work was carried out by NASA, resulting in the fabrication of the solar receiver unit illustrated in Figures 1.2a, b, c, and used lithium fluoride (LiF) for thermal storage [9]. That compound, which melts at 1121°K, was contained in corrugated tubes concentric with the cycle working gas tubes. The purpose of the corrugations was to minimize fluid redistribution in zero-g, which was a potential problem due to the approximately 30% shrinkage of LiF on freezing. It is necessary that there be a larger amount of LiF where the "cold" gas enters the receiver than at the gas exit. The larger ΔT between gas and LiF at the start causes a greater heat flux so a larger heat reservoir is required.

The LiF storage receiver program had included tests of the compatibility of LiF with several alloys over 5000 hrs. including cycling through the melting point [12]. While the project was shut down before the full receiver could be tested, three receiver tubes did undergo limited testing in simulated operating conditions [10].

By the mid to late 1960s (as shown in [4]) space solar dynamic work had nearly halted. There was some development of the Brayton Isotope Power System (BIPS) which uses nuclear decay heat to run a cycle instead of operating thermoelectric conversion devices. Also, very large thermal engines (hundreds of MW) were studied in connection with the various Solar Power Satellite (SPS) studies.

In private industry since the 1960s, there has been considerable experience with solar driven Organic Rankine Conversion (ORC). These ORC

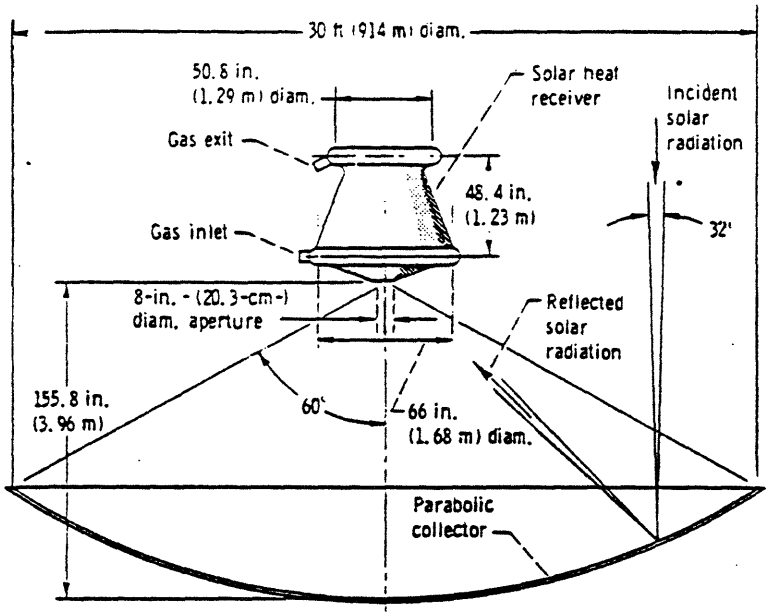

(a) Solar heat receiver, solar collector combination.

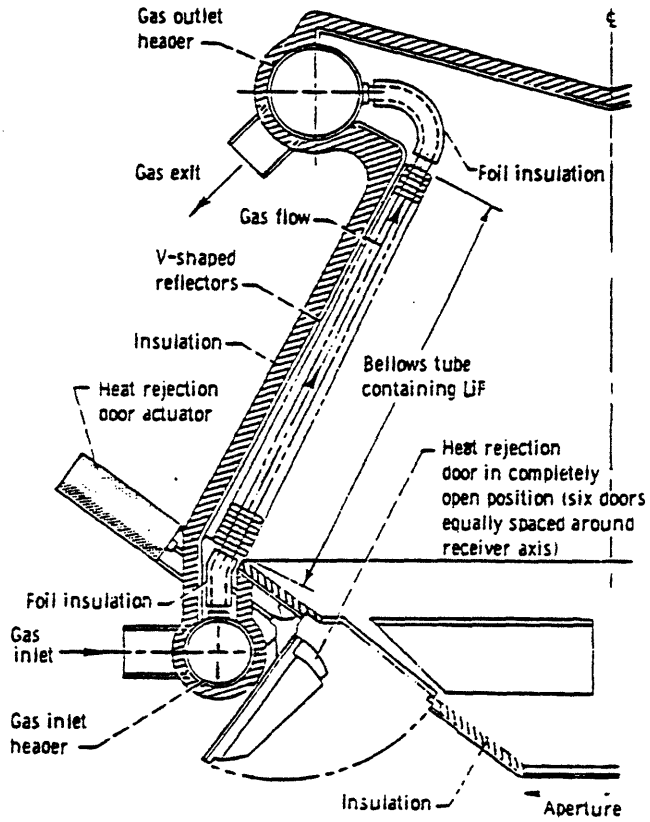

(b) Solar heat receiver cross section.

Figure 1.2a Solar Brayton System, LiF Heat Storage [11]

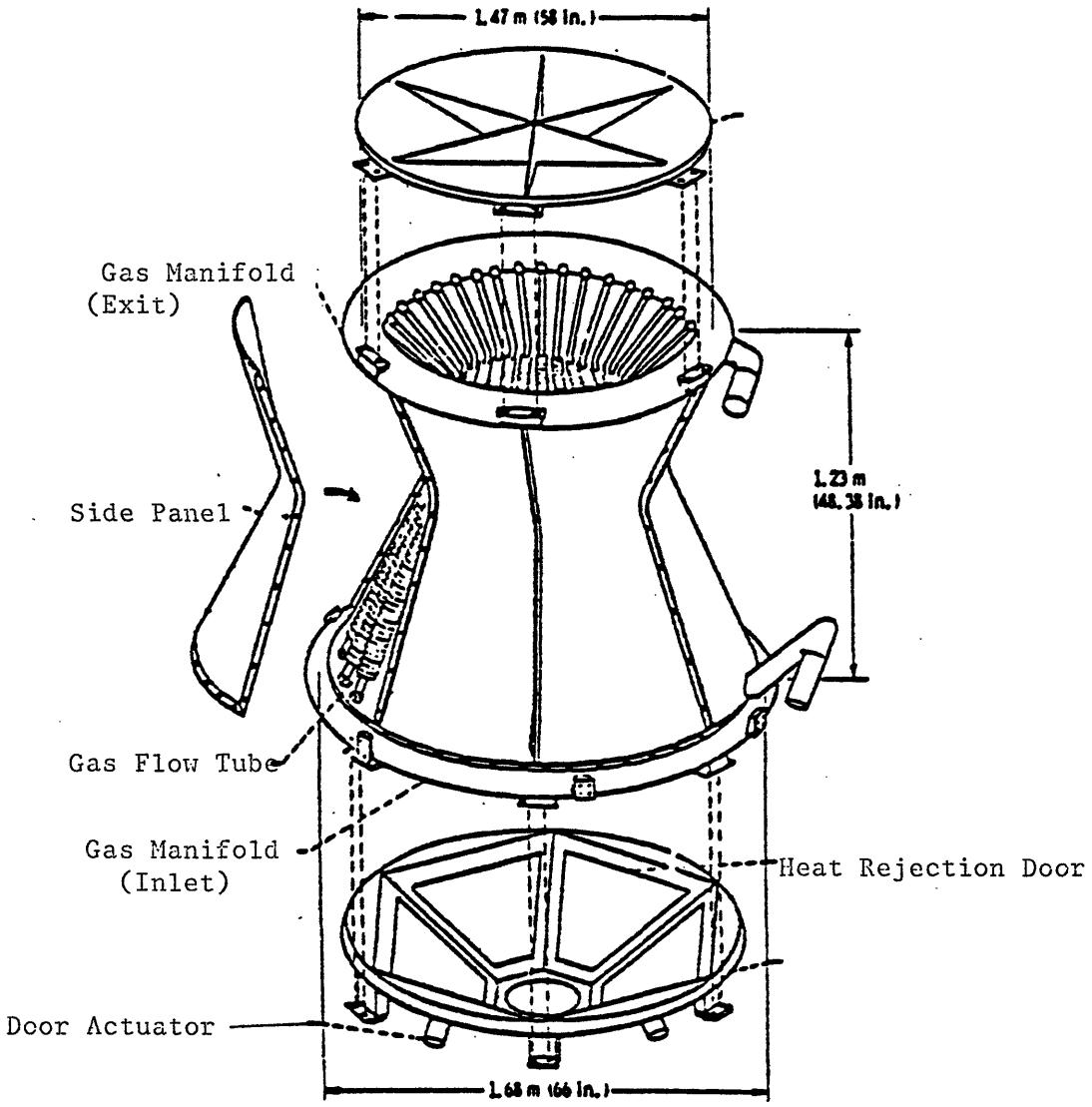

Figure 1.2b Exploded View of Receiver, LiF Heat Storage System

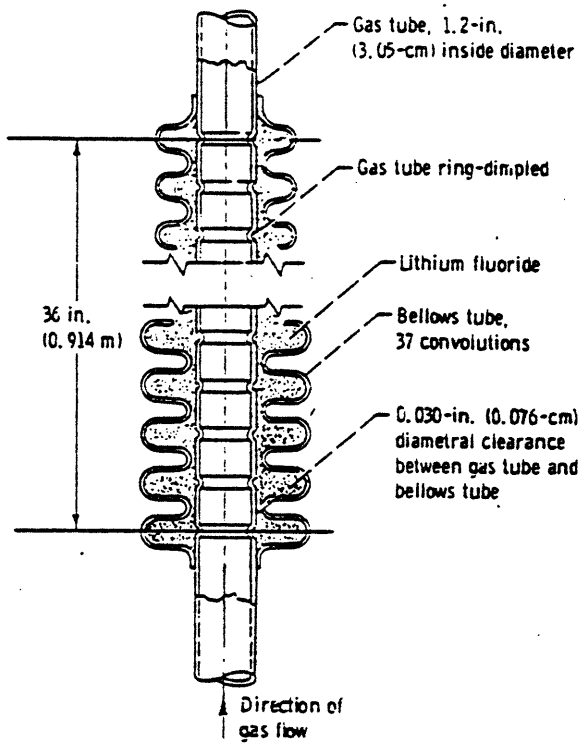

Figure 1.2c Cross Section of Gas Tube and LiF Heat Storage Material

units use a carbon-based working fluid, generally toluene, and have a relatively low peak temperature (~ 700°K, [1]-Table 3.3.2.2-2). They often have been installed in remote sites where they reliably produce a few kilowatts power.

With the revival of space station work in the 1980s, NASA and its contractors have considered solar dynamic systems for the reasons noted earlier. The highest temperature system included in this work has generally been limited by the melting point of LiF; however, recently some research has been done on fluoride mixtures with melting points to 1400°K [13].

1.4 Selection of MgF_2

Several years ago, the author began investigating the use of phase change thermal storage materials with melting points above that of lithium fluoride. The motivation for this was the potential for higher engine cycle efficiencies. Beside melting point, energy per unit mass (J/kg) is an important parameter. Considering the data for these two quantities (shown in Figure 1.3) silicon was selected for further study. The work performed in [14] and [15] showed a favorable result for the specific mass of solar dynamic systems using silicon when compared to solar array systems.

Subsequent to this, a wider survey of information showed that molten silicon was unlikely to be containable for long periods in any material. In particular, an experiment at General Electric several years before had shown that containment in silicon carbide (which had been postulated in [14]) was not possible [16].

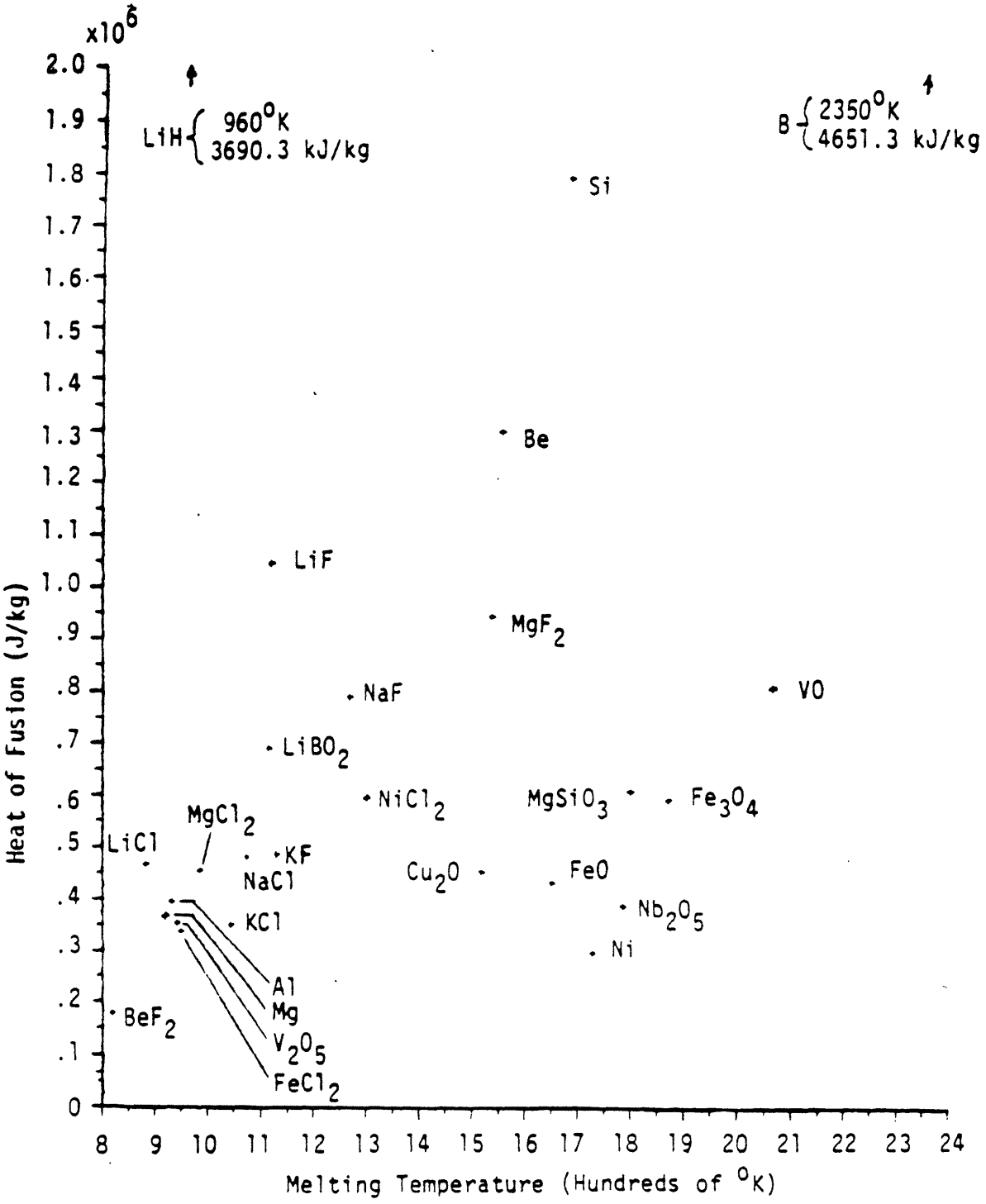

Figure 3 Heat of Fusion versus Melting Temperature

In searching for a replacement storage material it was clear that one would not wish to much exceed the melting point of Si due to increasing difficulty of containment. It was also desired that a reasonably safe material for compatability tests be chosen. Thus, looking at the possibilities shown in Figure 1.3, MgF_2 was chosen for further research over others such as Be.

Considerable effort was expended looking into what was known about the material. Persons at MIT and Oak Ridge National Laboratory (ORNL) familiar with fluoride chemistry indicated that it was likely to be stable and containable. Literature searches showed relatively sparse data. Particularly useful were the compilations by Eichelberger and Janz [17], [18] which listed previously published corrosion tests. An important source of thermodynamic quantities were the Joint Army, Navy, Air Force (JANAF) data tables [19] and the compilations by Barin (referenced later).

Table 1.2 summarizes some important properties of MgF_2 for comparison with those of LiF. MgF_2 requires slightly less heat of fusion than LiF but has a smaller volume change when melting, which should reduce receiver design difficulties. Unfortunately, no data is available on thermal conductivity of the liquid or that of the solid at the melting point. Nor does data exist on surface tension, although Eichelberger states that generally fluorides "creep and flow easily" due to a combination of viscosity, wetting, and surface tension effects (p. 190).

1.5 Mass and Drag Area Comparison of LiF and MgF_2 Power Systems

This section considers an explicit comparison of mass and drag area for two 100 kW_e power systems, one using LiF heat storage and the other MgF_2, with

Table 1.2

Properties Comparison of MgF_2 and LiF

PROPERTY	MgF_2		LiF	
Molecular weight gm/mole	62.30		24.94	
Melting point °K	1536 ± 5°K	*(1)*	1121 ± 1°K	(2)
Heat of fusion J/kg	0.94×10^6 ± 7%	(3)	1.050×10^6 ± 0.8%	(4)
Density ρ of liquid at melting point (kg/m^3)	2430 ± 1%	(5)	1810	(6)
Volume change on melting, % $(\Delta V/V_s)_{T_m}$	14.0 ± 1.12	*(7)*	~ 30	(8)
Thermal Conductivity W/m - °K	(~2.9 at 1536°K (s))	(9)	(~5.3 at 1121°K (s))	*(10)*

NOTES:

(1), (2), (3), (4) [19]

(5) [18]

(6) [17] no error bar given

(7) [19]

(8) [12] no error bar given

(9) Extrapolated from data referenced in [17] (see Appendix A) on solid MgF_2, "mean values" of data given

(10) Extrapolated from data referenced in [17] (see Appendix A) for solid, accuracy ± 10%

common design assumptions. The purpose is not to produce a "global" optimum for each system, though some optimization is performed. Rather, it is to illustrate some of the consequences of using the higher temperature system.

1.5.1 Collector-Receiver (Collection) System Energy Optimization

As Jaffe points out in [3], the optimization of the collector mirror and receiver cavity can only be done in tandem, as they are directly coupled. He optimizes net energy collection efficiency to the receiver during insulation for ground based systems. The model used here follows his except for modifications appropriate to space based systems.

The problem of the energy balance for the collection system is shown in Figure 1.4. The ideal paraboloid mirror is perfectly aligned with the sun, has no error in surface slope or specularity, and is perfectly reflective. The ideal receiver is perfectly insulated and sunlight enters through an infinitely small hole so that no heat may escape there. This requires an "ideal sun" subtending zero degrees of arc whose image is formed in the focal plane at the receiver entrance.

With "non-ideal" surfaces, alignment, and sun, an extended image is formed on the focal plane, and one may consider what receiver aperture radius (or area A_r) results in the largest net heat input. There are also non-unity values of mirror reflectivity and receiver absorbtivity, and the receiver blocks some part of the incoming light to the mirror. There is radiative loss out the aperture and, for a space system, radiative loss from the receiver walls is the only other significant loss.

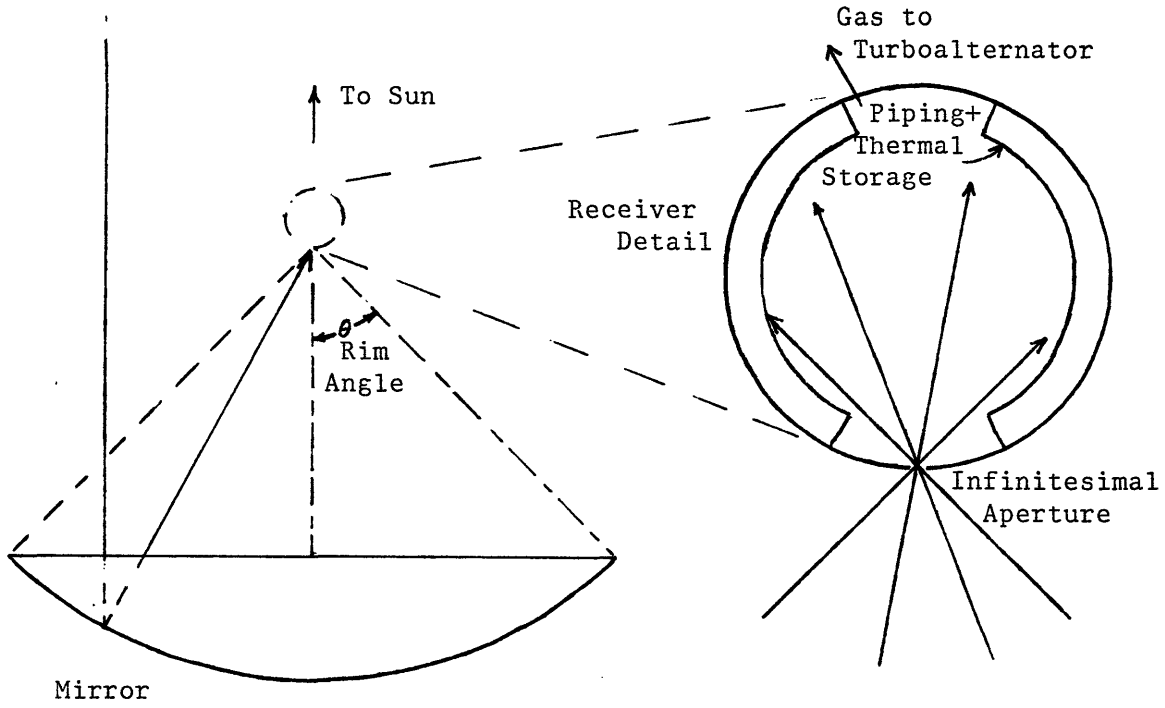

Ideal Energy Collection

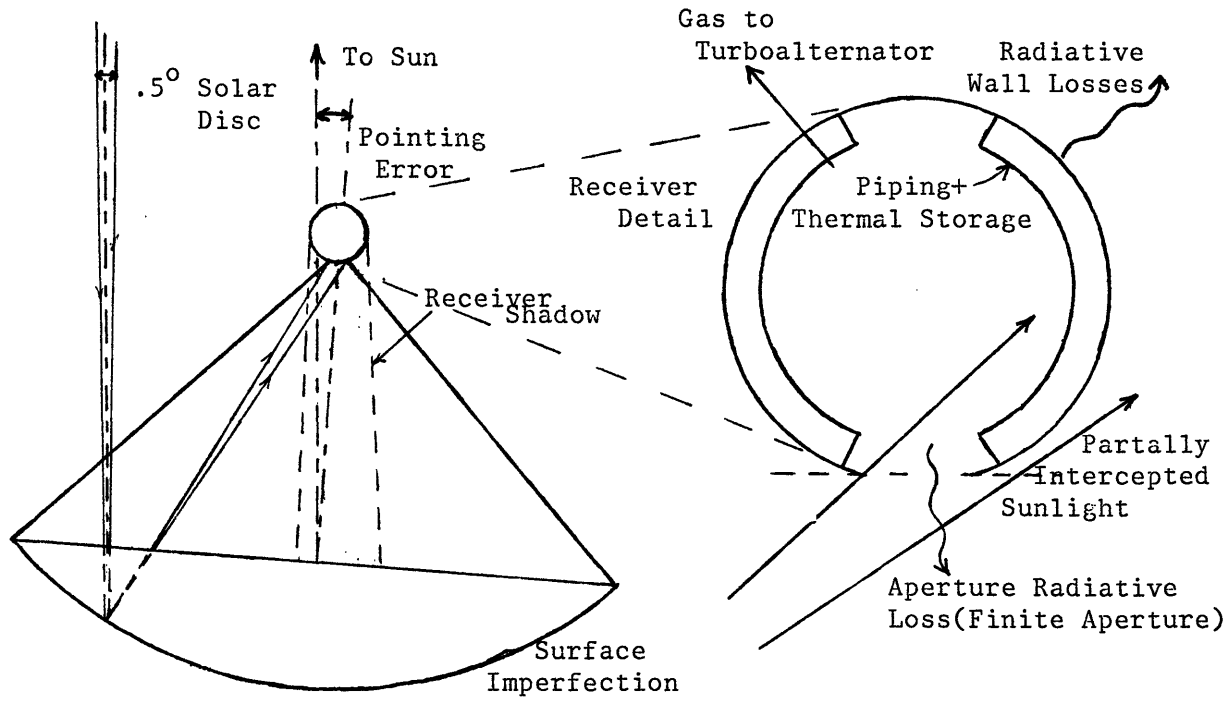

Actual Energy Collection

Figure 1.4 Solar Energy Collection for LEO Power System

Thus, the net heat collected may be stated as

$$Q_c = IA\rho G\phi\alpha - A_r\epsilon_r\sigma(T_r^4 - T_{bk}^4) - A_w\epsilon_w\sigma(T_w^4 - T_{bk}^4) \qquad (1.5)$$

where

I = solar flux (low value 1323 w/m^2 in LEO)

A = mirror projected area, m^2

ρ = mirror reflectivity

G = proportion of unblocked incoming light to mirror

ϕ = intercept factor: proportion of energy at the focal plane which enters the receiver

α = effective absorbtivity of the chamber (aperture)

A_r = receiver aperture area, m^2

ϵ_r = effective receiver emmissivity (aperture)

σ = Stefan-Boltzmann constant (5.67×10^{-8} W/m^2°K)

T_r = receiver interior temperature, °K

T_{bk} = effective space background temperature, °K

A_w = outer wall area of receiver, m^2

ϵ_w = emissivity of receiver outer wall

Note the assumption that the receiver has uniform interior and exterior temperatures.

Now the receiver wall area A_w will depend critically on the detailed heat transfer design of the receiver. But from a systems design point of view, it is convenient to define a parameter "radiant loss fraction" f, which is the fraction of energy entering the receiver that is lost by wall radiation. With this definition, one may restate (1.5) as

$$Q_c = IA\rho G\phi\alpha(1-f) - A_r\epsilon_r\sigma(T_r^4 - T_{bk}^4) \qquad (1.6)$$

Dividing this by the solar energy intercepted by the mirror, IA, gives the collection efficiency, i.e.

$$\eta_c = \rho G \phi \alpha (1-f) - \frac{1}{C} \frac{\epsilon_r}{I} \sigma (T_r^4 - T_{bk}^4) \tag{1.7}$$

where C is the concentration ratio, A/A_r.

To find ϕ, Jaffe applies a model in which the focal plane energy distribution is assumed to be Gaussian, and is caused by Gaussian distributions of slope and specularity errors, pointing misalignments, and the finite solar disc. He argues that while the last of these is a crude model, it will be a minor contributor to the overall distribution for practical concentrators. The purpose of the model is to avoid the detailed optical work that is inappropriate for a simple optimization.

Thus, the value of ϕ has the following relation to A_r,

$$\phi = 1 - e^{-A_r/2\pi\sigma_r^2} \tag{1.8}$$

with σ_r being the standard deviation of flux distribution in the focal plane, in meters. This relates to the other assumed distributions by an approximation to a ray tracing analysis:

$$\sigma_r^2 = R^2\delta^2 \frac{1}{\theta \tan^2 \frac{\theta}{2}} \left[\frac{-1}{3\sin^3\theta\cos\theta} + \frac{2-\cos\theta}{3\sin^3\theta} + \frac{2-2\cos\theta}{\sin\theta} + \frac{4\sin\theta}{3\cos\theta} - \ln \tan\frac{1}{2}\left[\frac{\pi}{2} + \theta\right] + \ln \tan\frac{1}{2}\left[\frac{\pi}{2} - \theta\right] \right] \tag{1.9}$$

where

R = concentrator radius, meters

θ = rim angle (see Figure 1.4)

and

$$\delta^2 = (2\sigma_{slope})^2 + \sigma_\omega^2 + \sigma_p^2 + \sigma_{sun}^2 \tag{1.10}$$

with the following standard deviations,

σ_{slope} = slope errors

σ_{ω} = specularity spread

σ_{p} = pointing error

σ_{sun} = incoming sunlight.

By defining a non-dimensional distribution,

$$\sigma_f = \frac{\sigma_r}{R} \tag{1.11}$$

ϕ may be related to concentration ratio using (1.8), with the result that

$$C = \frac{1}{2\sigma_f^2 \ln \frac{1}{1-\phi}} \tag{1.12}$$

Using (1.8) in (1.6), and differentiating with respect to A_r, results in an optimum value of ϕ given by

$$\phi_{opt} = 1 - \frac{2\sigma_f^2}{I\rho G\alpha(1-f)} \epsilon_r \sigma (T_r^4 - T_{bk}^4) \tag{1.13}$$

For reasonable value of mirror slope errors, the value of η_c from this optical model is insensitive to choice of θ, which is related to focal ratio f_r by the relation

$$f_r = \frac{F}{D} = \frac{1+\cos\theta}{4\sin\theta} \tag{1.14}$$

where

F = focal length

D = 2R = mirror diameter

Let $\alpha \approx \epsilon \approx 1$, G = .96, σ_{ω} = 0.5 mrad, σ_s = 2.3 mrad, based on Jaffe's work. Also, let I = 1323 W/m^2, ρ = .92, σ_p = 0.2 mrad from [1], Table 3.3.1-2. Set f = .05 and try two values of θ, 45° and 60°, and two of σ_{slope}, 2.0 mrad and 1 mrad. The values of σ_{slope} are both optimistic by Jaffe's standards, but the latter was achieved in NASA Lewis's work on a rigid magnesium alloy reflector in 1973 ([20], p. 42).

Figure 1.5 shows the results of these assumptions on optimum collector efficiency η_c with mirror slope error and rim angle as parameters. The numbers along the curves note corresponding optimum concentration ratios. The strongest effect of reducing mirror quality through σ_{slope} is not on collection efficiency but on concentration ratio. As mirror errors increase, the focal image size does as well; the receiver aperture widens, thus decreasing C. However, significant loss out this aperture -- reducing η_c -- does not occur until higher temperatures are reached. Thus, it is seen that mirror quality (which will directly affect mirror mass) is of particular concern for the system using MgF_2 storage, which will operate at a receiver temperature of about 1550°K.

Jaffe states that the optical approximations represented above have an error of about 5-10%; he also states that more complex solutions indicate that the maximum efficiency for a paraboloid mirror is achieved with $f_r = 0.6$ ($\theta = 45°$) as long as ϕ is close to 1. The rim angle of 45° is adopted here; a consequence is an increase of about 4% in mirror area over that of a flat surface of the same diameter. Also, henceforward it is assumed that surface slope error is 2 mrad.

Based upon the work done by NASA Lewis described in [11] and by Rockwell in [1], it is reasonable to assume that a means of closing the receiver aperture is available. With the receiver aperture closed during shadow, losses during that period are essentially limited to radiation from the outer walls. If the temperature of the cavity remains the same during shadow as during insolation, the radiative loss rate will remain the same. This shadow period loss must be made up with additional phase change thermal storage material.

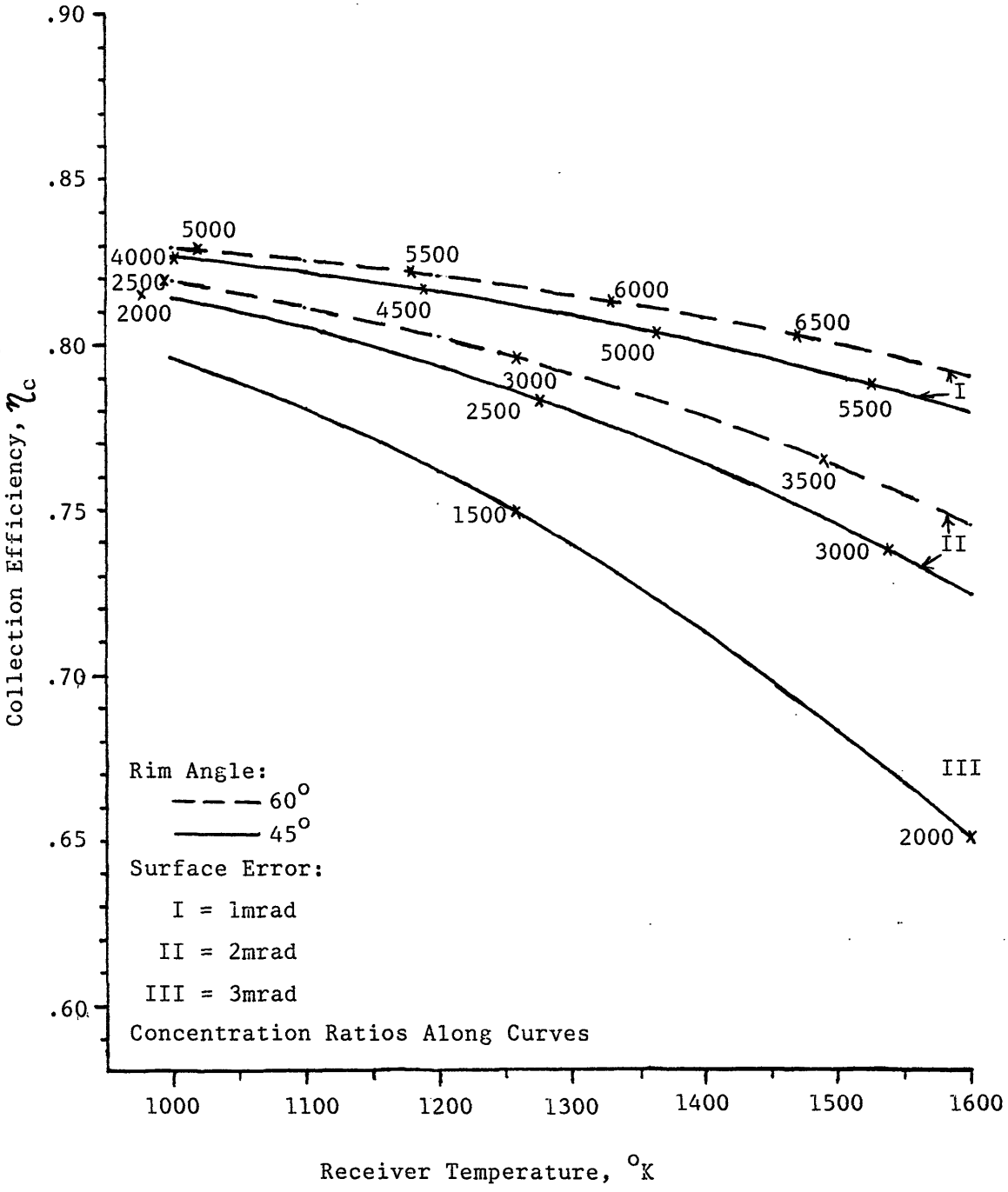

Figure 1.5 Optimum Collection Efficiency and Concentration Ratio as a Function of Receiver Temperature, Mirror Surface Error and Rim Angle

Thus, the storage efficiency is defined here as

$$\eta_{sto} = 1 - \frac{\text{energy radiated during shadow from walls}}{\text{energy collected for storage during insolation}} \qquad (1.15)$$

The energy lost by radiation during shadow is given by

$$H_{rs} = IA\rho G\phi\alpha f t_{sh} \qquad (1.15a)$$

which may be combined with the expression for mirror area required,

$$A = \frac{P_L}{I\eta_c\eta_{cy}\eta_{alt}}\left(1 + \frac{t_{sh}}{\eta_{sto}t_{sun}}\right) \qquad (1.15b)$$

where thermal engine (η_{cy}) and alternator (η_{alt}) efficiencies are now separated. The energy collected during insolation for use during shadow is

$$H_{sh} = \frac{P_L}{\eta_{sto}\eta_{cy}\eta_{alt}} t_{sh} \qquad (1.15c)$$

Combining these two with (1.15) and solving for η_{sto} gives

$$\eta_{sto} = \frac{1 - \frac{1}{\eta_c}\left[\rho G\alpha\phi_{opt}f\right]\frac{t_{sh}}{t_{sun}}}{1 + \frac{1}{\eta_c}\left[\rho G\alpha\phi_{opt}f\right]} \qquad (1.15d)$$

which becomes unity as the radiation loss factor goes to zero.

1.5.2 Thermal Engine Cycle

For the purposes of the present comparison, a non-optimized regenerated Brayton cycle is used, as schematically outlined in Figure 1.6. Starting with the assumptions in Table 1.3, which are derived from [15] and [21], the following relations are used to derive the cycle efficiencies and temperatures there. Let

$$\tau_t = \frac{T_4}{T_3} \quad , \quad \pi_t = \frac{P_3}{P_4} \qquad (1.16a)$$

$$\tau_{co} = \frac{T_1}{T_0} \quad , \quad \pi_{co} = \frac{P_1}{P_0} \qquad (1.16b)$$

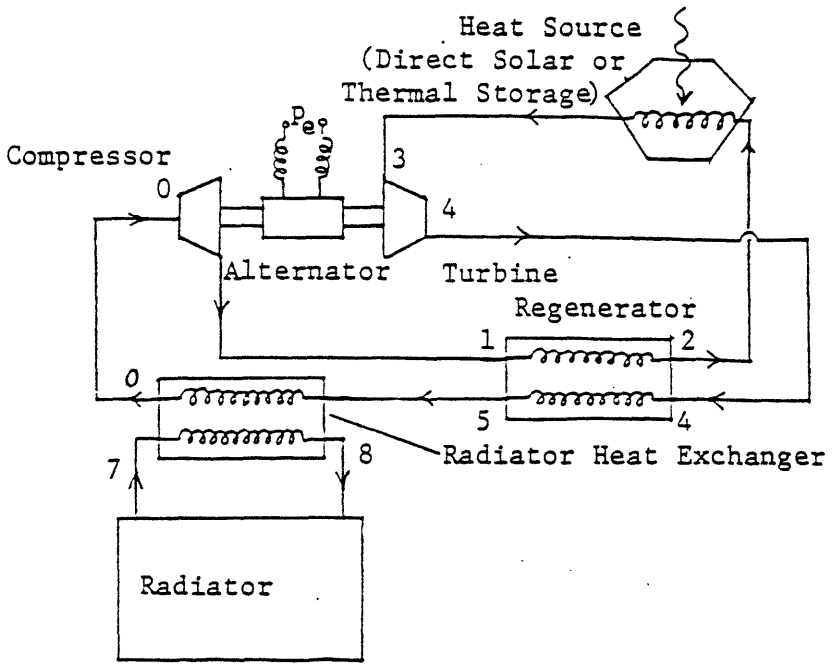

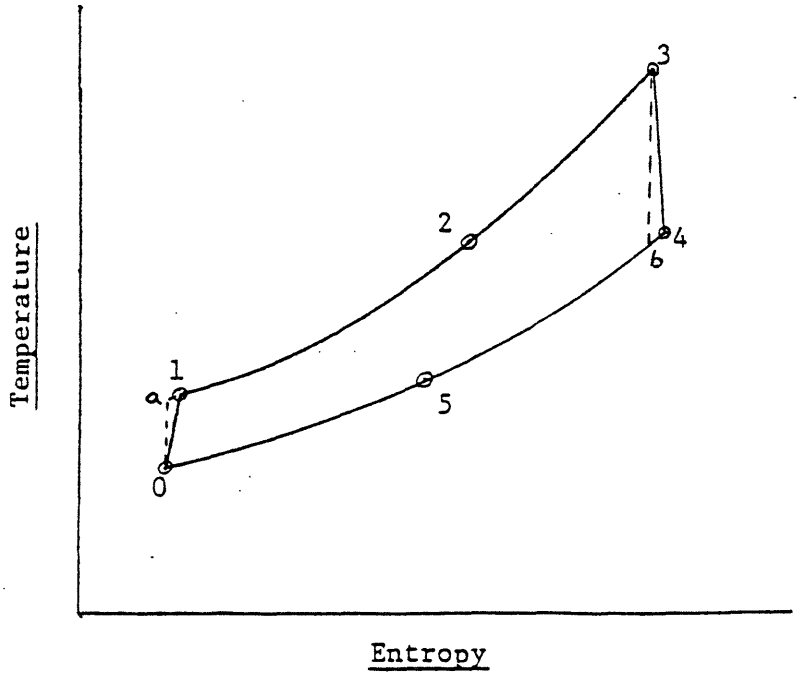

Figure 1.6: Brayton Cycle with Regeneration

Table 1.3

Regenerated Brayton Cycle Characteristics

	LiF	BOTH	MgF_2
Assumed temperatures ($^\circ$K)			
Peak (T_3)	1071		1486
Bottom (T_0)	350		350
Compressor pressure ratio (π_c)	2.4		3.3
Pressure loss factor (π_L)		.90	
Component efficiencies:			
Turbine		.9	
Compressor		.85	
Alternator		.9	
Effectiveness			
Regenerator		.9	
Radiator Heat Exchanger		.9	
Working fluid	He-Xe, with molecular weight = 40, $R_g = 208 \frac{J}{kg^\circ k}$, $c_p = 519.75 \frac{J}{kg^\circ k}$ ($\gamma = 1.67$)		
Cycle temperatures ($^\circ$K)			
T_1	523		602
T_2	787		973
T_4	816		1014
T_5	552		643
T_7	328		317
T_8	530		610
Cycle efficiency η_{cy}	.289		.429

NOTES: Peak temperature is assumed to be 50°K below melting point of respective storage material. Following the model of [15], peak pressure is assumed to be ~2 atm to obtain reasonably sized turbogenerator components. The pressure ratios for LiF and MgF_2 were from system optimizations done by [21] and [15] respectively. (The latter one was for a system using storage at 1685°K but the cycle efficiency is relatively insensitive to pressure ratio in the regenerated Brayton cycle.)

If we assume an ideal gas with $c_p(T)$ = constant, we may state for turbine and compressor efficiencies respectively,

$$\eta_t = \frac{T_3 - T_4}{T_3 - T_b} \tag{1.17a}$$

$$\eta_{co} = \frac{T_a - T_0}{T_1 - T_0} \tag{1.17b}$$

from which

$$\tau_t = 1 - \eta_t\left[1-\left[\frac{1}{\pi_c \pi_L}\right]^{\frac{\gamma-1}{\gamma}}\right] \tag{1.18a}$$

$$\tau_{co} = 1 + \frac{(\pi_c)^{\frac{\gamma-1}{1}} - 1}{\eta_c} \tag{1.18b}$$

The factor π_L represents an assumed 10% pressure loss around the cycle occuring mainly in the heat receiver tubing. This is a conservative assumption.

The effectiveness of the regenerator and of the radiator heat exchanger can be defined respectively as

$$\epsilon_1 = \frac{T_2 - T_1}{T_4 - T_1} \tag{1.19a}$$

$$\epsilon_2 = \frac{T_8 - T_7}{T_5 - T_7} \tag{1.19b}$$

thus resulting in

$$T_2 = T_1 + \epsilon_1(T_4 - T_1) \tag{1.20}$$

If it is assumed that heat losses from the heat exchangers are minimal, and that the system can be constructed so that

$$(\dot{m}c_p)_{\substack{\text{He-Xe}\\\text{gas}}} = (\dot{m}c_p)_{\substack{\text{radiator}\\\text{fluid}}} \tag{1.21a}$$

i.e. that

$$T_4 - T_5 = T_1 - T_2 \tag{1.21b}$$

then

$$T_5 = T_4 - \epsilon_1(T_4-T_1) \tag{1.21c}$$

It can then be shown that

$$T_7 = (\frac{1}{\epsilon_2} - 1)(1 - \epsilon_1)T_4 + [(\epsilon_1 - \frac{\epsilon_1}{\epsilon_2})\tau_{co} + 1]T_1 \tag{1.22}$$

Thus the temperatures shown in Table 1.3 are derived, along with the efficiency given by

$$\eta_{cy} = \frac{(T_3-T_4) - (T_1-T_0)}{T_3 - T_2} \tag{1.23}$$

The thermal throughput of the regenerator is

$$P_t = \dot{m}c_p(T_4-T_5) \tag{1.24a}$$

where

$$\dot{m} = \frac{P_L}{\eta_{alt}} \frac{1}{c_p[(T_3-T_4) - (T_1-T_0)]} \tag{1.24b}$$

1.5.3 Receiver Model

The thermal receiver is modeled as a sphere consisting of several layers of metallic insulation supported by trusswork and containing He-Xe gas flow tubes (Figure 1.7a). This model is based on [21], but with some corrections and improvements. The tubes are surrounded by an annulus of energy storage material which for simplicity is assumed to be evenly distributed along the tube. The innermost insulation layer forms a reflective surface. Reasonable geometric rules indicated in the figure are used to determine the size of the sphere. Explicitly

$$L_p = \frac{3}{4}\pi R_c \tag{1.25}$$

and

$$2\pi R_c \sin 2\theta_0 = N(1+\sqrt{2})D_{p_0} \tag{1.26}$$

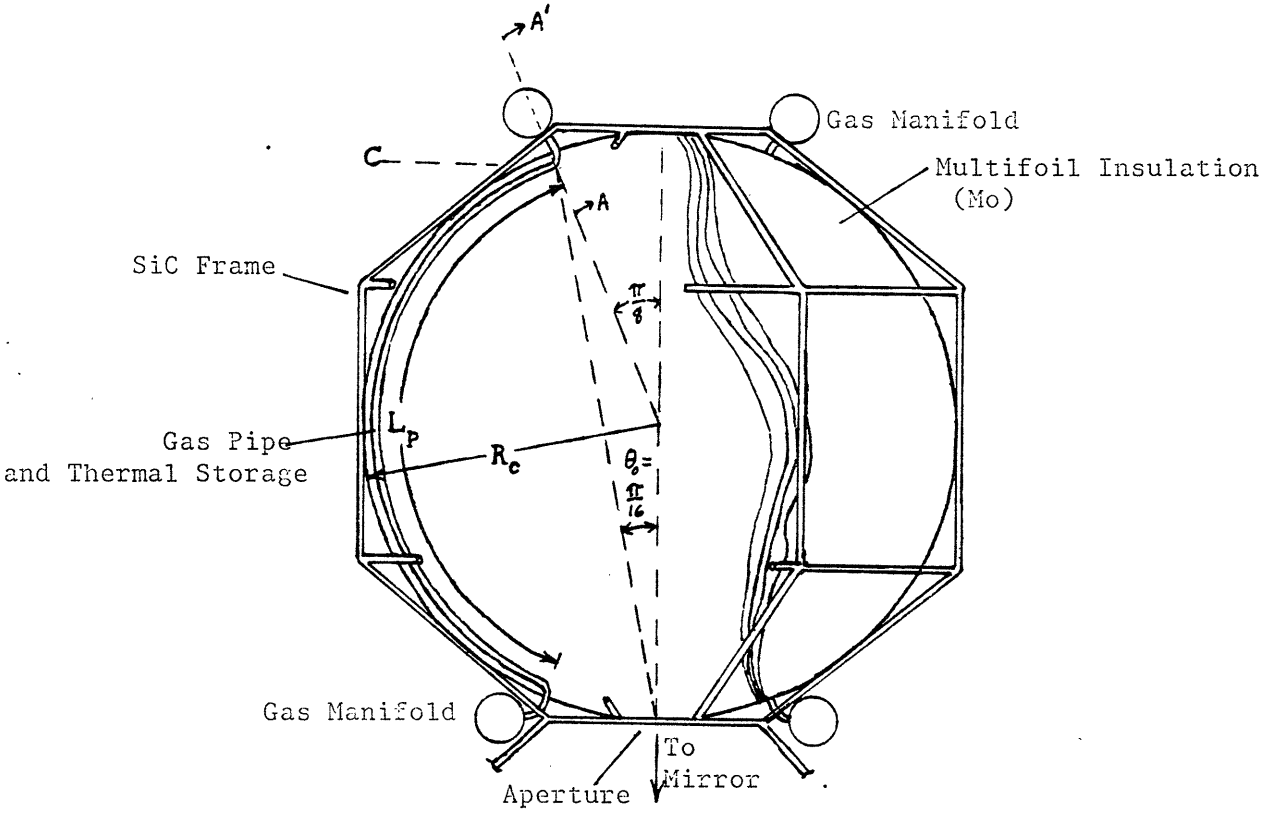

Figure 1.7a Cutaway of Receiver

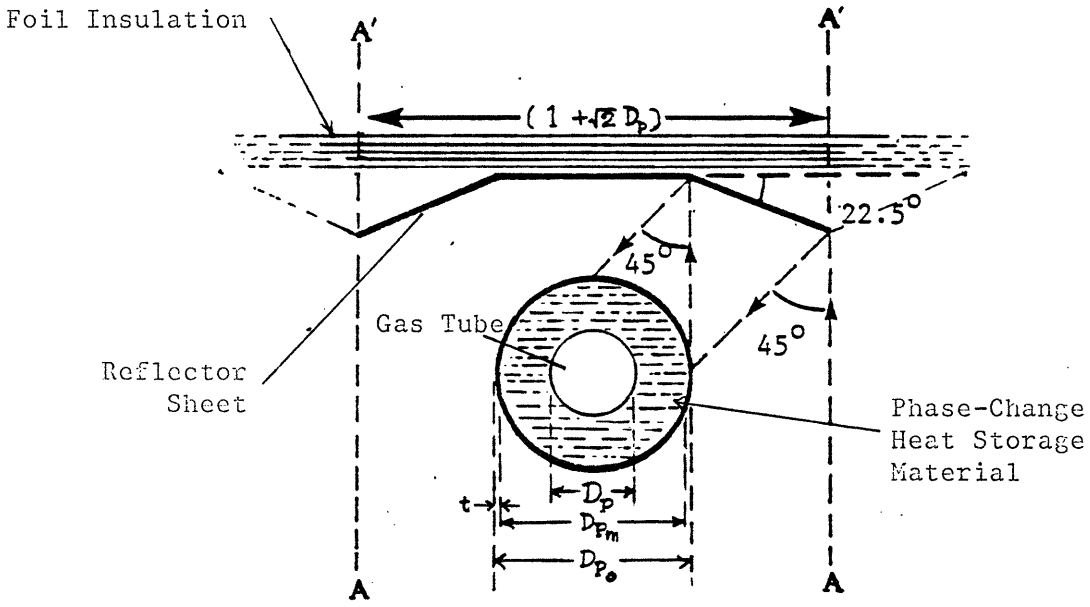

Figure 1.7b Section Through AA'; Gas Tube and Storage

for circumferential packing of pipes and reflectors at level "C", where

L_p = pipe length, m

R_c = sphere radius, m

D_{p_0} = pipe diameter, including storage and outer tube

N = number of pipes

$\theta_0 = \frac{\pi}{16}$

Now the ratio of pipe length to diameter may be obtained by assuming fully developed turbulent flow and considering a control volume of length dL. In the steady state the sum of heat transported into the volume by the wall and by the gas flow per unit time is set to zero, thus obtaining

$$\frac{\partial T_g}{\partial L} = \frac{4h_g(T_w - T_g(L))}{\rho c_p D_p u_\infty} \tag{1.27a}$$

with

h_g = heat transfer coefficient of gas, $\frac{W}{m^2 {}^\circ K}$

T_w = wall temperature, $^\circ K$

T_g = gas temperature, $^\circ K$

u_∞ = gas velocity, m/sec

ρ = gas density, kg/m^3

D_p = flow tube diameter

c_p = gas specific heat, $J/kg\ ^\circ K$

which may be restated as

$$\frac{\partial T_g}{\partial L} = \frac{4S_t}{D_p}(T_w - T_g(L)) \tag{1.27b}$$

If the Stanton number S_t and wall temperature T_w are assumed constant along

the pipe, this gives

$$\frac{L_p}{D_p} = \frac{1}{4S_t} \ln \frac{T_w - T_{g_{in}}}{T_w - T_{g_{out}}} \tag{1.27c}$$

where the gas temperatures refer to the beginning and the end of the pipe.

For turbulent flow in smooth tubes, the classical Moody plot friction factor can be approximated as

$$f_f \cong \frac{.046}{Re^{.2}} \qquad 20{,}000 \leq Re \leq 300{,}000 \tag{1.28a}$$

while the Stanton number with the modified Reynolds approximation is given by

$$S_t \cong \frac{f_f}{2} \frac{1}{Pr^{2/3}} \tag{1.29}$$

For the cases considered here we assume Pr = .7. Pitts and Sissom [22], p. 170, recommend a modification based on viscosity ratio to the 0.14 power when the difference between the wall and the bulk temperature exceeds 56°K, but the error caused here is not significant given the overall level of approximation.

The tube diameter is found by equating the required thermal power input per tube to the power picked up by the gas in each tube in the heating process, i.e.

$$\dot{m} c_p (T_3 - T_2) = \frac{P_L}{\eta_{alt}\eta_{cy}} \tag{1.30a}$$

or

$$u_m N \rho_m \frac{\pi D_p^2}{4} c_p (T_3 - T_2) = \frac{P_L}{\eta_{alt}\eta_{cy}} \tag{1.30b}$$

$$D_p = \left[\frac{4}{\pi} \frac{P_L}{\eta_{alt}\eta_{cy} c_p (T_3 - T_2)} \frac{1}{\rho_m u_m} \frac{1}{N} \right]^{1/2} \tag{1.31}$$

where ρ_m, u_m are assumed to be median values for the gas density and velocity over the tube length

based upon temperatures T_2 and T_3 defined in Table 1.3. Pressure losses along the pipe can be approximated as

$$\frac{\Delta p}{p} = 2\gamma f_f \frac{L_p}{D_p} M^2 \tag{1.32}$$

where median values are again assumed.

For the conditions encountered here, choice of M = 0.1 at the end of the pipe results in losses of a few per cent. Consequently, conditions at the pipe entrance can be found by assuming pressure constant (at 2 atm) and applying continuity. Median Reynolds number is obtained by combining these conditions with gas viscosity for the He-Xe gas as derived using the gas mixture relations given by Rohsenow and Hartnett [23].

The diameter of the tube to the outer edge of the storage material is expressible as

$$D_{p_m} \cong \left[(D_p+2t)^2 + \frac{4}{\pi} \frac{M_{sto}}{\rho_{sto} L_p N}\right]^{1/2} \tag{1.33a}$$

where

M_{sto} = storage mass, kg

ρ_{sto} = storage material density, kg/m^2 (liquid)

t = tube thickness, m

and the value of D_{p_0} is just

$$D_{p_0} = D_{p_m} + 2t \tag{1.33b}$$

with the assumption that the outer tube thickness is the same as that for the inner one.

The above equations allow an iterative solution for the values of N, D_p, L_p, R_c, D_{p_0}, and D_{p_m}. A refinement can be made by considering the effect of the storage material thickness on heat transfer to the gas. The "worst case"

conditions (in terms of required heating length L_p) occur at the end of the Earth eclipse (or shadow) portion of the orbit. At that time the storage medium surrounding the gas tube is entirely frozen, or nearly so, and the thermal gradient through the storage is the largest possible. The effect is to introduce a thermal resistance between the heat source and the bulk gas. So one may define an effective heat transfer coefficient $h_{g_{eff}}$ based upon the gas tube diameter (and thermal conductivity of the solidified storage material, k_s) as

$$h_{g_{eff}} = \frac{1}{\frac{1}{h_g} + \frac{D_p}{2k_s} \ln \frac{D_{pm}}{D_p}} \tag{1.34}$$

Then, using the definition of Stanton number, an effective value of S_t may be expressed as

$$S_{t_{eff}} = \frac{h_{g_{eff}}}{h_g} S_t \tag{1.35}$$

where S_t is as defined in (1.29).

So a parallel iteration may then proceed. One iterates over N, D_p, etc., to provide a proper geometric fit. $S_{t_{eff}}$ is revised after the fit is obtained and used in place of S_t to revise L_p/D_p for the next iteration over N. This proceeds until L_p/D_p converges.

1.5.4 Component Masses

Using the above models, masses of the various system components may now be developed. Specific masses, temperatures, and other data relevant to these calculations are summarized in Table 1.4, except where they have been tabulated earlier.

Table 1.4

Summary of Mass Determining Assumptions

Mirror	$4\ kg/m^2$ [1]	
Receiver	Tubing:	Nb-10Hf, 8800 kg/m^3, for LiF system ASTAR 811C, 16700 kg/m^3, for MgF_2 system Thickness, .25 mm, identical for all tubes; double tubing mass for manifolds; heat storage material of constant thickness along tube
	Insulation:	Mo sheet, 5×10^{-5} m thick Emmissivity $\approx .12$ Double number of sheets for leakage, and miscellaneous related items (e.g. spacers, reflectors) Background temperature 250°K
	Frame:	Silicon carbide members with $E = 60 \times 10^6$ psi, density = 3220 kg/m^3
Radiator	Two sections NaK above 450°K, 12 kg/m^2 H_2O below 450°K, 4.8 kg/m^2 Includes tubes, fins, headers, heat exchanger liquid, and system pumping penalty Pipe thickness set by 10-yr mean period to puncture 25% spare panels included Emmissivity 0.9, background temperature 250°K	
Regenerator	0.54 kg/kW_t [1]	
Turbo-alternator	3.4 kg/kW_e [1]	

The amount of phase change heat storage material required is given by

$$M_s = \frac{1}{h_f}\left[\frac{P_L t_{sh}}{\eta_{sto}\eta_{cy}\eta_a}\right] \qquad (1.36)$$

where

h_f = heat of fusion, W/kg

η_a = alternator conversion efficiency

Mirror mass is expressed as

$$M_m = \mu_m(1.042)\,\frac{P_L}{I\eta_c\eta_{cy}\eta_a}\left[1+\frac{1}{\eta_{sto}}\,\frac{t_{sh}}{t_{sun}}\right] \qquad (1.37)$$

where the factor 1.042 accounts for the parabolic shape. The mass per unit area, μ_m, is assumed to be about 4 kg/m^2 which is from [1]. Judging from [19], this is a conservative figure.

Following the data in [1], the turbogenerator is take to have a mass of about 3.4 kg/kW_e, and to be the same for both the LiF and MgF_2 storage systems. An additional component is the regenerator. If the thermal throughput for the LiF system regenerator in [1] is similar to that for the LiF system here, the regenerator system mass will be about 0.54 kg/kW_t.

In [21], Annen developed a space radiator model based on the use of a pumped fluid -- NaK above 450°K and water below that point. He also developed an expression for an effective radiator temperature given inlet, outlet, and background radiation temperatures. The radiator pipe thickness was set by a 10-year mean period to meteroid puncture and the model included a 25% allowance for spare panels. If one includes in the accounting the radiator tubes and fins, headers, heat exchangers, liquid and a pumping penalty, the effective mass (over one side) is about 12 kg/m^2 for the NaK portion and 4.8 kg/m^2 for the H_2O part. For comparison, [1, pp 3-108, 3-109],

proposes a radiator using "FC-85" fluid (for a brayton cycle using LiF storage) which has a mass of 8.46 kg/m^2.

The receiver insulation is assumed to be molybdenum sheet .05 mm thick, with an emmissivity of 0.12. The cavity temperature is slightly above the storage material melting point, and space background is 250°K. The number of molybdenum sheets required is doubled at the end of the calculation to compensate for leakage.

For the receiver tubing one must consider criteria for pipe thickness. Say that for purposes of fabricability the minimum is 0.25 mm. Another lower limit on pipe thickness is set by creep due to internal gas pressure over the lifetime of the system. Figures 1.8a and 1.8b show creep data as compiled from various sources by Conway in [24]. Now Nb-1Zr was used for the NASA LiF storage receiver. If we assume a 10-year lifetime at 1135°K, internal pressure of 2 atm, the Larson-Miller Parameter (LMP) is about 40.7×10^3. This requires an extrapolation of the Nb-1Zr curve shown in the figure and for a pipe diameter of about 3.8 cm (found from the iteration in the previous section) leads to a required thickness of about 1 mm. If the Nb-10Hf alloy is used, the minimum thickness is reduced to below .25 mm. (Conway notes that there is considerable uncertainty in the Nb-1Zr creep data, but the correlation shown is conservative.)

For the MgF_2 storage system, the higher temperature to which the metal is exposed (assumed to be 1550°K) leads to an LMP of 55.6×10^3 and the choice of the tantulum alloy ASTAR 811-C. With a pipe diameter of ~2.5 cm the wall thickness required is less than .10 mm, based on Figure 1.8a. However, note that Figure 1.8b implies that, given the test data scatter, a 2σ certainty of

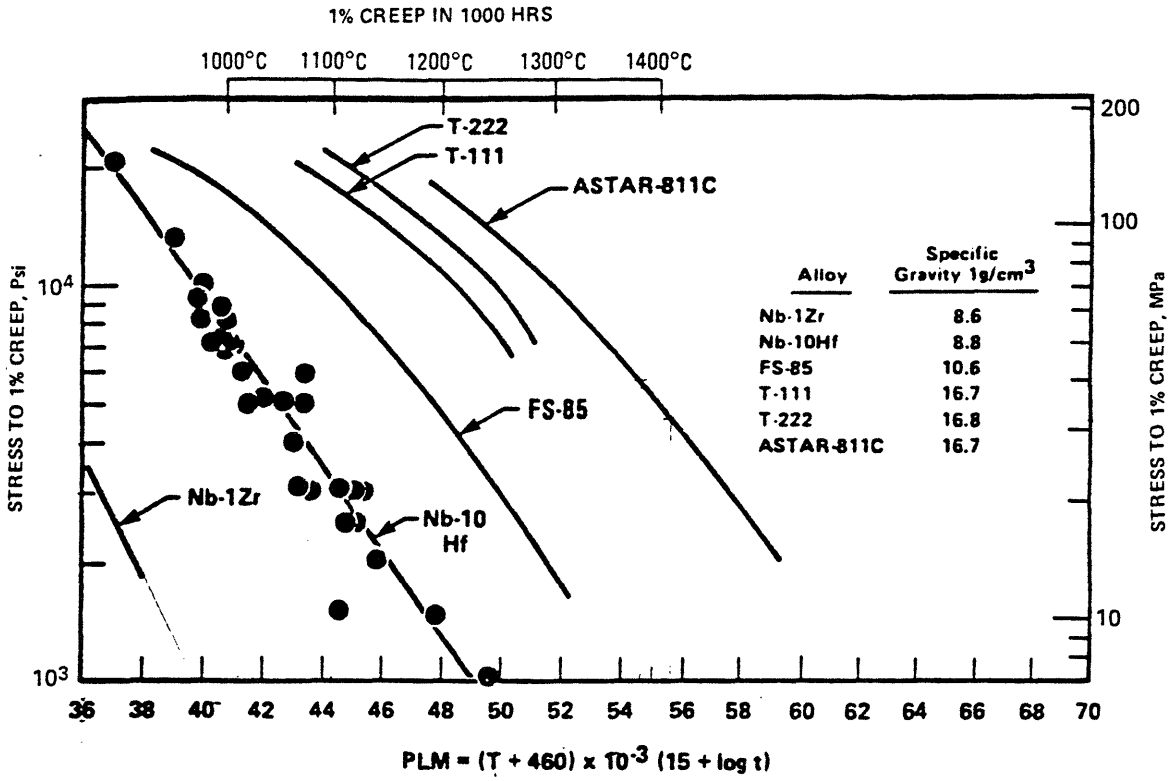

Figure 1.8a Creep Data for Refractory Alloys (Conway,[24])

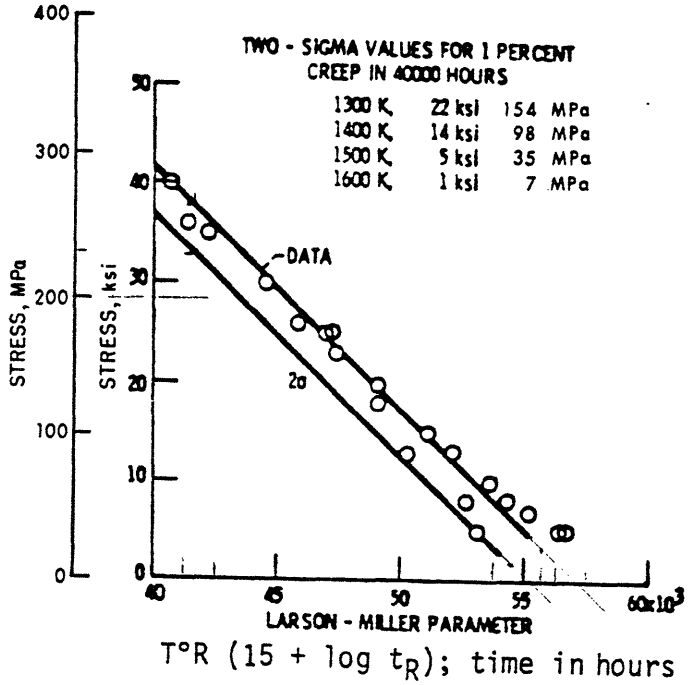

Figure 1.8b Creep Data Scatter for ASTAR-811C (Conway,[24])

being within 1% creep is unachievable. However, this is probably not critical for the receiver tubing.

A pipe thickness of .25 mm for Nb-10Hf is chosen for the system using LiF and .25 mm ASTAR for the one using MgF_2. This mass is then doubled to account for required manifolding. (By accident this leads to pipe masses for each system which are within 10% of each other.)

The structural mass of the truss work surrounding the receiver insulation is scaled from the mass derived by the author in [14]. The truss work forms an octagonal frame, and the beam cross sections are determined by the static bucking load of a member in the lower third of the frame when the receiver is subjected to 3 g's acceleration. Then one may show that the structural mass in kilograms can be scaled as the relation

$$M_{str} = 16.2 \left[\frac{R_c}{1.062}\right]^2 \left[\frac{M_g}{133}\right]^{1/2}$$

where M_g, the mass supported by a single lower member is assumed to be given by

$$M_g = \frac{1}{8}\left[M_{turbine} + M_{regenerator} + M_{radiator}\right]$$

$$+ \frac{1}{8}\left[\frac{3}{4}\left[M_{insulation} + M_{storage} + M_{tubing} + M_{manifolding}\right]\right]$$

The implicit assumption is that the items in the first bracket are located above the receiver in the launch vehicle. Those in the second bracket are within the receiver and are partially supported by side braces during launch. The structural material is SiC.

Results of the mass calculation are shown in Figure 1.9 as a function of the receiver heat loss factor f. At low values of f, insulation requirements

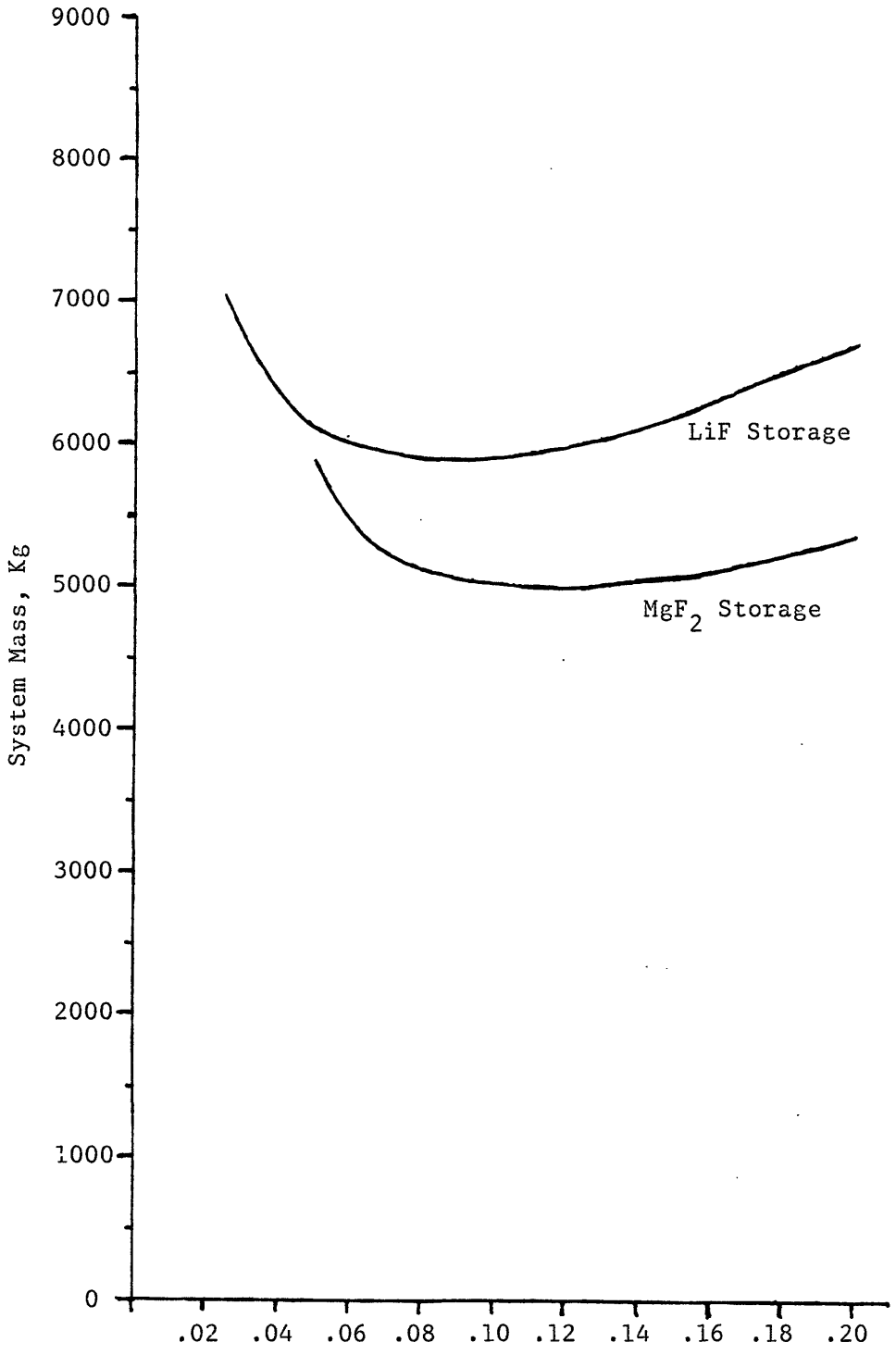

Figure 1.9 System Mass Versus Radiant Loss Fraction, f

raise the system mass; at high values, the collection mirror mass drives system mass as losses must be made up. A mass breakdown for the near optimum systems is given in Tables 1.5 and 1.6. As might be expected, insulation requirements for the MgF_2 system receiver impose a mass penalty over the other. Radiator and regenerator masses are less for the higher temperature, greater efficiency system. The overall mass change would be significantly reduced if the mirror mass/area went down. Such a reduction would be more likely to be achievable in the LiF system, which, since it operates at lower temperature can tolerate lower mirror accuracy for a given collection efficiency (as shown in Figure 1.5). In sum, then, the mass advantage of the MgF_2 system is encouraging but not definitive.

A more robust result may be represented by the comparison of potential drag areas noted in Table 1.6. This stems directly from collection, storage, and cycle efficiencies, and implies a direct reduction in fuel required to make up drag effects over the system lifetime. The mirror (flat projected) area requirements for a range of values of the factor f are plotted in Figure 1.10 and show the trend causing increased system mass at higher f. Figure 1.11 gives a dimensional comparison of the two optimized systems.

Table 1.5

Summary of Receiver-Collector Characteristics at Optimum

	Storage Type: LiF		MgF_2	
Masses				
Receiver		1823		1993
Storage	958		754	
Tubing,manifolding (sum)	318		384	
Insulation	408		762	
Structure	139		88	
Mirror		2865		2222
Parameters and Dimensions				
Mirror diameter		29.6m		26.0m
Radiative loss factor (f)		.10		.12
Aperture intercept factor (ϕ)		.9919		.9710
Concentration ratio (C)		2280		3098
Collection efficiency (η_c)		.7573		.6749
Storage efficiency (η_{sto})		.8285		.7811
Number of insulating layers (doubled quantity)		10		28
Receiver radius		2.519 m		2.059 m
Gas pipe diameter (D_p)		4.03 cm		2.57 cm
Pipe diameter including storage (D_{p_m})		6.92 cm		5.35 cm
Pipe length		5.99 m		4.82 m
Number of pipes		36		38

Table 1.6a

Mass Summary for Power Systems (kg)

Storage Type:

	LiF		MgF_2	
Receiver	1823		1993	
Mirror	2865		2222	
Radiator	688		336	
NaK section	241		137	
H_2O section	447		340	
Regenerator	193		101	
Turbogenerator	340		340	
TOTAL	5909		4992	
Net Mass Change from LiF to MgF_2 System	••		- 15.5%	

Table 1.6b

Areas Comparison for Power Systems (m^2)

Storage Type:

	LiF	MgF_2	Change
Mirror	687	533	- 22.4%
Radiator	113	52.9	- 53.2%

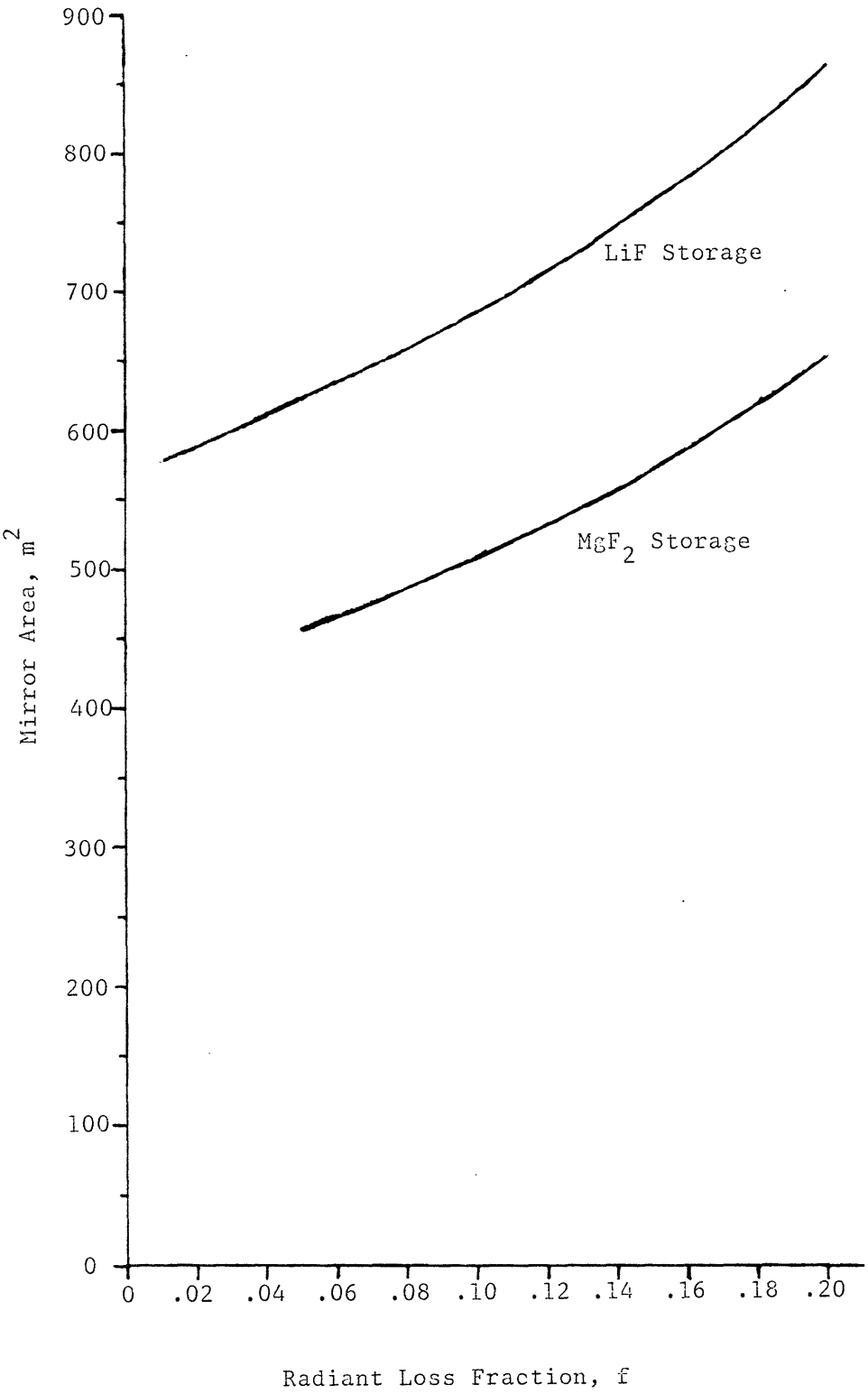

Figure 1.10 Mirror Area Versus Radiant Loss Fraction, f

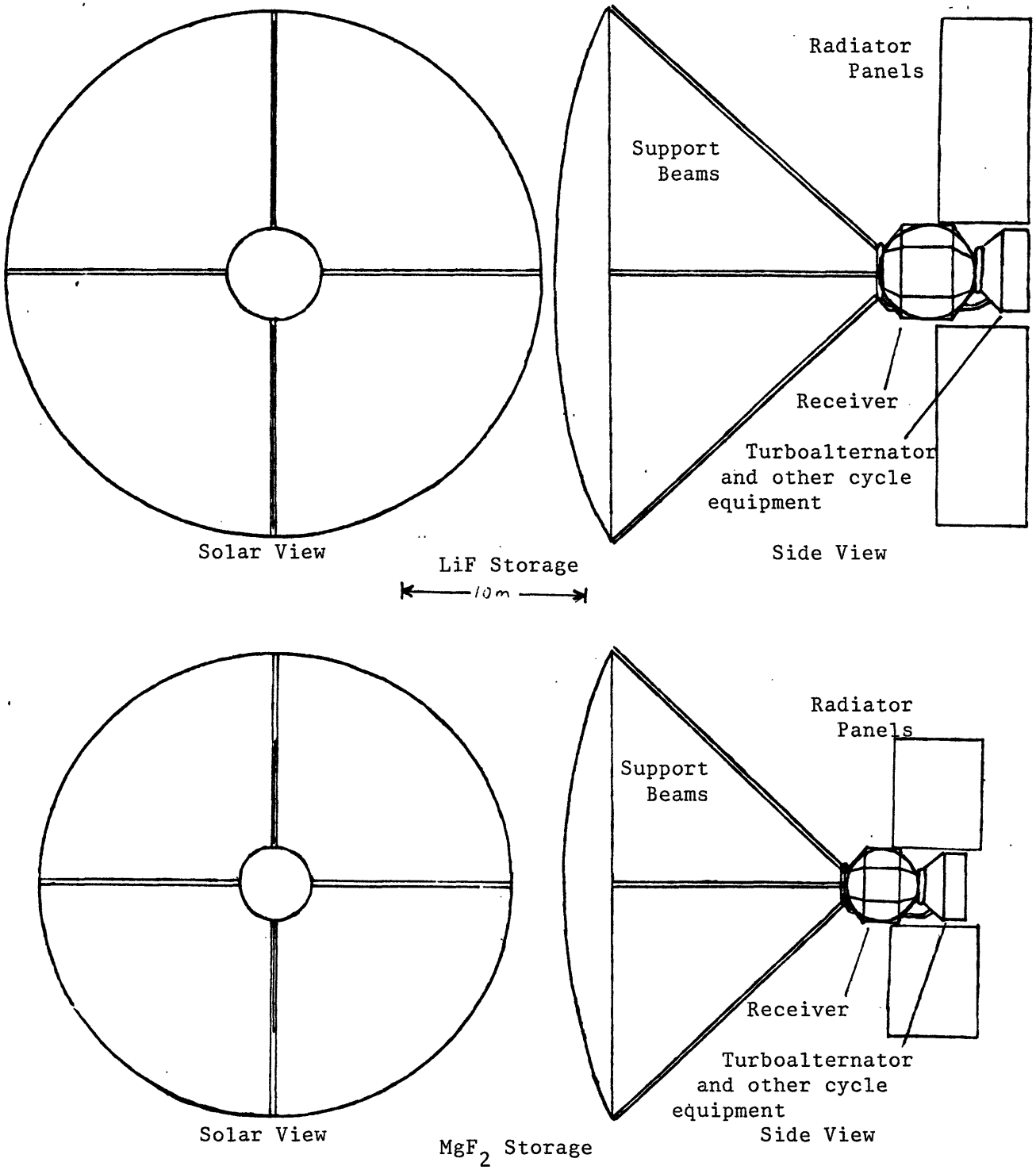

Figure 1.11 Dimensional Comparison of Power Systems

CHAPTER II

MATERIAL COMPATIBILITY IN THE APPLICATION OF MgF_2 TO SOLAR THERMAL STORAGE

2.1 Introduction

Having demonstrated the possible systems level effects of using MgF_2 thermal storage, it is appropriate to turn to more detailed technical issues. These may be summarized as follows:

- thermochemical stability of MgF_2 itself, its potential for undesirable interactions with the containment material directly or in combination with contaminants remaining from manufacture or acquired from the environment -- this to be considered over the lifetime of the system, a minimum of 10 years. Broadly put these can be called issues of corrosion.
- acquisition of data on the properties of MgF_2 relevant to component design, among which are: supercooling of the liquid, thermal conductivity, surface tension and wetability with various materials. The last two are important to the issue of void formation on freezing, which could thermally isolate some MgF_2, particularly in zero gravity conditions. Thermal conductivity, as shown in the previous chapter, will affect the length of tubing required to heat the system working gas. Supercooling refers to a delay in crystallization and release of stored heat when the storage medium is cooled below its melting point.

This chapter will be concerned with a theoretical treatment of potential corrosion problems. Some qualitative data was acquired on some of the material properties as a corollary to corrosion tests. These will be discussed later.

2.2 Corrosion and Containment

2.2.1 MgF_2 Stability Alone and With Oxygen

Magnesium Fluoride is regarded as an ionic divalent halide and appears in the single crystal form as the mineral sellaite ([25], p. 822,825; [26], pp. 5-7). For formation from the standard state at 1600°K, the free energy change

$$Mg_{(g)} + F_{2(g)} \longrightarrow MgF_{2(l)} \quad \Delta G^\circ \cong -198\text{kcal/mole} \quad ([19],[27],[28]) \qquad (2.1)$$

shows that with a pressure of 1 atm for each gas, the $MgF_{2(l)}$ is the stable component. If we consider deviation from standard conditions at this temperature, then

$$\Delta G = \Delta G^\circ + \sum_{i=1}^{r} \upsilon_i(\mu_i - \mu_i^\circ) \equiv \Delta G^\circ + \Delta G_i \qquad (2.2)$$

where μ_i is chemical potential, υ_i is the stoichiometric coefficient for each substance "i" in the equation (2.1).

At equilibrium, $\Delta G = 0$ by definition and the equilibrium "constant" for 1600°K is given by

$$\log K = \frac{-\Delta G^\circ}{RT\ln 10} = \frac{198 \text{ kcal/mole}}{(1.987 \text{ cal/mole}^\circ \text{ K})(2.303)(1600^\circ\text{K})} = 27.05 \qquad (2.3a)$$

and at the same conditions

$$K \equiv (Q)_{eq} = \frac{a_{MgF_2}}{p_{F_2} p_{Mg}} = 10^{27.05} \qquad (2.3b)$$

where the ideal gas assumption for F_2, Mg is implicit (the partial pressures

are in atmospheres). If one sets the fluoride activity to one (pure liquid) the result is

$$p_{F_2} p_{Mg} = 10^{-27.05} = 8.913 \times 10^{-28} \qquad (2.4)$$

which shows the minimal product of partial pressures for stability above MgF_2. Consider next the possibility of an exchange reaction

$$MgF_{2(l)} + 1/2\ O_{2(g)} <=> MgO_{(s)} + F_{2(g)} \qquad (2.5)$$

for which $\Delta G^o \cong 105.51$ kcal/mole. With the assumption of unit activities for the non-gaseous components, one obtains at $1600^\circ K$

$$K = 10^{-13.867} = \frac{p_{F_2}}{p_{O_2}^{1/2}}$$

or

$$p_{F_2} = 1.357 \times 10^{-14}\ p_{O_2}^{1/2} \qquad (2.6)$$

Say that the maximum pressure of O_2 in a vessel containing MgF_2 is 10^{-5} torr (1.316×10^{-8} atm) (this is approximately the chamber pressure under which the test capsules to be described below were welded). The consequence of this, using (2.6) and (2.4) is that $p_{F_2} \geq 1.557 \times 10^{-18}$ atm (1.557×10^{-13} Pa) will prevent formation of MgO, and in turn that $p_{Mg} = 5.726 \times 10^{-10}$ atm (5.802×10^{-5} Pa).

The above suggests the stability of MgF_2, but to proceed further one must consider the environment encountered in the present application.

2.2.2 Selection of Containment Materials

To operate a system at the MgF_2 melting point, one has two options in materials: high temperature ceramics or refractory metals. Initially, ceramics looked attractive because of their relatively low density. However, the problems inherent in fabricating them led to assigning them low priority. The samples that were prepared were of refractory metal alloys.

Much of the investigation into the field of refractory metals was assisted by the expertise and suggestions of Mr. Jack DeVan of the Oak Ridge National Laboratories (ORNL) and Professor John Elliott of MIT. Some time was spent searching for previous work on molten MgF_2 compatibility with refractory metals. None was found in the compilations of Janz [18] or Eichelberger [17] or in a computerized literature search. The local manufacturer of high purity MgF_2 crystals (mainly for optical applications) uses graphite crucibles [29]. A refractory metal distributor claimed that industry experience had shown Ta to be "most resistant," Mo and W less so [30], but the results to be discussed here show different results in the cases of Ta and W alloys. Recently, a Japanese patent was discovered for a tantalum crucible for molten fluorides, including MgF_2. The text presents a design solution to overcome problems with fluorides that are difficult to remove from certain crucible components due to good wetting qualities [31].

As mentioned in [24], a rough rule is that an alloy should not be used in a situation where temperatures exceed 50-60% of its absolute melting temperature. This suggests that the limiting temperature for superalloys is ~1273°K while that for Nb is around 1473°K.

Refractory metals are transition elements with half-filled or less outer "d" subshells, giving strong interatomic bonding. This results in desirable properties such as high melting point and low creep (Figures 1.8 and 2.1). However, they are also subject to complex mechanisms that can cause brittleness and fabrication problems.

Alloying can be used to change metal properties. Reactive metals such as Hf will combine with oxygen diffused into W or Ta and form precipitates that strengthen the material but reduce ductility. Tungsten added to tantalum provides solution strengthening. Creep strength is improved using materials that increase elastic modulus by decreasing self-diffusivity. In some cases, C or N is intentionally added to form strengthening precipitates with the reactive components. Some typical alloying additions are listed in Table 2.1.

On a "global" level the effects of oxygen, nitrogen, carbon, and hydrogen in the environment on the pure refractory metals has been outlined by Wilkinson [32] and DeVan. These elements will diffuse into solution in the metals; once the solution limit is reached, they will form compounds with the refractory. The surface exposed to (for example) O_2 gas will form an oxide layer. This layer may volatilize (for example, MoO_3 at 1473°K) or it may form a semi-protective surface (tungsten at 1433°K). Such considerations will determine the corrosion rate-laws as a function of temperature and pressure. As typical cases, longterm service temperatures in air for tungsten are limited to 1273°K and for molybdenum to 773°K. Tantulum and niobium have a much higher solubility for oxygen than molybdenum or tungsten, which will delay the formation of an oxide layer.

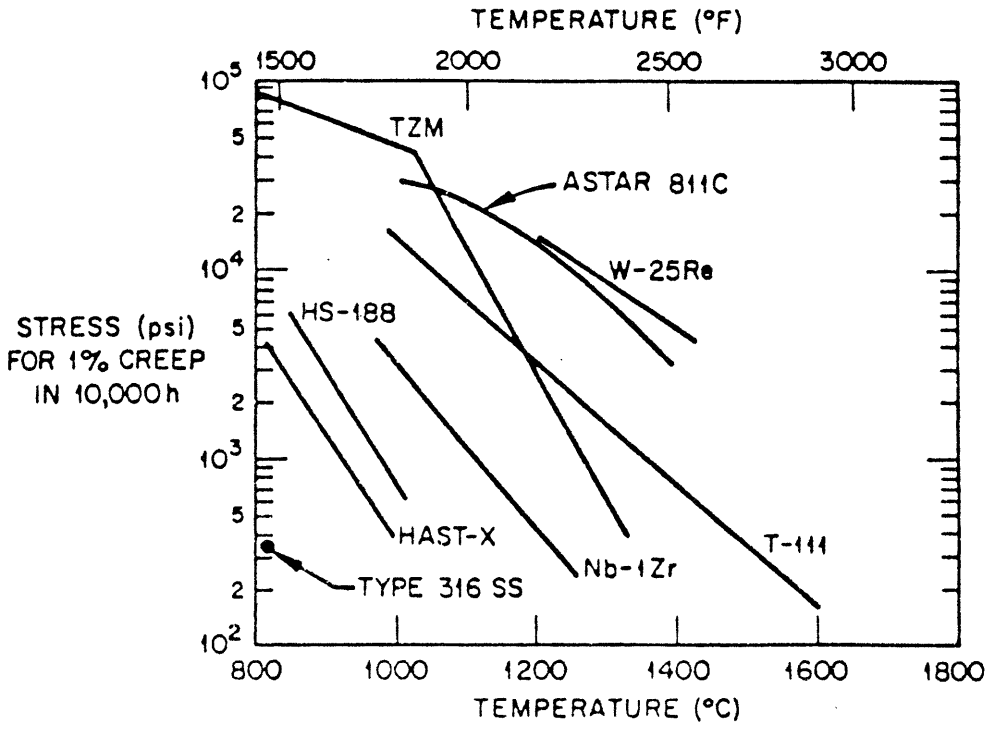

Figure 2.1 Creep Data for Several High Temperature Alloys. (Ref 24, p 11)

Table 2.1 Alloy Additions Used in Creep Resistant Refractory Metal Alloys

Alloy Base	Substitutional Solutes	Reactive Elements	Interstitial Elements
V	Cr, Cb, Ta, Mo, Fe	Zr, Ti	C, N
Cb	W, Mo, Ta	Zr, Hf	C, N
Ta	W, Re, Mo	Zr, Hf	C, N
Cr	W, Mo, Cb, Ta	Ta, Cb, Ti, Zr, Hf	C
Mo	W, Re	Ti, Zr, Cb	C, N
W	Re, Hf, Cb, Ta	Hf	C

In alloys containing reactive metals such as Hf, the latter will act as getters, reacting with oxygen before the base metal does, and increasing the effective solubility. Once these getters are exhausted, corrosion will proceed as in the pure material.

At conditions in a low earth orbit, pressures should be sufficiently low that massive corrosion as described above will not be a concern. Instead, the main effect of the gasses mentioned above is on brittleness (ductility).

Ductility of refractory metals presents a complex picture. At room temperatures, W and Mo are brittle and difficult to fabricate, whereas Ta and Nb are ductile and retain this condition regardless of the presence of oxygen. Tantalum and Nb become brittle within a few weeks with an oxygen partial pressure of 10^{-7} torr (1.3×10^{-5} Pa) at 1273°K.

This difference in behavior stems from two different mechanisms for loss of ductility, and the wide difference in interstitial oxygen solubility between the two classes of refractories. (At 2/3 of their melting point temperatures, Ta and W have oxygen solubilities of 10 atomic % and 5×10^{-5} atomic % respectively ([32], p. 7).) In Mo and W, brittleness at room temperature is caused by interstitials operating at crystal boundaries in a way that is not fully understood [DeVan]. As temperatures go up (starting at about 423°K for Mo and 773-873°K for W) the mobility of slip planes at the boundaries becomes high enough that ductility is achieved. Addition of alloying metals can move this transition temperature down.

In the case of Ta or Nb, loss of ductility is caused by the oxygen or other element going into interstitial solution within the grains themselves. (At low temperatures this is prevented by low oxygen mobility.) While

ductility is lost, strength is improved (Wilkinson). The effect on creep may also be an improvement, according to DeVan.

It should be noted here that hydrogen does not cause embrittlement of refractories at elevated temperatures, though loss of ductility can occur when the material is cooled. Further, hydrogen has the effect of reducing the activity of oxygen by having the potential to combine and form water.

Even if embrittlement does occur, it is not necessarily fatal to the system. For example, the T-111 (tantalum alloy) cannisters containing the radioisotope heat source in the Voyager spacecraft power system have not failed despite their presumed brittle state. The criterion is that there be no sudden loads, such as those caused by vibrations.

Refractory metals are quite dense, which is undesirable for space applications; for example, ASTAR 811C provides an ultimate tensile strength of 42 ksi (29 kgf/mm^2) at 1262°C (1535°K) and a density of 16.7 g/cm ([24], p. 233). Another problem (mainly for small scale experimental work) is that many of the alloys were manufactured at experimental or pilot production levels in the 1960s and are not available commercially. Much of the detailed manufacturing expertise developed at that time has dissipated.

Particularly in consideration of creep criteria, two of the leading candidates for refractory containment are ASTAR 811C (Ta-8W-1Re-.7Hf-.025 C) and W-25Re (the numbers are in weight percent). By a fortunate coincidence, recent work on a space nuclear power reactor resulted in limited production of these alloys in a usable form. They were provided to the author in the form of tubing and plate by Mr. R.L. Heestand of ORNL. Table 2.2 summarizes and compares the attributes of some leading candidate materials.

Table 2.2

Some Leading Candidate Containments

ASTAR 811-C (Ta-8W-1Re-.7Hf-0.025C)	Besides capabilities of creep resistance, this alloy has excellent fabricating and welding qualities (Buckman, et al., [33], p. 26).
W-25Re	Low diffusion rate of impurities (from W) and creep properties comparable to ASTAR make this alloy attractive with the brittleness of W being alleviated by the Re (Hagel, et al., [24], p. 109).
T-111	Creep strength good, ultimate tensile strength close to that of ASTAR ([24], p. 237), commercially available.
T-222	Creep strength better than T-111 (see Figure 1.8)
TZM (Mo-0.5 Ti-0.08Zr-0.02C)	Fairly good tensile strength, though substantially inferior in creep at MgF_2 melting point (Hagel, et al., [24], p. 109).
TZC (Mo-1 Ti-0.3Zr-0.4C) MHC (Mo-1 Hf-0.3C)	Superior tensile properties to TZM (Hagel, et al., [24], p. 104)

Also possible, although more remotely, is containment in ceramics such as SiC.

2.2.3 System Contaminants

For a space system containing molten MgF_2, there will be several external sources and types of contaminants for which some possibilities are listed in Table 2.3. This assumes the environment around a space station, for which exact particle collision rates will depend on altitude, propulsion systems, etc. Initial outgassing of the system could be a contributor to embrittlement or corrosion; to prevent this, the system might not be heated until several weeks after going on orbit, or might be heated slowly. Ram collision with the atmospheric atomic oxygen stream, such as that encountered by the shuttle, should not be a problem since the hot parts containing MgF_2 will be enclosed within the receiver cavity.

Other sources of contamination will be internal to the system. One is that resulting from impurities is the hot gas loop, and it is considered next. The other is moisture present even in high quality single crystal MgF_2. This problem will be treated later, after some further development of the thermodynamic data.

2.2.3.1 Gas Loop Contamination

It is probably impossible to achieve a sufficiently low level of contaminant species in the He-Xe Brayton cycle working gas (molecular weight = 40) to prevent embrittlement of Ta based alloys over the system lifetime ([24], p. 78). Let us say that (based on [24], p. 77) we can allow a maximum oxygen partial pressure of 10^{-8} torr (1.333×10^{-5} Pa) with tantalum alloys. Based on Chapter 1, this is out of a total pressure of the order of 2 atm.

Table 2.3 Contaminant Gasses and Their Sources

Species	Possible Sources
H , H_2	H_2O dissociation
He	Atmospheric, propellant pressurization
N_2H_4, NH_3	Propulsion systems
CH_4 and ionized products	Thruster firings, Reaction of N_2H_4 with O
OH^+	From H_2O
O	Atmosphere
H_2O	Thrusters, liquid dumps, atmospheric, vehicle and EVA leakage
CO, CO_2	Atomic O reactions, atmospheric, vehicle and EVA leakage
O_2	Atomic O recombination, vehicle and EVA leakage
N_2	Atmospheric, propulsion systems, vehicle leakage
NO	Thruster firings
Ar	Atmospheric
Heavy hydrocarbons, (e.g., Freons, trichlorethylene)	Coolant system leaks, cleaning fluid residues

The mass deposition rate of (for example) O_2 on a surface is given by

$$\Gamma_s = \frac{m_{O_2} n_{O_2} \bar{c}_{O_2}}{4} = \frac{\rho_{O_2} \bar{c}_{O_2}}{4} \left[\frac{\text{kg}}{\text{m}^2 - \text{sec}}\right] \tag{2.7}$$

where $\bar{c}$ is the mean thermal speed, n particle density at about one mean free path from the wall, and m mass per molecule. But in the presence of the flowing carrier gas there must be diffusion of O_2 through the boundary layer to the absorbing wall such that the above "n" may be substantially lower than the bulk concentration. In actual conditions there will be turbulent pipe flow of the working gas. Assume a diffusion boundary layer (O_2 depleted), whose thickness δ is of the same order as that for near wall momentum transfer (i.e. for the laminar sublayer within the turbulent flow). Then diffusion limited mass flux to the wall is

$$\Gamma_D \approx S_t \rho_{O_2} u_\infty \tag{2.8}$$

where Stanton number S_t can be used if the heat and mass transport rates are similar. Here u_∞ is the core flow velocity. Then if the Stanton number is expressible in terms of friction factor as approximately $f_f/2$ (ignoring for the moment the Prandtl number correction factor) we have

$$\Gamma_D \approx \frac{f_f}{2} \rho_{O_2} u_\infty \tag{2.9}$$

The oxygen density is that in the core flow. For comparison, in the absence of the carrier gas the mean free path would exceed the tube diameter and (2.7) would apply directly. Thus, taking the ratio of (2.7) and (2.9),

$$\frac{\Gamma_D}{\Gamma_S} = 2 f_f \frac{u_\infty}{\bar{c}} \tag{2.10}$$

Assuming the Maxwellian distribution, for which $\bar{c}_{O_2} = \sqrt{\frac{8RT}{\pi M_{O_2}}}$ and conditions

for the MgF_2 storage system from Chapter 1, ($\bar{c} \approx 991$ m/sec, $u_\infty \approx 70$ m/sec, $f_f \approx .00678$) one finds that

$$\frac{\Gamma_D}{\Gamma_S} \approx \frac{1}{1045} \tag{2.11}$$

thus implying that critical contamination levels of oxygen can be eased by about three orders of magnitude. This means an improvement from He-Xe gas contamination levels of 5 parts per trillion to 5 parts per billion. In [24], p. 75, it is stated that achieving and detecting the lower level is presently impossible; but that current techniques should be able to detect 1 ppb concentration.

2.2.4 Metal Containment Fluoride Interactions

Given a particular alloy, MgF_2, and contaminants, it is possible to consider the equilibrium conditions for the interior of a closed system.

Table 2.4 lists several products for the general reaction of the form.

$$(1/2)MgF_{2(l)} + (1/x)M_{(s)} <=> (1/x)MF_x + 1/2Mg_{(g)} \tag{2.12}$$

where the metal M undergoes the process at 1600°K. The standard free energies of reaction (Table 2.4) are from [27] and [28] (Barin) and are generally in close agreement (better than 1%) with those from [19] (the JANAF tables). The main difference between the two is that while the latter lists heats of formation for each species at each temperature (ΔG_f° or ΔF_f°), the former lists values of G with respect to a fixed temperature; i.e., using Barin we may say for (2.12) that

Table 2.4

Standard Free Energies of Reaction for Formation of Fluorides from MgF_2 and Refractory Metals at 1600°K (per mole F)

Reaction: $\frac{1}{2} MgF_{2(l)} + \frac{1}{x}M_{(s)} \longrightarrow \frac{1}{x}MF_x + \frac{1}{2}Mg_{(g)}$

	ΔG° kcal/mole F		
Species	**Barin [27],[28]**	**JANAF [19]**	**Notes**
$\frac{1}{5} TaF_{5(g)}$	26.096	no data	
$\frac{1}{6} ReF_{6(g)}$	71.458	no data	
*$\frac{1}{4} HfF_{4(?)}$	No data above 1100°K	no data	From Barin $\frac{1}{4} HfF_{4(s)}$, ΔG° = 15.823 at 1100°K Extrapolate 10-13 kcal/mole at 1600°K.
$\frac{1}{6} WF_{6(g)}$	48.701	47.350	For JANAF, from $\frac{1}{6}(\Delta F^\circ_{WF_6} - 3\Delta F^\circ_{MgF_2})$
$\frac{1}{2} MgF_{2(l)}$	-96.828	-98.988	Free energy of formation from elements in standard states, per mole F $\frac{1}{2}(Mg_{(g)} + F_{2(g)} \longrightarrow MgF_{2(l)})$

* *Touloukian claims that* $HfF_{4(s)}$ *sublimates at 873°K [46].*

$$\Delta G^{\circ} = [(1/2G_{Mg(g)} + (1/x)G_{MF_x}] - [(1/2G_{MgF_2(l)} + (1/x)G_{M(s)}] \qquad (2.13)$$

where the values of G are read directly from the tables. The high positive values of ΔG° from the table make it evident that the reactions will go backwards when the gaseous components start at standard pressure (1atm), but for a closed system starting with vacuum there will be small equilibrium pressures of the fluorides.

Table 2.5 lists free energies of formation for several possible refractory metal oxides. Unfortunately, data for these are quite spotty. Chang and Phillips surveyed data on refractory metal-oxygen systems for W, Mo, Ta, and Nb [35]. They found considerable confusion on the stability of various W oxides, particularly those of mixed valence between WO_2 and WO_3, but they did note the dominating stability of Ta_2O_5 in the Ta-O system.

Both Barin and JANAF give thermophysical quantities for the mixed valence oxides, $WO_{2.72}$, $WO_{2.90}$, $WO_{2.96}$, but listing them here would be excessive detail. One may note that the transformation $WO_{2(s)}$ to $WO_{3(s)}$ is favored when the oxygen partial pressure is above 1.075×10^{-9} atm (8.93×10^{-7} torr) at 1600°K.

The listing of free energies in both Tables 2.4 and 2.5 is per atom of fluorine or oxygen respectively. By doing this we see directly the relative "strengths" of the fluorine or oxygen bonds across compounds. In the case of oxygen, this can be translated into relative equilibrium partial pressures (lowest for the most positive free energy change). The data concerning HfO_2 are confirmed by the results of Liu, Inouye, and Carpenter in [36]. There, a

Table 2.5

Standard Free Energies of Formation of Oxides from $O_{2(g)}$ at 1600°K (per mole O)

	ΔG° (kcal/ $\frac{1}{x}$ mole oxide)		
Species	**Barin [27],[28]**	**JANAF [19]**	**Notes**
$\frac{1}{5}\ Ta_2O_{5(s)}$	-65.076	-65.020	
$\frac{1}{2}\ ReO_{2(s)}$	to 1300°K	no data	At 1300°K, ΔG°=-25.016 kcal/ mole from Barin
$\frac{1}{3}\ ReO_{3(s)}$	to 433°K	no data	
$\frac{1}{7}\ Re_2O_{7(s)}$	to 600°K	no data	At 298°K, ΔG°= -36.3 kcal/ mole ([34], p. 8)
$\frac{1}{2}\ HfO_{2(s)}$	-98.864	no data	At 298°K, ΔG°= -126.1 kcal/ mole ([34], p. 8)
$\frac{1}{2}\ WO_{2(s)}$	-36.604	-35.514	At 298°K, ΔG°= -61 kcal/mole
$\frac{1}{3}\ WO_{3(s)}$	-35.299	-35.256	At 298°K, ΔG°= -60.6 kcal/mole
$MgO_{(s)}$	-96.087	-96.530	
$MgO_{(s)}$	101.531	101.506	For formation by the exchange reaction $MgF_{2(l)} + \frac{1}{2}\ O_{2(g)} \longrightarrow MgO_{(s)} + F_{2(g)}$

The quantity "x" is the subscript of oxygen in oxide species.

tantalum alloy (Ta-8 wt. % W-2 wt. % Hf, or T111) exhibited formation of HfO_2 rather than Ta or W oxides when oxygen was diffused in at 1273°K.

In many problems of metallurgical thermodynamics, one is considering a situation in which boundary conditions can be set for a desired end, eg. the partial pressure of oxygen p_{O_2} over molten iron can be lowered to reduce hematite (Fe_2O_3) to other oxides until the oxide phase disappears altogether [37]. However, the present case is that of a closed system evolving to an equilibrium given a temperature (1600°K) and certain starting species (alloy, MgF_2, liquid, contaminants). This requires three sets of equations: reactions between species, gas-solution equilibrium for each species, and conservation of atoms.

Consider a system consisting initially of only molten MgF_2, and tungsten metal. Final conditions will be determined by four equilibria and one conservation equation, i.e.

$$3MgF_{2(l)} + W_{(c)} <=> WF_{6(g)} + 3Mg_{(g)} \qquad (2.14)$$

$$MgF_{2(l)} <=> MgF_{2(g)} \qquad (2.15a)$$

$$WF_{6(l)} <=> WF_{6(g)} \qquad (2.15b)$$

$$Mg_{(l)} <=> Mg_{(g)} \qquad (2.15c)$$

and

$$\frac{\text{total moles Mg}}{\text{total moles F}} = \frac{1}{2} \qquad (2.16a)$$

or

$$\frac{n^g_{MgF_2} + n^g_{Mg} + n^l_{MgF_2} + n^l_{Mg}}{6n^g_{WF_6} + 2n^g_{MgF_2} + 6n^l_{WF_6} + 2n^l_{MgF_2}} = \frac{1}{2} \qquad (2.16b)$$

The values of the molar numbers "n" in the liquid can be approximated as

$$n^l_{MgF_2} = X^l_{MgF_2}(n^l_{mg} + n^l_{MgF_2} + n^l_{WF_6}) \cong \frac{V^l}{v^l_{MgF_2}} \tag{2.17a}$$

$$n^l_{Mg} = X^l_{Mg}(n^l_{mg} + n^l_{Mg} + n^l_{WF_6}) \cong X^l_{Mg}\,\frac{V^l}{v^l_{MgF_2}} \tag{2.17b}$$

$$n^l_{WF_6} \cong X^l_{WF_6}\,\frac{V^l}{v^l_{MgF_2}} \tag{2.17c}$$

where "X" is mole fraction, V^l is volume of the liquid, v^l is molar volume of MgF_2 (m^3/mole). The parenthetical terms for mole numbers of Mg and WF_6 are considered negligible compared to that for the MgF_2, for which the mole fraction is assumed to be close to unity.

For the gas phase, with application of the ideal gas law, one may state

$$n^g_{MgF_2} = \frac{p_{MgF_2}V^g}{RT} \tag{2.18a}$$

$$n^g_{Mg} = \frac{p_{Mg}V^g}{RT} \tag{2.18b}$$

$$n^g_{WF_6} = \frac{p_{WF_6}V^g}{RT} \tag{2.18c}$$

where p is partial pressure, V^g is the gas volume, and R the universal gas constant. Using the molar quantity expressions in the conservation expression, (2.16b), results in

$$(p_{Mg} - 3p_{WF_6})\frac{V^g}{RT} = (3X^l_{WF_6} - X^l_{Mg})\frac{V^l}{v^l_{MgF_2}} \tag{2.19}$$

where terms involving X_{MgF_2}, p_{MgF_2} have dropped out.

Now the gas-solution equilibria merely state that ΔG_A for a member of the species "A" in going from the liquid solution to the gas phase is zero -- the chemical potential μ_A is the same for each. As shown in Lupis ([38], pp. 108-9) for moderate pressures, and with the assumption of an ideal solution, this implies

$$a_A = X_A = \frac{P_A}{P_A} \tag{2.20}$$

where a_A is activity in the liquid and P_A is the vapor pressure of pure liquid A at the temperature of interest. (This also applies to a solid solution, but with the additional criterion that P_A is over A in the same structure as the solvent.)

Applying the last equation in the present case, X^l_{Mg} and $X^l_{WF_6}$ may be replaced in (2.19) to result in

$$(r_V \frac{v^l_{MgF_2}}{RT} + \frac{1}{P_{Mg}})p_{Mg} = 3(r_V \frac{v^l_{MgF_2}}{RT} + \frac{1}{P_{WF_6}})p_{WF_6}$$

or

$$\frac{p_{Mg}}{p_{WF_6}} = \frac{3(r_V \frac{v^l_{MgF_2}}{RT} + \frac{1}{P_{WF_6}})}{(r_V \frac{v_{MgF_2}}{RT} + \frac{1}{P_{Mg}})} \tag{2.21}$$

where r_V is the volume ratio

$$r_V = \frac{V_g}{V_l} \tag{2.22}$$

and the units of the pressures are Pascals.

The equation (2.14) implies an equilibrium of the form

$$\Delta G^{\circ} = -RT \ln p_{WF_6} p_{Mg}^3 \qquad (2.23)$$

where the pressures are in atmospheres, if both the $MgF_{2(l)}$ and the $W_{(c)}$ are in the pure standard state for that temperature. Combining this with the last relation between p_{Mg} and p_{WF_6} gives the desired result.

To proceed one requires the vapor pressures P_{Mg} and P_{WF_6}, for which there are two methods of estimation (given that there are no direct data). These are as follows:

1. Integration of the Clausius-Clapeyron equation for condensed phase-vapor equilibrium, where the molar volume of the condensed phase is small compared to the vapor and the vapor behaves as an ideal gas, whence

$$\ln P - \ln P(T_0) = \int_{T_0}^{T} \frac{\Delta H_{evap}(T)}{RT^2}\, dT \qquad (2.24)$$

where

$$\Delta H_{evap}(T) = \Delta H_{evap}(T_0) + \int_{T_0}^{T} (c_p^{(v)}(T) - c_p^{(l)}(T))dT \qquad (2.25)$$

$\Delta H_{evap}(T_0)$ is most often available for the boiling point at one atmosphere (760 torr). In the case of Mg, $T_0 \cong 1378^{\circ}K$, $\Delta H_{evap}(T_0) \cong 30.5$ kcal/mol and $c_p^{(v)} = 4.968$ cal/mol-°K, $c_p^{(l)} = 2.75 \times 10^{-3}T + 8.86$ cal/mol-°K for the temperature range of concern. The result is $P_{Mg}(1600^{\circ}K) =$ 4.501 atm.

2. Equating $\mu_{Mg}^{(g)}$ to $\mu_{Mg}^{(l)}$ gives (using Lupis p. 109)

$$P_{Mg} = e^{\frac{\mu_{Mg}^{\circ(l)} - \mu_{Mg}^{\circ(g)}}{RT}} \quad \text{(atmospheres)} \qquad (2.26)$$

Now the JANAF tables list $\Delta G_f^\circ(T)$ for Mg in both liquid and gas states. It is of course zero for the gas in the standard state (1 atm) above the boiling point, but for the liquid is precisely the (excess) free energy in the numerator of the exponent, and is 4.826 kcal/mol at 1600°K. (This is $\Delta G^{\circ(l)} - \Delta G^{\circ(g)}$ when the equations for formation in either state are added to obtain $WF_{6(l)} <=> WF_{6(g)}$.) The result is $P_{Mg} = 4.567$ atm. Proceeding similarly, for WF_6 one can obtain $P_{WF_6} = 161$ atm by method 1 and 170 atm by method 2. Apply the pressures obtained by method 2 (in Pascals) with R = 8.314 J/°K-mole, $v^l_{MgF_2} = 2.599 \times 10^{-5} m^3$/mole (from Janz, [18]), and a volume ratio of 1.417 (from W-25 Re capsule to be described later). The result is $p_{Mg} = 5.856 \times 10^{-6}$ Pa (5.780×10^{-11} atm), $p_{WF_6} = 6.972 \times 10^{-5}$ Pa (6.881×10^{-10} atm).

For the case of reaction of MgF_2 with tantalum to form $TaF_{5(g)}$ (with vapor pressure 226 atm at 1600°K) one finds product pressures of $p_{Mg} = 0.2716$ Pa (2.681×10^{-6} atm) and $p_{TaF_5} = 13.46$ Pa (1.328×10^{-4} atm) at equilibrium.

Projection of the available free energy data for HfF_4 from 1100°K to 1600°K (see Table 2.4) indicates that it may be more reactive with MgF_2 than any of the other refractories considered here. This is interesting in view of the experimental reaults to be discussed in Chapter III. Rhenium, judging by the data in Table 2.4, should be less reactive than the other metals.

Formation of refractory oxides at high temperatures is clearly favored thermodynamically if oxygen is available as indicated in Table 2.5 as well as by long historical experience [32]. (Here again, Hf is most reactive.) As noted before, at high pressures and high temperatures, corrosion will be rapid and destructive. But even at low pressures, long term effects on ductility will occur in tantalum alloys.

In sum then, thermodynamic data indicates the stability of MgF_2 itself with refractory alloys.

2.2.5 Effect of Residual Moisture in Fluoride

The recent paper by Misra [13] has noted the possible results of residual water contamination of fluorides. According to that source, water present in a fluoride may lead to production of hydrofluoric acid (gas) which then can react (either in solution or in the free space of the container) with the metal container. For the particular case of MgF_2, the rapid formation of HF and MgO is supported by the comments of Mr. R. Sparrow of Optovac, Inc. [29]. One would have

$$MgF_{2(l)} + H_2O_{(g)} \longrightarrow MgO_{(s)} + 2HF_{(g)} \qquad \Delta G^\circ = 5.512 \text{ kcal/mole} \quad (2.27)$$

(Production of a hydrate of Mg, $Mg(OH)_2$, is also possible, but results in $\Delta G^\circ \cong 154$ kcal/mole, so it will be ignored here.)

Reaction with a metal can then proceed as in the following two examples:

$$W_{(s)} + 6HF_{(g)} = WF_{6(g)} + 3H_{2(g)} \qquad \Delta G^\circ = 101.2 \text{ kcal/mole} \quad (2.28a)$$

$$Ta_{(s)} + 5HF_{(g)} = TaF_{5(g)} + \frac{5}{2}H_{2(g)} \qquad \Delta G^\circ = 26.66 \text{ kcal/mole} \quad (2.28b)$$

Here it will be assumed that, following the ideal solution model noted earlier, solubility of the gasses H_2, H_2O, HF, in liquid MgF_2 at 1600°K can be ignored, while that of WF_6 and TaF_5 is not. That is, if the activity is given by

$$a_g \approx x_g \approx \frac{p_g}{P_g}$$

where x_g is mole fraction in solution, p_g is partial pressure, and P_g is vapor pressure, then for molecules with low boiling points, P_g will be very large and x_g negligible (Denbigh in [39] notes that above the critical temperature of a substance, the model can be used if integration of the Clausius-Clapeyron expression for vapor pressure is fictitiously extended). For the moment also, it is assumed that the solubility of magnesia (MgO) in the liquid fluoride is negligible, so that the oxide activity is close to one. In other words, any MgO that appears will immediately precipitate.

Sparrow, [29], states that it is difficult to determine moisture contamination levels in fluorides; however, for optical (high-quality) single crystal MgF_2, 100 mole ppm is a reasonable value. For a closed vessel, interior corrosion will be limited by this supply (i.e. 10^{-4} mole MgO per mole MgF_2 in (2.27)). Another result, however, will be production of the gasses noted in the above equations. These can easily pressurize the container to a value approaching or exceeding 1 atm, depending upon the ratio of MgF_2 to free volume.

For example, using (2.27) and (2.28), one can show that for the test capsules noted earlier (which are ~40% filled with MgF_2) internal pressures

will be (in Pa)

$p_{HF} = 2.16 \times 10^4$
$p_{H_2} = 12.0$
$p_{H_2O} = 2.16 \times 10^4$
$p_{WF_6} = 8.90 \times 10^{-2}$
$p_{total} = 4.780 \times 10^4$ (0.4717 atm)

} for Tungsten

$p_{HF} = 4.72 \times 10^3$
$p_{H_2} = 5.56 \times 10^4$
$p_{H_2O} = 1.24 \times 10^3$
$p_{TaF_5} = 811$
$p_{total} = 6.24 \times 10^4$ (0.615 atm)

} for Tantalum

(This is with vapor pressure P_{TaF_5} = 225 atm derived as before.)

If the capsules are assumed to be 95% filled, considerably higher pressures are found

$p_{HF} = 1.26 \times 10^5$
$p_{H_2} = 377$
$p_{H_2O} = 8.94 \times 10^5$
$p_{WF_6} = 0.113$
$p_{total} = 1.02 \times 10^6$ (10.1 atm)

} for Tungsten

$$p_{HF} = 2.81 \times 10^4$$
$$p_{H_2} = 1.93 \times 10^6$$
$$p_{H_2O} = 4.43 \times 10^4$$
$$p_{TaF_5} = 862$$
$$p_{total} = 2.00 \times 10^6 \text{ (19.8 atm)}$$

} for Tantalum

Note that the significant pressure increases are for those gasses assumed to be insoluble in the liquid. If MgO activity were lowered (i.e. if the magnesia were below saturation in the molten fluoride) then more of the water contaminant would be consumed, increasing the amount of HF available for reaction with the metal. That this is so here is suggested by the ideal solubility of MgO in any liquid for the given temperature ([39], p. 267).

$$\ln x_s = \frac{L}{R}\left(\frac{1}{T_m} - \frac{1}{T}\right) \qquad (2.29)$$

where x_s is the mole fraction solubility of the magnesia, R the gas constant, T_m the magnesia melting point (2915°K). This comes to about 7% when the heat of solution L is approximated by the heat of fusion (77,330 J/mole). This solubility is very high compared to the amount of MgO that can be produced with the available oxygen. If one assumes all the H_2O to be consumed, then the total pressures come to 18.9 atm and 20.2 atm for the tungsten and tantalum tubes respectively (at 95% filled).

Along with reaction of the trapped moisture with the fl ride to produce HF and metallic fluorides, there may also be interaction of the water and the metal directly to produce metallic oxides. Using free energy change (per mole H_2O) as a criterion, the most dominant would be

$$W_{(s)} + 3H_2O_{(g)} <=> WO_{3(s)} + 3H_2 \qquad \Delta G^\circ = 7.930 \text{ kcal/mole} \qquad (2.30a)$$

$$W_{(s)} + 2H_2O_{(g)} <=> WO_{2(s)} + 2H_{2(g)} \qquad \Delta G^\circ = 2.677 \text{ kcal/mole} \qquad (2.30b)$$

$$2Ta_{(s)} + 5H_2O_{(g)} <=> Ta_2O_{5(s)} + 5H_{2(g)} \qquad \Delta G^\circ = -135.67 \text{ kcal/mole} \qquad (2.31)$$

Ignoring the oxide solubilities, this suggests that the tantalum container would be more apt to react with the water than would the tungsten one.

However, there is another consideration that must be folded into this analysis. Hydrogen gas produced in the container is likely to diffuse out within a short period due to a very high mobility in the metal. [40] notes values of the diffusion coefficient D of 2.21×10^{-4} cm^2/sec (2.21×10^{-8} m^2/sec) for W and 2.98×10^{-4} cm^2/sec (2.98×10^{-8} m^2/sec) (extrapolated) for Ta around the melting point of MgF_2.

An order of magnitude estimate of the time required for a significant reduction in the hydrogen pressure in the container can be made as follows. Start with Fick's equation for diffusion,

$$\frac{\partial c}{\partial t} = D\frac{\partial^2 c}{\partial X^2} \qquad (2.32)$$

where c is the concentration of atoms or moles per unit volume of the diffusion medium, x is distance, and t is time. The time required to establish a linear concentration gradient (if we had a steady state concentration at either end) is of the order

$$\Delta t \sim \frac{(\delta)^2}{D} \qquad (2.33)$$

where δ is the metal thickness. For the present case (the capsules described in the next chapter), $\Delta t \approx 13.5$ sec for Ta and 7.5 sec for W. So only a short time is required to establish a steady state. One is tempted to assume that the time to reduce the internal pressure will be relatively large, and thus a quasi-steady model may be applied, i.e. there will be a succession of linear concentration gradients of lower slope as the internal pressure is reduced. With $\frac{\partial c}{\partial t} = 0$, the expression for the concentration as a function of position "x" in the wall with δ the total thickness is

$$c = c_o(1 - \frac{x}{\delta}) \tag{2.34}$$

where c_o is the hydrogen concentration just within the inner wall. Then the flux through the wall J is related to the concentration gradient by the general expression

$$J = -D\frac{dc}{dx} \tag{2.35a}$$

which, using (2.34), would give

$$J = \frac{Dc_o}{\delta} \tag{2.35b}$$

Now we relate the H_2 pressure in the interior of the container, p_o, to the concentration of hydrogen within the inner wall surface, c_o. It is clear from any number of references that hydrogen molecules must first be broken into atoms and then go into solution before diffusing through the metal. Similarly, they must come out of solution at the other end. DeVan asserts that these processes should not significantly affect the time required for hydrogen leakage at the temperature of interest. So, the hydrogen concentration driving the diffusion process is assumed to be directly related

to the interior pressure p_o as

$$c_o = \frac{p_o}{RT} A \tag{2.36}$$

where R is the universal gas constant and A is Avogadro's number.

The values of p_o and thus c_o (formally incompatible with the earlier assertion that $\partial c/\partial t = 0$) are now taken to vary with time as the gas leaks out. Then interior pressure is related to flux by using the relation

$$A_r J dt = -V dc_o \tag{2.37}$$

along with (2.36) applied in the differential form to the right side and in the form shown to (2.35b) which is inserted in the left. Then cancelling terms one obtains

$$\frac{dp_o}{dt} = \frac{-A_r D}{\delta V} p_o = \frac{1}{\tau} p_o \tag{2.38}$$

Here A_r is the container wall area, V the interior volume. For a cylindrical container of radius r_w, the value of the time constant τ is expressible as

$$\tau = \frac{r_w \delta}{2D} \tag{2.39}$$

For the test cylinders described in the next chapter, the value of τ comes to 28 sec for the W cylinder and 34 sec for the Ta. So the assumption of a quasi-steady diffusion was a bit rough, but the main point is that the contained pressure should be significantly lowered within a few minutes. (For comparison, from Figure 34, p. 99 of [32], the perm ation rate for H in Nb at [through 1mm thick metal, with H_2 pressure = 1atm] temperature, shows a loss of 0.0054 mole/hour and there are only 4.17×10^{-6} moles present in the partly filled cylinders. The rate for loss through W is shown to be about 2 or 3 orders of magnitude less by the same author.)

The consequence of this will be that the reactions (2.27) and (2.25a) or (2.30) or (2.31) will indeed proceed to completion, that is, that the hydrogen

will be drained off and the water vapor used up to produce fluoride and/or oxide reaction products. The interior pressure will depend upon the final thermodynamic balance between these products. (Of course, the reaction kinetics will determine when this balance is reached.)

By combining the previously stated equilibria of this section so as to eliminate the hydrogen, we have:

$$3MgF_{2(l)} + WO_{3(s)} <=> 3MgO_{(s)} + WF_{6(g)} \qquad \Delta G^{\circ} = 109.8 \text{ kcal/mole} \qquad (2.32a)$$

$$3MgF_{2(l)} + \frac{3}{2}WO_{2(s)} <=> \frac{1}{2}W_{(s)} + 3MgO_{(s)} + WF_{6(g)} \qquad \Delta G^{\circ} = 109.8 \text{ kcal/mole} \qquad (2.32b)$$

$$MgF_{2(l)} + \frac{1}{5}Ta_2O_{5(s)} <=> MgO_{(s)} + \frac{2}{5}TaF_{5(g)} \qquad \Delta G^{\circ} = 21.18 \text{ kcal/mole} \qquad (2.33)$$

Qualitatively, the result must be a decrease in the internal pressures relative to the results with metal oxides but without H_2 loss, since the gas species involving hydrogen have been "pulled out."

Considering the tantalum equilibrium in the last equation, if the solid species are both present (and we ignore their solubility) at equilibrium so their respective activities are unity, then the required equilibrium pressure for $TaF_{5(g)}$ is 6.013×10^{-3} Pa. By conservation of oxygen and of the Mg to F ratio, this implies that there are 1.658×10^{-11} mole of solid MgO and 4.706×10^{-7} mole Ta_2O_5 in the partially filled cylinder. Again, ideal solubility of TaF_5 is assumed, as well as an ideal gas in the empty space.

In other words, we say that

$$\frac{n^{l}_{MgF_2} + n^{g}_{MgF_2} + n^{s}_{MgO}}{2n^{l}_{MgF_2} + 2n^{g}_{MgF_2} + 5n^{g}_{TaF_5} + 5n^{l}_{TaF_5}} = \frac{1}{2}$$

$$2n^{s}_{MgO} = 5(n^{g}_{TaF_5} + n^{l}_{TaF_5}) \tag{2.34a}$$

or

$$n_{MgO} \approx \frac{5}{2}\left(\frac{V^{g}}{RT} + \frac{V^{l}}{v_{MgF_2}} \frac{1}{P_{TaF_5}}\right)p_{TaF_5} \tag{2.34b}$$

and

$$5n^{s}_{Ta_2O_5} + n^{s}_{MgO} = n_{os} \tag{2.35a}$$

$$n_{Ta_2O_5} = \frac{n_{os} - n^{s}_{MgO}}{5} \tag{2.35b}$$

where n_{os} is the amount of oxygen we start with given the initial contamination with water. As determined by (2.33) and the assumed activities, the equilibrium pressure of $TaF_{5(g)}$ must be the same in the 95% filled cylinder as in the partially filled one, though the amounts of the oxides differ (3.862×10^{-11} and 1.177×10^{-6} mole for MgO, Ta_2O_5 respectively).

A similar situation, judging by the standard free energy changes, should obtain for the tungsten cylinder. By writing only (2.32) and (2.33) we have assumed that the presence of the gasses Mg, F_2, O_2 can be ignored in both cylinders. A consideration of the equilibria for formation of the oxides will show that this assumption is reasonable. The conclusion from the last calculations would be that the major constituent of the gas in the cylinders will be the vapor of MgF_2, with a pressure of 30.4 Pa at 1600°K ([18], p. 387).

The equilibria stated in (2.33), (2.34) will, however, be shifted if the oxides are sufficiently soluble in the MgF_2 that they are below their solubility limits. The activities of the oxides in solution in the simplest model would be given by

$$a_i = \frac{X}{X_{sat}} \approx \frac{n_i}{n_{i_{sat}}}$$

where the mole numbers may substitute as above when X, X_{sat} are small. The values of solubility given by (2.29) are $X^{sat}_{MgO} = 0.0726$ and $X^{sat}_{Ta_2O_5} = 0.0211$. There is far too little oxygen available to reach these limits. If again one allows for the solubility of TaF_5 in the liquid, one obtains (in the tantalum case) pressures for that gas of 797 and 850 Pa in the partially and 95% filled cylinders respectively.

It is reported by the manufacturer that tests on the Optovac MgF_2 showed a general oxide solubility of ~250 ppm, but they consider this number to be of questionable reliability. Application of this to find the internal pressures as outlined in the previous paragraph was made; the results are TaF_5 pressures of 38.6 and 40.3 Pa for the partially and 95% filled tubes.

Despite these uncertainties, it appears that the diffusion of hydrogen will keep water contamination requirements on the MgF_2 at levels currently available from manufacturers.

CHAPTER III

CORROSION TESTS

3.1 Introduction

To obtain data confirming the theoretical compatibility of molten MgF_2 in refractory metal containment a high temperature vacuum furnace was designed and constructed. Clearly it was impractical to test the materials for ten years (> 80,000 hrs.). As noted before the LiF compatibility tests had run for 5000 hours (~7 months). A goal of 2000 hours (~83 days) was set here, and was exceeded. Such relatively short tests compared to system lifetime are at least coarse screens of compatibility. With close examination of the metal surfaces exposed to the substance contained one can reasonably make projections over the system life. This was done both in the LiF work and in the more recent tests by Misra, which were carried out for 100 and 500 hours [13]. Of course, one must be cautious in making such projections since contaminants peculiar to the sample preparation may be responsible for apparent corrosion problems.

3.2 Sample Preparation

As noted above, the alloys ASTAR 811C and W-25Re were supplied by courtesy of ORNL. From a local supplier MgF_2 was purchased in macroscopic crystalline form. This was used rather than a powder to reduce adsorbed water and oxygen. The manufacturer stated that total impurity levels in the crystal were probably below 100 molar parts per million. The crystals were broken into a size that would fit into the tubing, then were cleaned with acetone,

weighed out and put into separate pyrex containers. Thermoelectron Corporation performed assembly of the test capsules shown in Figure 3.1 after the metal was cleaned with solvent.

The tubing had been manufactured by drilling in the case of ASTAR and by extrusion in the case of W-25Re. On the internal wall of the ASTAR were visible short (< 2mm) dents (< ~.1mm depth) arranged in approximately circumferential clusters, evidently formed when the drill caught on the surface. The outer surface of the ASTAR showed a dull polish with a barely visible (by unaided eye) scratch pattern while its inner wall showed slightly deeper circumferential scratches. The W-25Re inner wall exhibited clusters of adjacent longitudinal scratches with a maximum length of about 6 mm and a maximum depth approaching 1/4 of the wall thickness. The W-25Re cylinder surface was brighter and more finely polished than the ASTAR's. The outer surface showed some faint longitudinal scratches; the inner one showed variable but generally circumferential scattered scratches of apparently greater depth than those on the outside. Both types of alloy showed considerable variation in wall thickness longitudinally and circumferentially. For the ASTAR this variability exceeded ~50%; for the W-25Re it was less than ~20%.

The W-25Re material had to be cut by electro-discharge machining. Both capsules were electron beam welded, which encapsulated the $\sim 10^{-5}$ torr (1.33×10^{-3} Pa) atmosphere of the welding chamber. (This level of pressure was relatively good; it was the result of a specially requested overnight pumpdown of the system.) As indicated in Figure 3.1, two W-5Re/W-25Re thermocouples were welded to each capsule. Also, a small piece of the

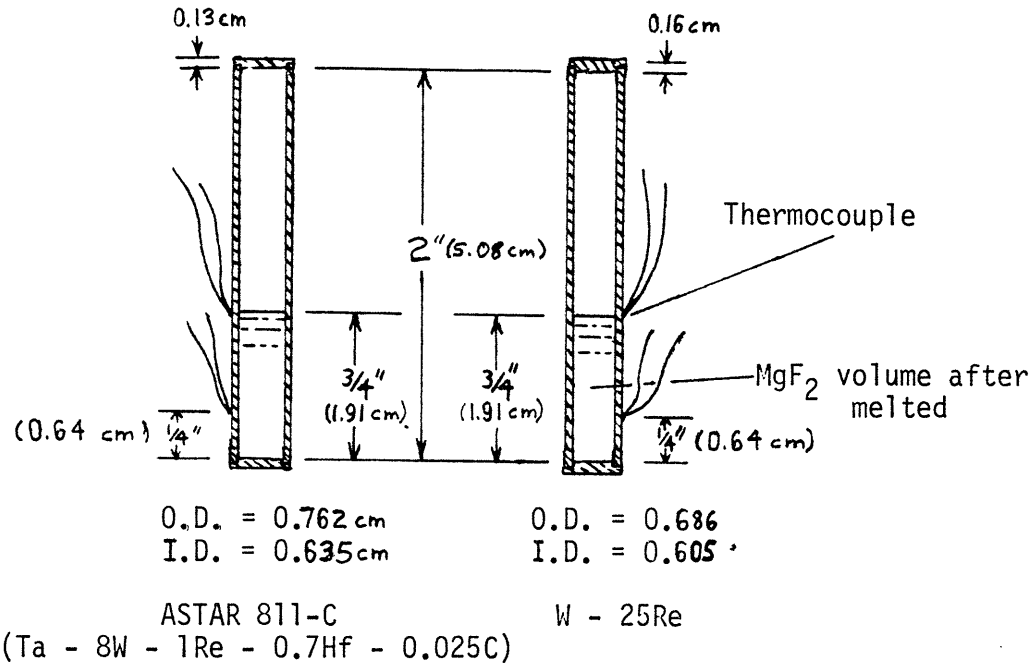

Figure 3.1 Test Capsule Configuration.

endplate material (< ~5 mm. in any dimension) was put inside to provide a sample further shielded from the furnace environment, if needed.

3.3 Vacuum Furnace

3.3.1 Design and Construction

Work on the test capsules run in parallel with design and construction of a vacuum furnace with which to test them.

[24] recounts the stringent contamination requirements that were imposed on high temperature vacuum tests of niobium and tantalum alloys by ORNL. The motivations for these conditions were to avoid two possible problems caused by interstitial oxygen contamination: (1) embrittlement and, (2) intergranular attack by lithium and boiling potassium. The intended applications of the alloys tested were space nuclear reactor systems.

The following quote conveys the magnitude of the problem encountered. It required...

> "...bakeable, cold-wall chambers pumped by ion-sputtering, titanium sublimation or turbomolecular pumps....Even with this equipment...the major problem was to control the desorption of oxygen from heater surfaces, reflective insulation and vacuum chamber accessories so that the bulk of this oxygen was picked up by the vacuum pumps and not the refractory metal test components. In many cases the refractory metal components were wrapped with tantalum, molybdenum or titanium foil to effect a mechanical barrier between the component and the chamber environment. The bakeout cycle and heat-up of the test system were controlled to limit the vacuum atmosphere to $< 1.3 \times 10^{-6}$ Pa (10^{-8} torr)

once the system had reached a temperature of 450°C. After the system operating temperatures were attained, the steady-state ambient pressure in the vacuum chamber was usually well below 1.3×10^{-6} Pa (10^{-8} torr) and hydrogen was the dominant species in the residual gas."
([24], p. 78)

This information was conveyed orally to the present author by Mr. DeVan of ORNL before the publication and distribution of [24] in January 1984. Obtaining a new vacuum system to satisfy these criteria would have been prohibitively expensive. In an MIT laboratory there was a surplus system that had historically attained pressures in the "mid- 10^{-8} torr range" (1.33×10^{-6} Pa). The bell jar was bakeable, but the seals were not, as they used rubber rather than copper O-rings. Pumping was by a diffusion pump using 304 silicon fluid and the baffles (traps) separating the pump from the chamber used open loop LN_2 cooling. Mr. DeVan's opinion was that this system could be employed usefully, particularly if the test samples were covered in protective foil.

After considerable refurbishment of the vacuum system, including conversion of the baffle cooling to a closed freon loop, the furnace shown in Figure 3.2 was constructed. The core of the furnace is a tantalum frame and heating elements that were obtained on indefinite loan from ORNL. Surrounding it are layers of tantalum and molybdenum (as insulating radiation shields) sheet and a water cooled copper jacket.

Two feed-throughs allow for as many as 12 high temperature (W-Re) thermocouples. There is a feed-through for lower temperature thermocouples, and two commercially constructed watercooled power feed-throughs bolted to adapter rings. The remaining three feed-throughs are for the coolant water, roughing pump and ion gauge.

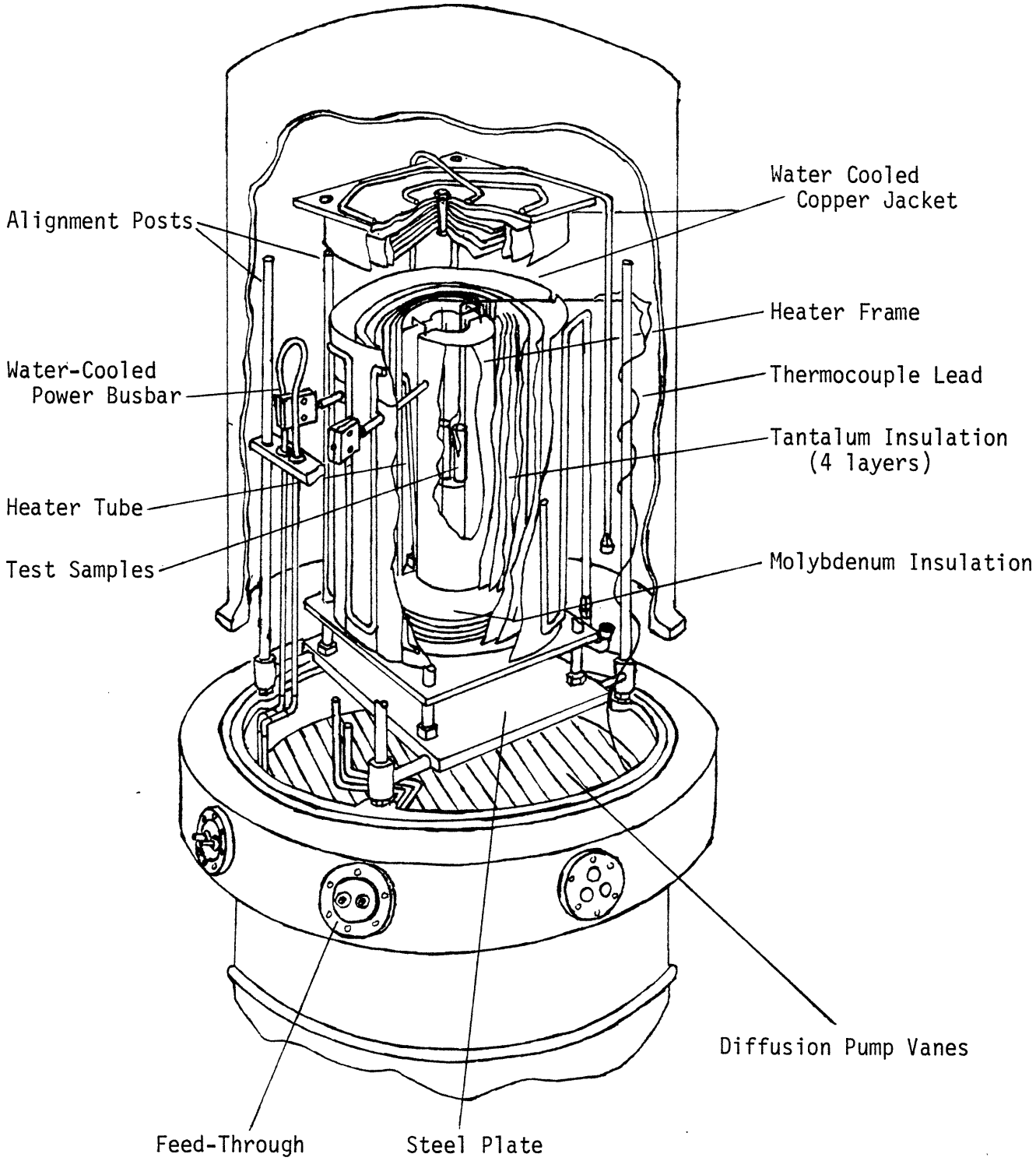

Figure 3.2 Vacuum Furnace Configuration.

A substantial leak of air or water into the vacuum while the furnace is hot would cause rapid oxydation of the metal parts. In case of a pressure jump the ion gauge, diffusion pump and heater power are cut off. Another interlock shuts down the latter two in case of a significant drop in coolant water flow. The 1/2" thick stainless steel plate supporting the furnace alignment rods provides protection of the diffusion pump in the event of catastrophic melting.

There are two water filters in parallel in the supply line so that filters can be replaced during system runs. The Hewlett-Packard (HP) power units are operated as current controllers within a set voltage limit. (They may also be operated with voltage controlled and current limited, but the furnace resistance is too low for that to be practical.) They would indicate a voltage drop if a short circuit occurred, and the furnace is grounded except for the heating elements.

3.3.2 Testing of Furnace

To test the furnace system two types of thermocouple were used. Some were of high temperature W-26Re/W-5Re and others were of iron-constantan. Of the former, one was bare, with its tip resting on the platform of the sample holder frame, another was clipped to the end of a heater frame, and the third was clipped to one end of the outer molybdenum shield (Figure 3.3). One of the low temperature type was clipped to the side copper jacket and another held to the bottom copper plate under a furnace frame support bolt.

Some oxydation of the molybdenum parts took place due to a water leak, but significant portions of the oxydation products evaporated under heating.

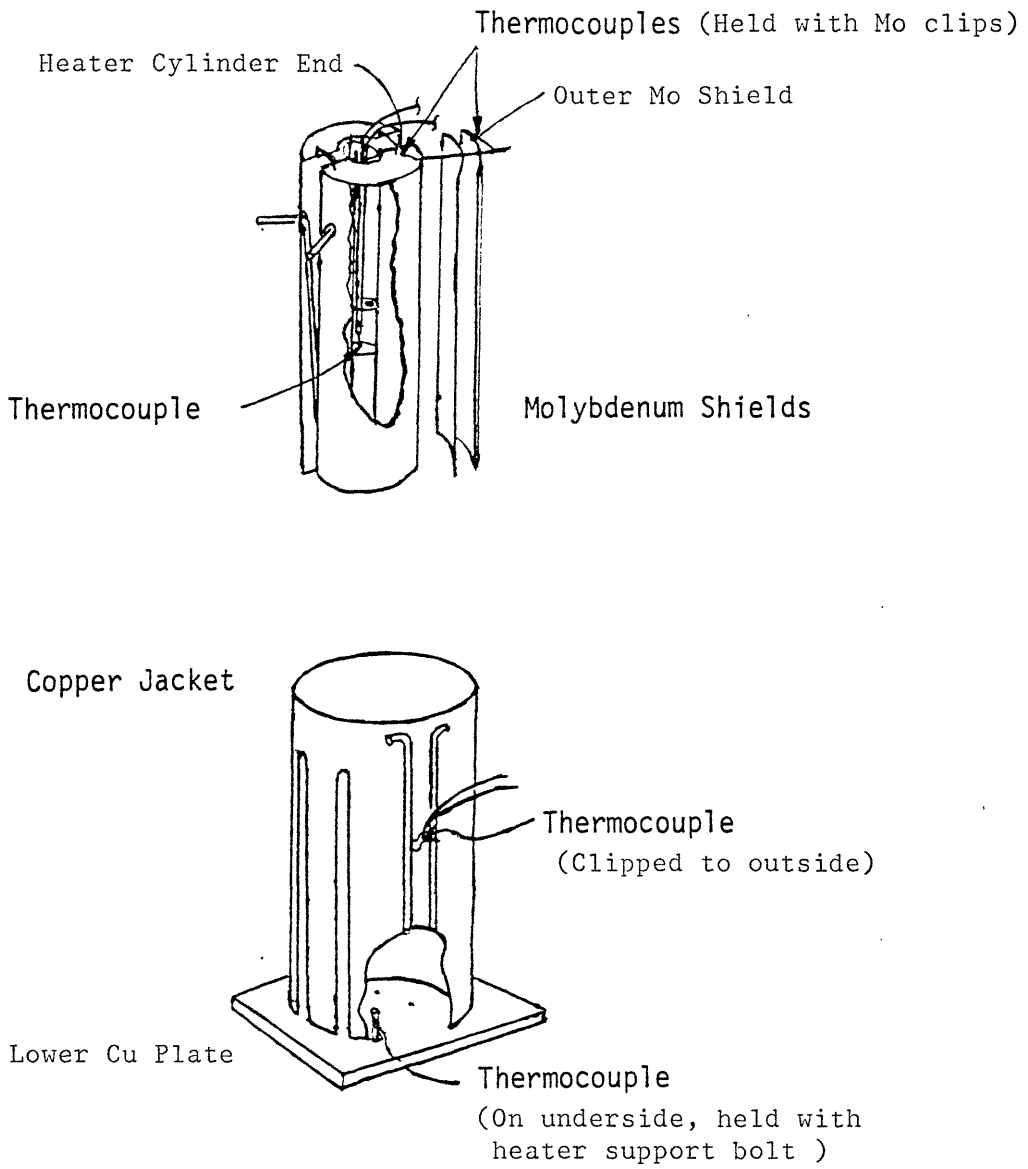

Figure 3.3 Placement of Thermocouples for Furnace Tests

Temperature and power data were recorded by hand for two furnace test runs. A particularly large amount of outgassing occurred during the first run shown in Figure 3.4, and the power was turned off as the pressure climbed into the 10^{-4} torr (1.33×10^{-2} Pa) range. (The pressure meter reads directly in torr.) With this test was noted a lower than expected heater resistance and there was some concern about being able to reach the MgF_2 melting point. A few days later (the diffusion pump was off during most of that time) a proof-test with little data recorded showed that this temperature could be reached.

Some days afterward, the recorded run shown in Figure 3.5 was performed. Considerably less outgassing occurred this time. (Again the diffusion pump had been off between tests.) From the pattern of up-down pressure changes in Figure 3.5 one can hypothesize that outgassing occurred in stages as the radiation shields heated up. For use with test samples, the heating was done more slowly to minimize outgassing. (The thermocouple error bar shown is given by the factory, and does not include set-up errors.)

When operating at peak power, the furnace draws ~2.72 kW at 78A, 35V from the two HP6479 DC power supplies. The outer molybdenum radiation shield is at 995°K and the end of the heater frame at 1406°K; the bare center thermocouple reads 1583°K (no samples present).

3.4 Long Duration Corrosion Test

3.4.1 Preparation

Two samples -- one of each type alloy -- were cleaned with trichlorethylene and acetone and mounted into the loading frame (Figure 3.6, a photograph actually taken after the furnace test). Ceramic insulators for the

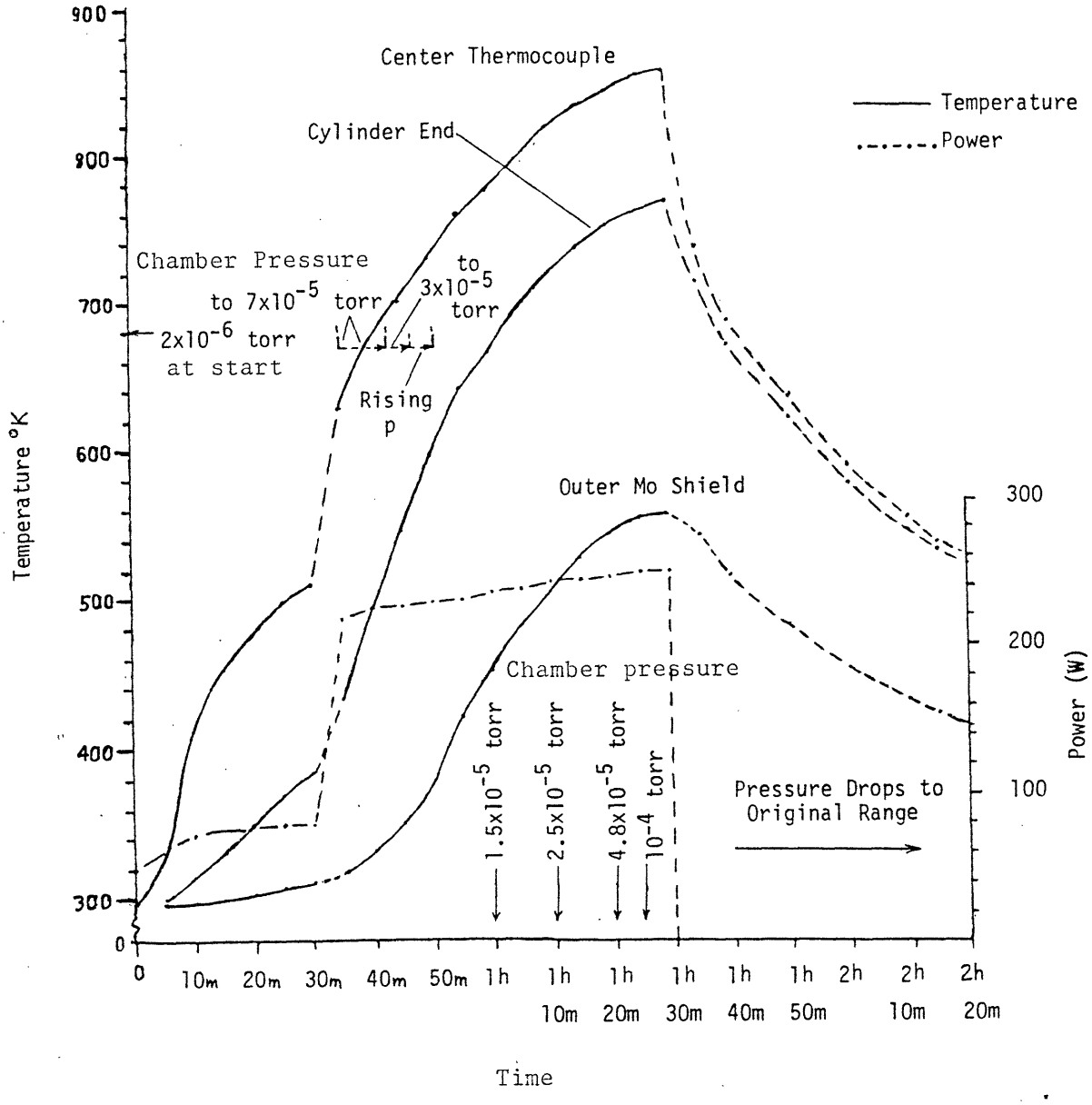

Figure 3.4 First Test of Furnace (No samples)

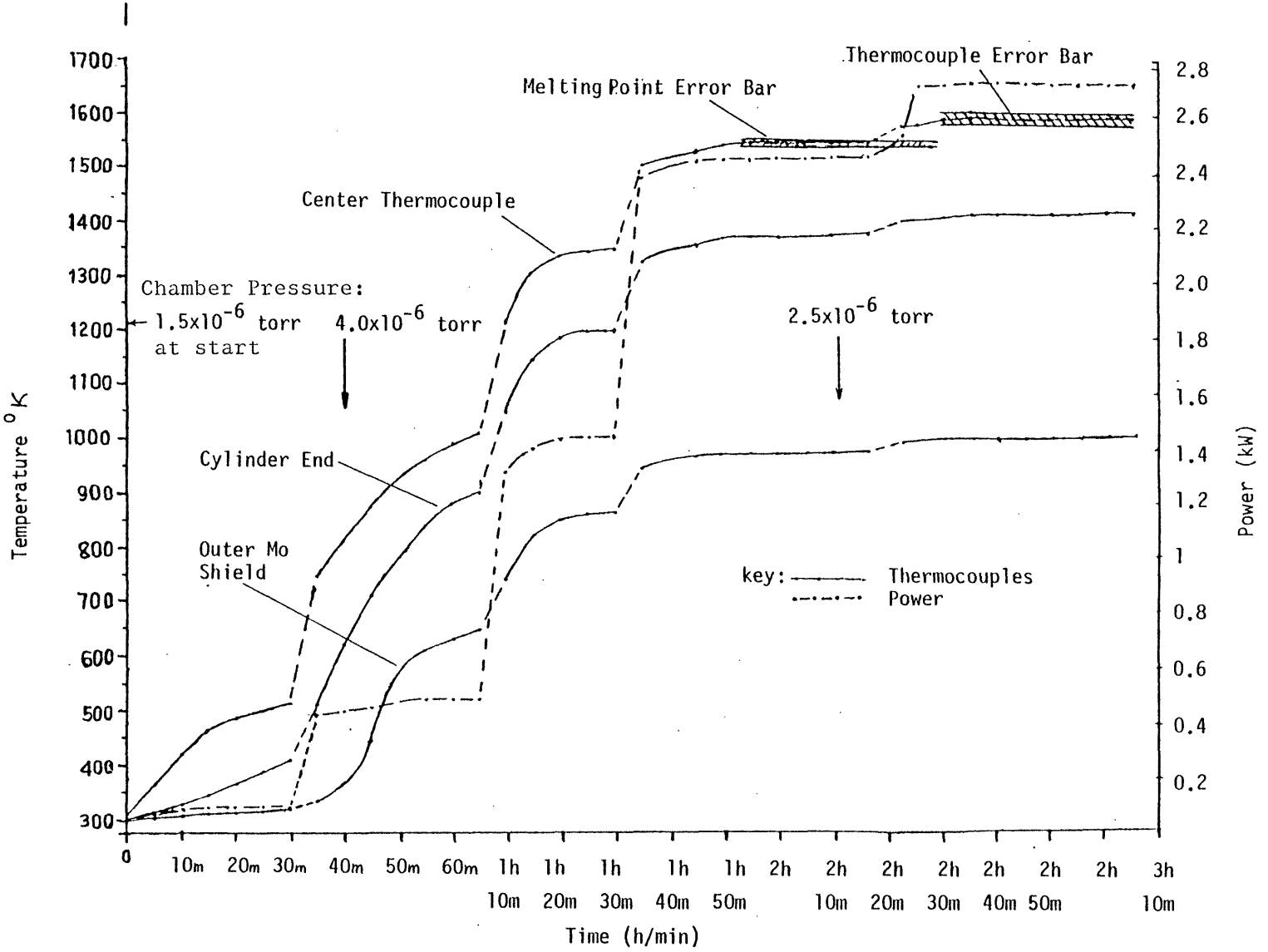

Figure 3.5 Second (Recorded) Test of Furnace (No samples)

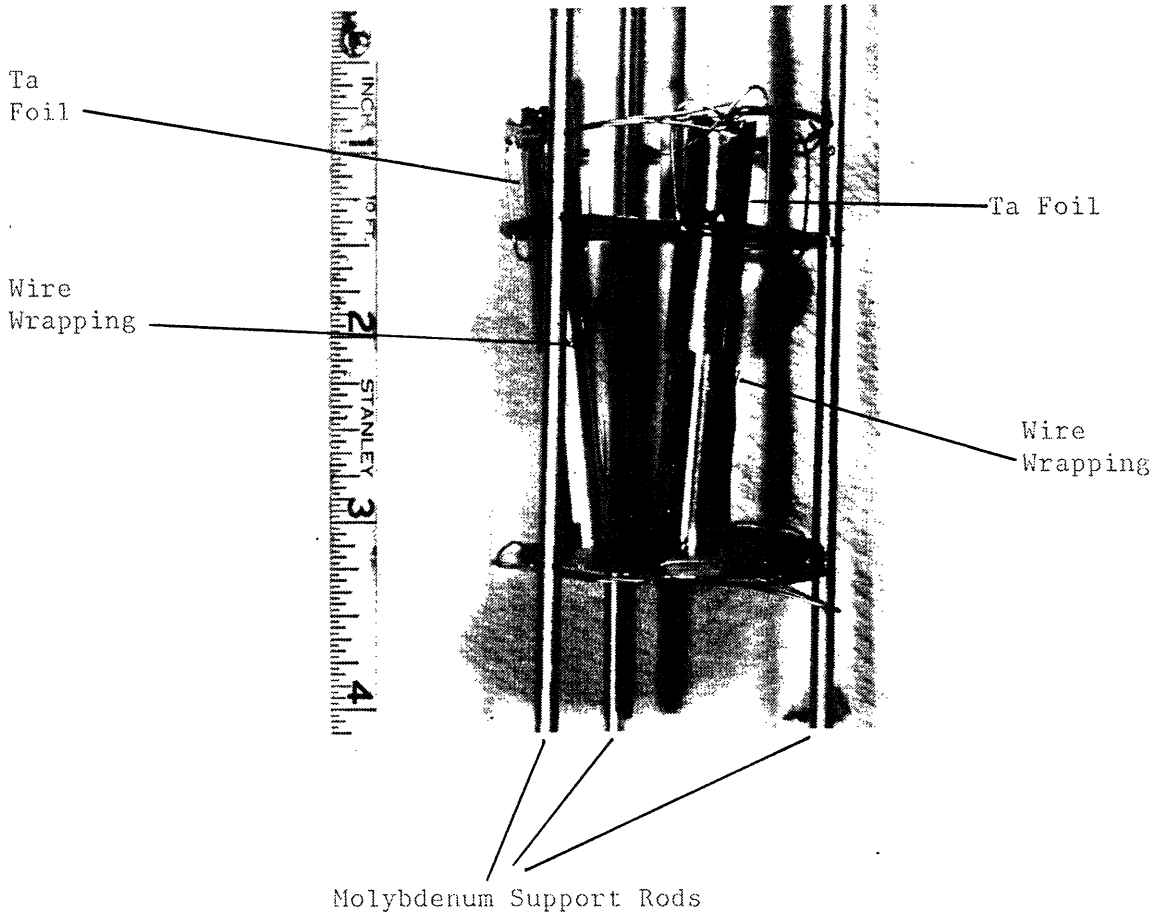

Figure 3.6 Samples Mounted in Frame, ASTAR at Right, W-25Re at Left (Photo taken just after long duration test)

tungsten thermocouple wires were first cleaned in boiling nitric acid. During the threading of the very brittle wire through the insulators, the upper thermocouple became detached from the ASTAR sample.

Thermoelectron Corp. had wrapped several turns of tungsten wire around each sample near the center to keep the thermocouple leads from breaking off. It had been intended to remove this other wire before installing the samples in the furnace, but due to concern about lead breakage, it was not removed. This wire probably shorted the thermocouples. In the absence of any resistance in the wrapping wire, the effect would be to cause both thermocouples to read out the temperature at the wrapping (see Appendix B).

In view of the previously noted warnings concerning the effects of outgassing on tantalum alloys, some tantalum foil (1 mil thick) was wrapped around the samples. The upper half of each cylinder was wrapped to provide comparable gas exposure to part of both. The lower half of the ASTAR was partially covered to see if there was any variation in metal corrosion with different gas exposures *and* the MgF_2 together.

Once the extension wires were welded in place, the frame containing the samples was loaded into the furnace and the vacuum system started. Some effort was expended trying to achieve vacuum pressures below the 10^{-6} torr (1.33×10^{-4} Pa) range. Outgassing was allowed to go on for several weeks, including some bell jar heating. It became evident that condensation on the refrigerated vanes was controlling chamber pressure.

3.4.2 Operations

To start the long duration test, furnace power was applied in steps over a period of days. In addition to avoiding a pressure peak, this was done to prevent thermal shock that might cause thermocouple detachment. At about 11:00 am on 21 January, the power setting was turned to 70A, then to 76A by 1:35 in the afternoon. The setting was at 76A until the early afternoon of 27 January. On that date, the power units developed a rapping noise and output instability. Current was reduced to 70A, at which the problem did not recur. Due to thermocouple recordings made the previous day, it was clear that the MgF_2 was melted at that level. (This will be explained in the next chapter.)

A water shutdown for the building had been scheduled for two days later. The diffusion pump and furnace power could not remain on, so the system was shut down to begin diagnostic tests of the power supplies for which a "dummy" load using power resistors was constructed. The tests showed that the components were operating within their specified range. Nonetheless, for safety, the air filters were cleaned and it was decided not to operate above 70A for long periods.

A broken ion gauge filament made it necessary to open the chamber long enough to remove the unit and effect a repair; meanwhile, a dry nitrogen backfill was used to minimize moisture uptake. After a reheating process over several days, at 10:15 am on 18 February current was set at 68A for the remainder of the duration test (except for cycling through the melting range, as explained later).

At 11:10 am on 20 February an anomalous event in the MIT power system caused all power to the building to shut down for 12 minutes. By the time the

power returned, the pressure in the chamber was above 10^{-4} torr (1.33×10^{-2} Pa), the ion gauge limit, but below 10^{-2} torr (1.33 Pa), the machanical gauge limit. The temperature of the core platform thermocouple (unattached to the samples) had dropped to about 810°K. By early that afternoon, the furnace was once again operating at the 68A level.

Chamber pressure generally cycled with the refrigeration, staying approximately in the range $1.2\text{-}2.5 \times 10^{-6}$ torr ($1.60\text{-}2.67 \times 10^{4}$ Pa). For nearly a month the refrigerator did not cycle; as a consequence, pressures fell and stayed in the range from about .5 to $.7 \times 10^{-6}$ torr ($6.67\text{-}9.33 \times 10^{-5}$ Pa). No adjustments had been made to the system, and it reverted to its previous behavior.

On May 11 at approximately noon, current was turned down to 50A. Thermocouple measurements showed the phase transition to solid in both cylinders as the heater was cooled. The power was reduced over the next two days as some final thermocouple measurements were taken. At 10:00 am on 14 May all power to the heaters was shut off.

3.4.3 Temperature and Time Data

In Table 3.1 is a summary of temperature data as recorded at various amperage (power) levels of the furnace. The table also includes times at these levels, which are not necessarily identical with times at the respective temperatures; transients of temperature when changing power levels were not always recorded on a thermograph, and when recorded the times required are lumped into the times at the equilibria for the power levels set. For example, if the power level were at 50A and turned up to 60A, the time at 60A

Table 3.1

Equilibrium Temperature Data -- Compatibility Test

			W-25Re		ASTAR			
Amps	**Volts**	**Power**	**Lower**	**Upper**	**Lower**	**Center**	**Time at this level**	**Estimated time accuracy**
78	34.9	2722					5 min	
76	33.2	2523	1602	1643	1653	1583	142.38 hr	± 30 min
75		2475	1591	1632	1640	1564	3.66 hr	± 5 min
70	29.75	2083	1530	1569	1577	1507	12.15 hr	± 45 min
68	28.3	1924	1507	1543	1562	1480	1926 hr	± 1.5 hr
65	26.75	1739	1468	1504	1514	1449	6.733 hr	± 15 min
60	23.6	1416	1402	1434	1448	1383	8.967 hr	± 15 min
55	20.8	1144	1335	1362	1375	1313	7.011 hr	± 15 min
50	18.1	905	1264	1288	1301	1241	75.633 hr	± 1 hr

NOTES:

- 2.83 hr ± 5 min at 74A, and ~2 hr 30 min which is uncertain (either 70A or 76A)
- Total time above melting point: 2089 hr ± 1 hr (from thermocouple detected meltings)
- Center thermocouple was resting on sample platform unattached to either sample cylinder

would be counted from the moment the setting was changed. Changes in the power levels were made intermettantly throughout the long duration test to investigate the melting/freezing cycle (see Chapter 4). The time given in the table as minimum in the melted condition is derived directly from the melting/freezing data as recorded. Temperature variability at a given power setting has several possible sources:

a. *Difficulty in setting amperage of power units.* Fractional amperage levels had to be estimated by eye and this was impeded since the units were not operating perfectly in parallel (the slaved unit put out slightly less current than the other). A marking system superimposed on the ammeters eventually allowed settings that gave temperatures consistent to within ~1-2°K.

b. *Voltmeter and recorder drift.* Calibration was done as often as possible but an error bar of 1-2°K is probable.

c. *Cooling water temperature variation.* Cooling water temperature varied by about ± 5°K during furnace operation. For parallel plate radiative heat transfer in the furnace this would have negligible effect on the core (cylinder thermocouple) temperatures.

d. *Change in thermocouple electrical characteristics over time.* This is possible due to metallurgical changes in the thermocouples. At the end of the duration test they were even more brittle than at the start.

In all, however, variability at given power levels was less than ~± 3°K when care was taken with factors a and b.

These variable effects are superposed over other, more nearly constant sources of error. In particular, one sees a difference in temperature between the upper and lower thermocouples on the W-25Re cylinder, and this is unexpected given that they were shorted together, as noted above. Possible reasons for this are the following:

a. *Variability in calibration of thermocouple wire in manufacture.* The producer of the thermocouple wire (Omega) states that variability may be as much as ± 1% relative to the operating temperature which amounts to ± 15-16°K here.

b. *Effects of the short on the cylinder or of accidental shorts to ground elsewhere in the circuit.* One can show formally that these could cause errors, with a magnitude that is uncertain (see Appendix B). There was no evidence of shorting "beyond" the cylinders in the circuit when the furnace was opened.

In addition, it later became evident that the calibration standard, which originated in a digital voltmeter (DVM), varied between DVMs by an amount equivalent to ± 1.5-3°K. However, the capsule temperatures were all made based upon a single DVM during the long duration test.

3.5 Examination of Long Duration Furnace-Tested Samples

3.5.1 Outer Surfaces

On being removed from the furnace, the samples, wrapping foil, frame and ceramic insulators all appeared in excellent condition. All metal parts were very clean, having a silver-like shine. The ceramics were white except for a slight darkening near the top end, and some considerable black-coppery

coloring near the location where the horizontal pieces exited between the top cap and the main furnace body. The former is explained by volatile accumulation at the cooler end of the furnace, the latter by the same mechanism but with greater effect as the thermocouple exit was a channel for volatiles.

Upon removing the foil shields from the samples, their covered surfaces were seen to have the same appearance as the uncovered ones. At a few small ($\sim$1 mm^2) spots on each cylinder, the foil had evidently vacuum-welded itself to the surface. On close inspection, a thin ($\sim$.120 mm) circumferential line of white particles was found on the ASTAR cylinder, located where the bottom edge of the upper Ta shield had been close to or in contact with the cylinder.

Optical inspection of these particles showed a translucent crystalline appearance. An investigation was conducted using the SEM (Scanning Electron Microscope) and associated EDX analysis. The SEM showed thin ($\sim$.2 μm) mica-like layering and that the particles were not continuous with the cylinder surface. In addition, charge build-up difficulties indicated poor electrical conductivity.

The EDX can perform semi-quantitative elemental analysis for atomic number nine and above (this excludes C,N, and O). There was considerable difficulty in applying it here due to overlap of characteristic electron energy emission lines amongst the refractory elements. The apparent detection of some silicon on both the particles and the cylinder surface may be spurious because of overlap problems with a W line. Nonetheless, the silicon could have originated with the diffusion pump oil, particularly during the 12 minute power failure. Other elements -- Al, Mg, K, F -- did seem to be present in the particles by an order of magnitude greater (a few %) than on the cylinder surface. Tantalum was the major constituent of the particles.

Galasso in [41] discusses several crystalline complex oxides which have a layered structure, and it is likely that the particles fall into this category. They were probably formed from the edge of the Ta shield. A few apparently similar particles were seen on the W-25Re cylinder at a similar location. However, they did not show the distinct layering, and EDX analysis was inconclusive; they may have been later contaminants.

3.5.2 General Interior Conditions

The samples were each cut approximately in half using a low-speed saw and Isomet cutting fluid. Saws were conditioned with graphite and consumed about 0.5 mm width. The slow speeds (~20 minutes for ASTAR and 1-1/2 to 3 hours for W-25Re depending on pressure used) resulted generally in < 10 μm relief. Later cuts were made through the cylinder and frozen MgF_2 simultaneously. Acetone and distilled water were used to try to clean out the cutting oil, but it had evidently penetrated the cracks in the frozen MgF_2 during the cutting process. Using a vacuum or ultrasonic wash was the most effective method to remove the oil.

When first cut, the cylinders showed no obvious signs of corrosion. The melted and frozen MgF_2 adhered to the wall, though more tenaciously in the case of the ASTAR than the W-25Re cylinder. On the inner wall of the ASTAR cylinder were scattered frozen droplets of MgF_2, and possibly a uniform thin layer of the fluoride as well. Figure 3.7 shows these droplets seen edge on; the dark spots on the cylinder cross section are from ink applied to reduce glare. No fluoride droplets or layer was evident in the W-25Re cylinder.

15a

Figure 3.7 Fluoride Droplets on Inner Surface of ASTAR Cylinder

The distribution of MgF_2 in each cylinder is of interest. Figure 3.8 shows a series of sketches based on observations made after the initial cuts. Note that the majority of MgF_2 in the W-25Re cylinder appears to be in the upper half. The central hole through the crystal in each cylinder is consistent with what is seen when a fluid that shrinks on freezing crystalizes from the walls inward.

Figure 3.9 shows the frozen melt looking towards the bottom of the ASTAR cylinder. Vertical streaks may have been caused by accumulation of graphite from the cutting process. In Figure 3.10 one can see the edge of the flouride on the wall of the same cylinder; fragments beyond the edge suggest good wetting, or may only result from shrinkage of the melt when freezing.

The fluoride in the W-25Re top half cylinder is shown in Figure 3.11. The frozen state contact angle is close to 90°.

It would have been useful to be able to compare cylinder wall thickness before and after the furnace test. It had been assumed that this could be done by comparing samples tested with the small remaining unused cylinder sections. Unfortunately, it was not realized until after the cylinders were manufactured that the considerable variations in wall thickness along the cylinder lengths made this method unuseable. In retrospect, the manufacturer of the capsules should have been asked to measure and specify wall thickness for specific locations along the tubes.

In view of this error, the conclusions to be presented here on experimental material compatibility results are based upon the weight of evidence from optical examinations, composition analysis, and observations of crystal grain boundaries. However, we briefly digress to consider whether

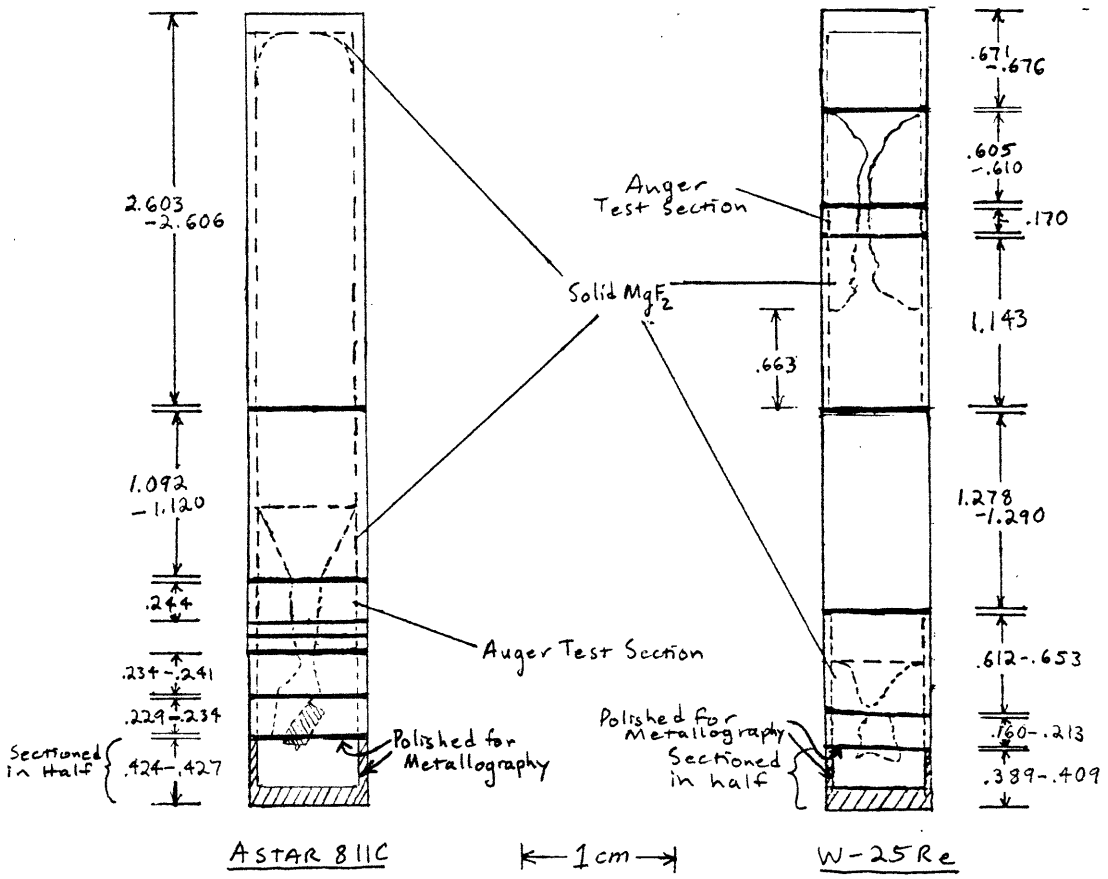

Figure 3.8: MgF_2 Distribution in Test Samples

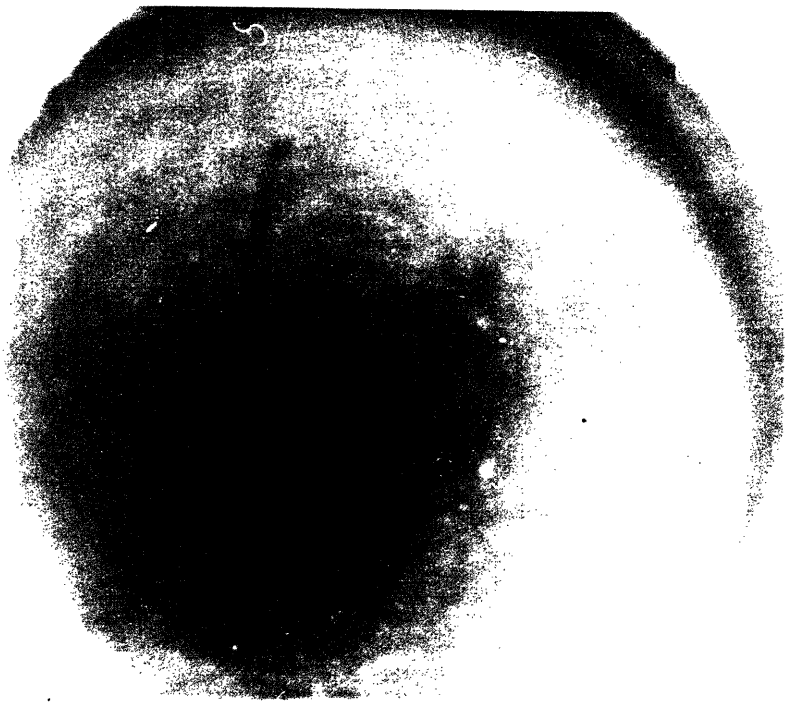

9a

Figure 3.9 Fluoride in Lower Half of ASTAR Cylinder

3d

Figure 3.10 Edge of Fluoride in Lower Half of ASTAR Cylinder

266

Figure 3.11 Fluoride in Upper Half of W-25Re Cylinder

useful conclusions can be drawn from the interesting distribution of MgF_2 in the cylinders.

3.5.2.1 Fluoride Distribution and Surface Wetting

The presence of solidified fluoride in the upper parts of the test cylinders, taken together with the thermocouple data to be discussed in the next chapter, shows that liquid fluoride was suspended in the upper parts of the cylinders at various times. One may ask whether this information provides any useful conclusions concerning the wetting properties of the fluorides on the alloy cylinders. That is, given the height of the suspended column, and the size of the cylinder, can one put a bound on the wetting angle α or surface tension?

At least for conditions of static stability, it appears that the answer is in the negative. Recall that the contact angle for a fluid with a wall is determined by

$$\sigma_{lg}\cos\alpha + \sigma_{ls} = \sigma_{sg}$$

where σ_{lg}, σ_{ls}, and σ_{sg} are the liquid-gas, liquid-solid, and solid-gas surface tensions, identical to Helmholtz surface free energy for pure materials. In zero gravity conditions, this angle α will be identical to the one seen on a macroscopic scale, and either end of a liquid in a tube will form a section of a sphere (Figure 3.12a).

Now if we moved the tube into a gravitational field, and if again the macroscopic angle were determined by surface energy as α, then the droplet would fall unless supported by a pressure difference, $p_2 - p_1$ (Figure 3.12b). But what is actually observed is that the apparent contact angle assumes

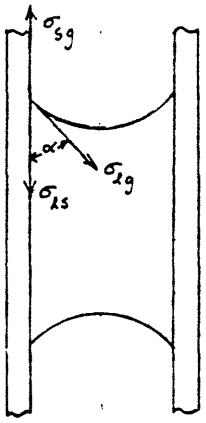

Figure 3.12a Liquid in Tube, zero-g conditions

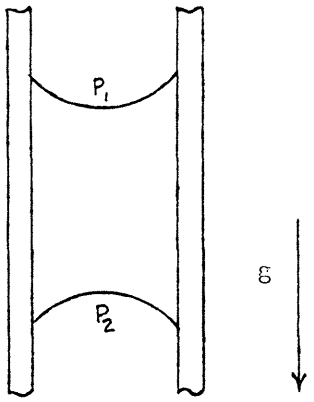

Figure 3.12b Liquid in Tube under gravity(zero surface roughness)

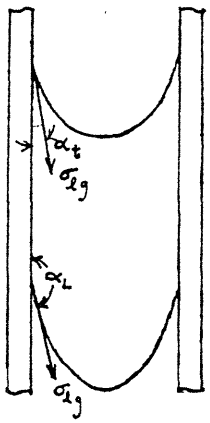

Figure 3.12c Liquid in Tube Under Gravity Observed Behavior

different values at the leading and trailing edges, α_L and α_T, and the upper and lower surfaces distort (Figure 3.12c). If one integrates the surface tension along the upper and lower edges with the apparent contact angles, one finds that it provides a force supporting the liquid in addition to any pressure difference.

Experimentally it has been found that for a given liquid, gravitational field, and tube size there is a limit on how large the leading angle, and how small the trailing angle, can become. Myshkis et al in [42] note that though this phenomenon is not fully understood, there is experimental evidence showing a correlation with surface roughness. The same author states that Deryagin developed a theory to relate the limiting apparent contact angle α_i with the α which must exist at a microscopic scale on the wall, since it is determined solely by surface energies. This states that

$$\cos\alpha_i = k\cos\alpha$$

where k is a measure of surface roughness that goes to unity as perfect smoothness is approached. Under that condition, the apparent contact angle would be limited to the microscopic one, and the droplet in a cylinder would fall absent a supporting pressure difference. Conceptually, surface roughness means that on the microscopic scale the liquid makes contact at locations that allow an upward force at the apparent contact angle.

In the present context, the above discussion implies that to obtain the ideal contact angle α, one need know the value of k and of the limiting apparent angle α_i; or, if one knew the apparent angles at top and bottom for a given column height, one could deduce the value of σ from the force balance (given a known pressure difference). Clearly there is insufficient data here for either of these methods.

However, one can place a lower limit on surface tension σ (or σ_{lg}) using the stability criterion discussed by Satterlee and Reynolds in [43]. This criterion is one of dynamic stability of the meniscus, namely that no small disturbance of the shape will lead to a reduction in total potential energy. The results are correlated by the Bond number

$$B_o = \rho \frac{gR^2}{\sigma}$$

where ρ is liquid density, g the gravitational constant, and R the tube radius. Bond number compares gravitational to surface tension forces.

The stablest case occurs with apparent contact angle $\alpha = 90^\circ$, for which $B_o \leq 3.3$; the least stable are with completely wetting or nonwetting conditions, for which $B_o \leq 0.70$. Using the value of R for the W-25Re cylinder and ρ for MgF_2 liquid, one finds

$\sigma \geq 66$ dyne/cm (90° contact angle)

$\sigma \geq 311$ dyne/cm (completely wetting or nonwetting)

This only sets a broad lower boundary. But it is interesting to note that [25] sets the surface tension of LiF at ~250 dyne/cm. If MgF_2 indeed wets well, then the second bounds above suggest surface tension similar to that of LiF. Working backward, using the stability criterion, this implies B_o of the order one; i.e., gravitational and surface tension forces were of the same order. This result does not affect the validity of the present work for zero-g conditions.

3.5.3 Auger Analysis of Cylinder Cross-sections

Slices were made, using the low speed saw, of the flouride-filled parts of the cylinder as was indicated in Figure 3.8. At this point no sign of corrosion was seen in the W-25Re, but the ASTAR seemed to have a problem at several spots where it appeared that MgF_2 had penetrated the wall. The worst of these wall inclusions, which had penetrated about 3/4 of the wall, was studied using Auger surveys.

3.5.3.1 Principles of Auger Analysis

When a sufficiently high energy electron beam is used to ionize an atom, a core level hole can be created, which may then be filled by an electron from a higher energy level. Energy released by this transition is emitted by the atom as an x-ray photon or "Auger" electron. Detection of the former is the basis of x-ray fluorescence analysis (ESCA) and of the latter of Auger Spectroscopy.

The penetration depth of the Auger technique is 1-2 atomic layers; for this reason, a Ar+ beam is used to sputter-clean the surface. With many hours of careful work on the machine, one can obtain quantitative measures of elements present to an accuracy of about 0.1%. Elements except hydrogen are detectable.

The data are usually presented as a normalized plot of the derivative of the number of Auger electrons detected with respect to kinetic energy versus kinetic energy in electron volts. Conventionally, the spikes (dips) in the plot, since they are sharper than the peaks, are used to identify elements. As example of data is shown in Figure 3.13, which was a scan mode survey of monocrystalline MgF_2 after being sputtered for 3 minutes, which removed some surface carbon. Changes in the intensity of these peaks occur for elements appearing in compounds due to electron cloud modifications in bonding.

Time limitations made it impossible to achieve the potential accuracies stated above. With the scan times used, the detection limit was about 1%. With knowledge of appropriate sensitivity factors for the elements and compounds, quantitative percentages for them could be obtained. These factors

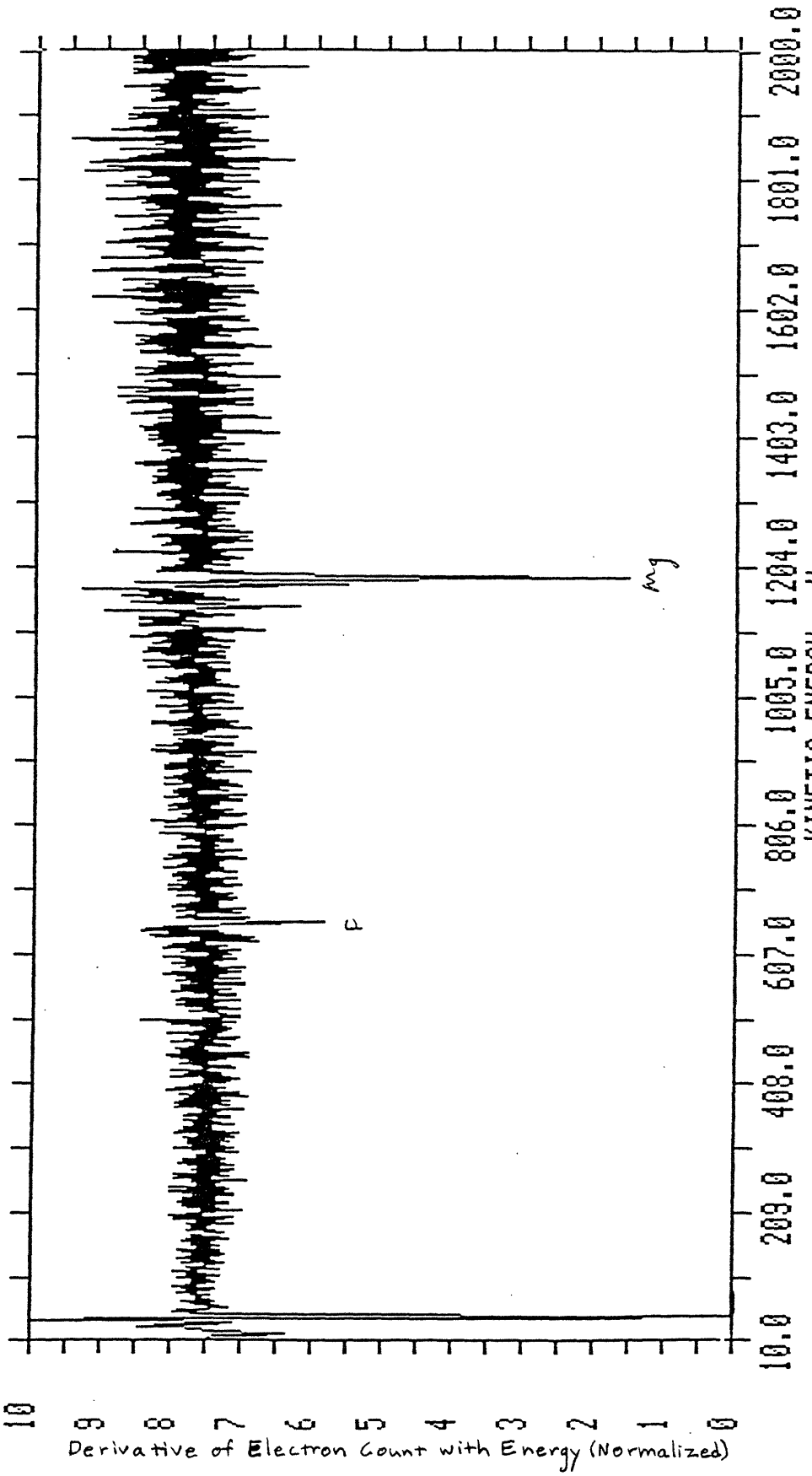

Figure 3.13 Auger Analysis of Monocrystalline MgF_2

are available only for the elements; for compounds they would have to be compiled experimentally from known pure substances.

3.5.3.2 W-25Re Auger Analysis

Figure 3.14 is an SEM micrograph of the W-25Re/MgF_2 interface region. The metal is in the upper part center, the MgF_2 below to the lower right. The mottled dark regions to the left and right are silver paint applied to provide a shorter conduction path for electrons impinging on the non-conductive MgF_2. Streaking is due to charge buildup and the white regions are probably anomalous charging areas of the MgF_2 or the paint. (There was some change in them between photographs. Also, sputtering had been used to reduce charging, and some areas may have been partly shielded from the Ar+ beam.)

The irregular metal surface at the interface is consistent with the finish of the cylinder interior, and was probably revealed because of MgF_2 chipping. Attempts to perform a surface analysis there were impeded by the irregular "valley." At another location difficulty occurred due to carbon particles (probably from the graphite used to condition the saw blade) that had become lodged at the interface. Nonetheless, an analysis was performed on the metal at the latter location within ~50 μm of the interface. The survey (which was preceded by several minutes of sputtering) is shown in Figure 3.15. Tungsten is present in several lines and due to line overlaps is probably "hiding" the Re. The carbon shown is considerably reduced from pre-sputter values, so it probably originated with surface contamination. The sample used was from the top half of the cylinder and may not have contained fluoride for the entire furnace test, though thermocouple data indicate that there was melt separation within the first week of being above the melting point.

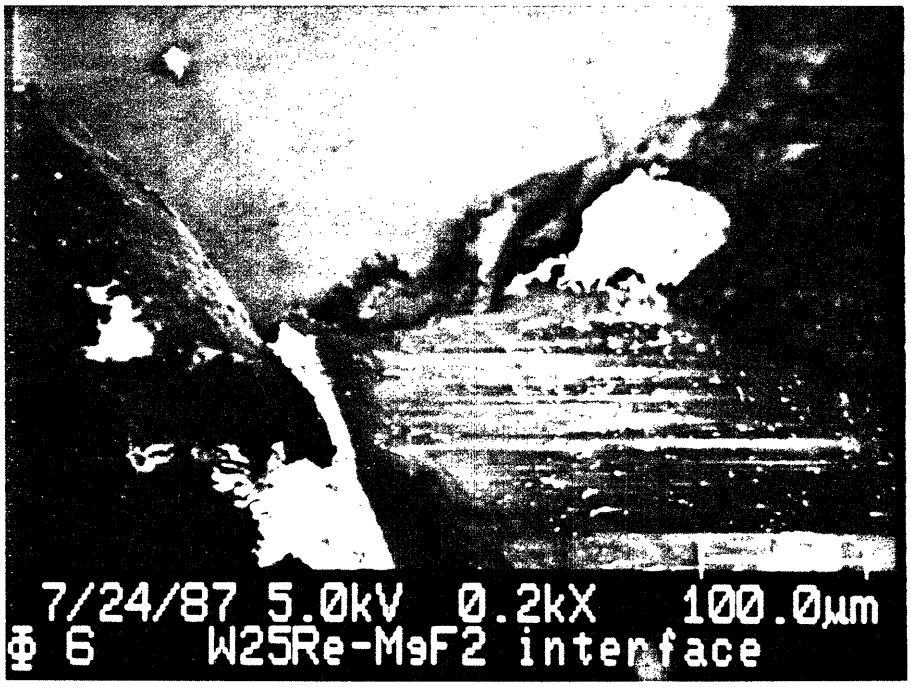

Figure 3.14 W-25Re/MgF_2 Interface Region, Cylinder Cross-Section (200X)

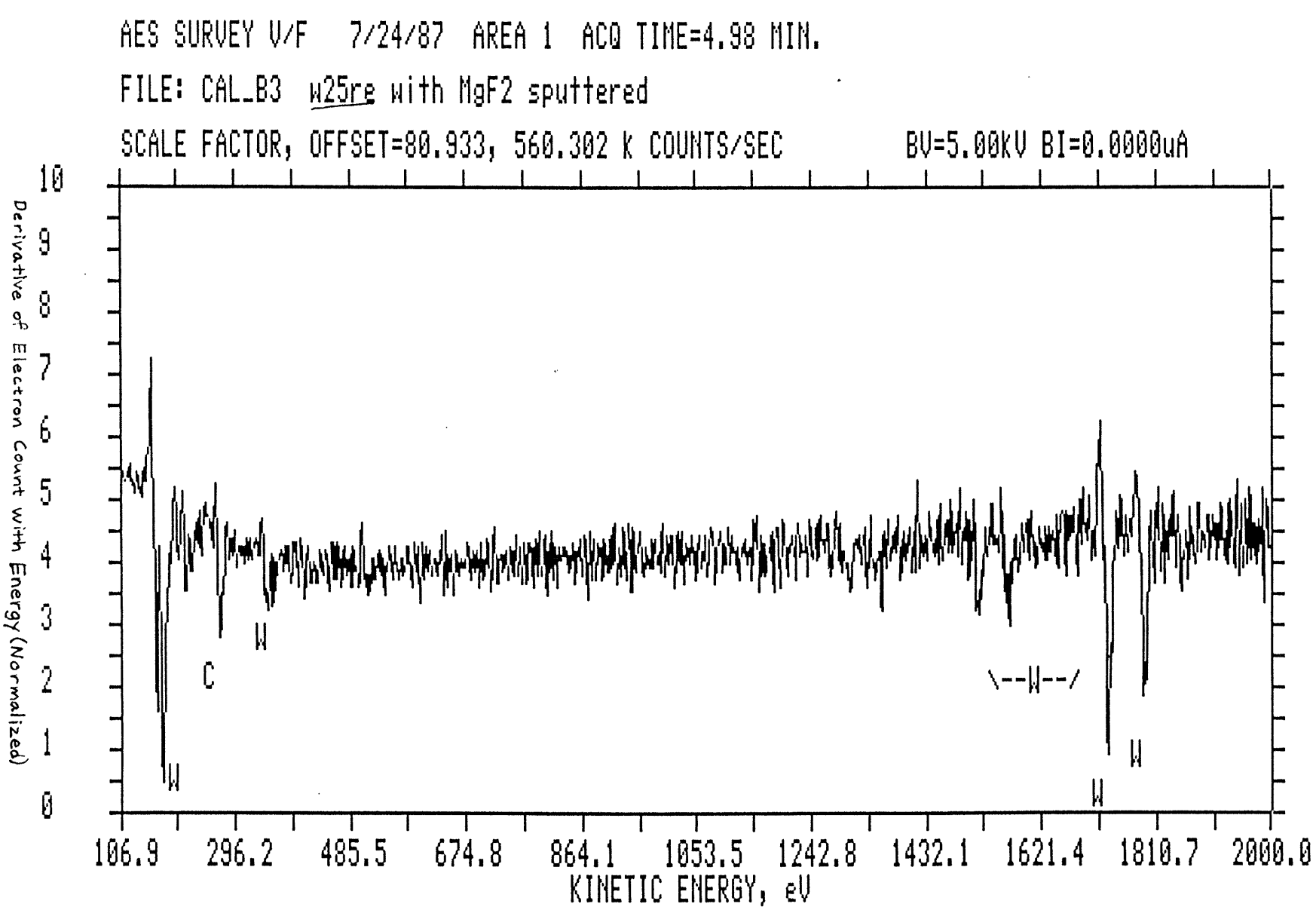

Figure 3.15 Auger Survey of W-25Re Adjacent to MgF_2

3.5.3.3 ASTAR-811C Auger Analysis

Examination of this sample concentrated on a comparison of the wall inclusion noted earlier to a more typical interface zone.

The former area is shown in the SEM micrograph, Figure 3.16. At the top center is the MgF_2, below it the inclusion zone, and then the apparently unaffected metal. The edge wall of the cross-section falls off to the lower left. Note that the MgF_2 is present in "veins" in the inclusion.

Auger surveys of points in the unaffected metal and the inclusion zone are shown in Figures 3.17a and 3.17b respectively. In both oxygen is present and probably results mainly from surface adsorption. The crucial difference is the presence of iron in the inclusion zone. Indeed, there are several possible Fe-Ta phases as shown in the phase diagram presented by Kubaschewski ([44], p. 144), and reproduced by Moffat [45]; see Figure 3.18. None of these displays a melting point at or below the operating temperature of the furnace test, so solid state diffusion must have been the mechanism of the inclusion growth, unless the presence of W and the minor constituents resulted in a major change in behavior.

In Figure 3.19a, a closer view of a region at the inclusion/unaffected metal boundary is shown. It is about halfway to the right and halfway down from the center of the last photograph. A survey showed the large black object in top center to be carbon. The data mapped in Figures 3.19b and 3.19c result from scanning for particular elemental lines over the same area. The presence of Fe within the inclusion and its absence outside are clearly shown. At the same time tantalum is fairly uniform, with perhaps a small depletion

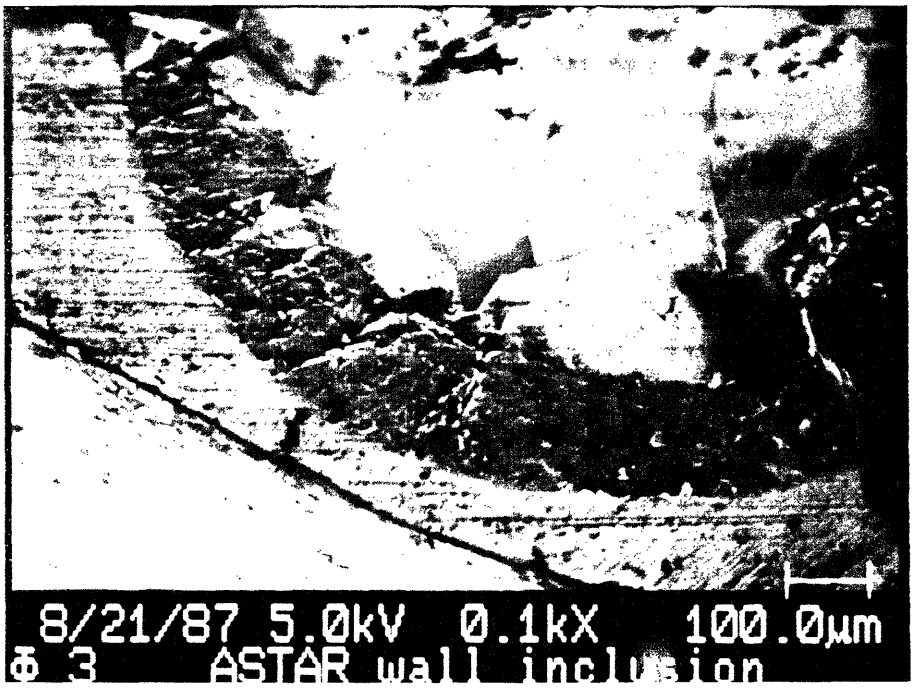

Figure 3.16 ASTAR Sample, Wall Inclusion (100X)

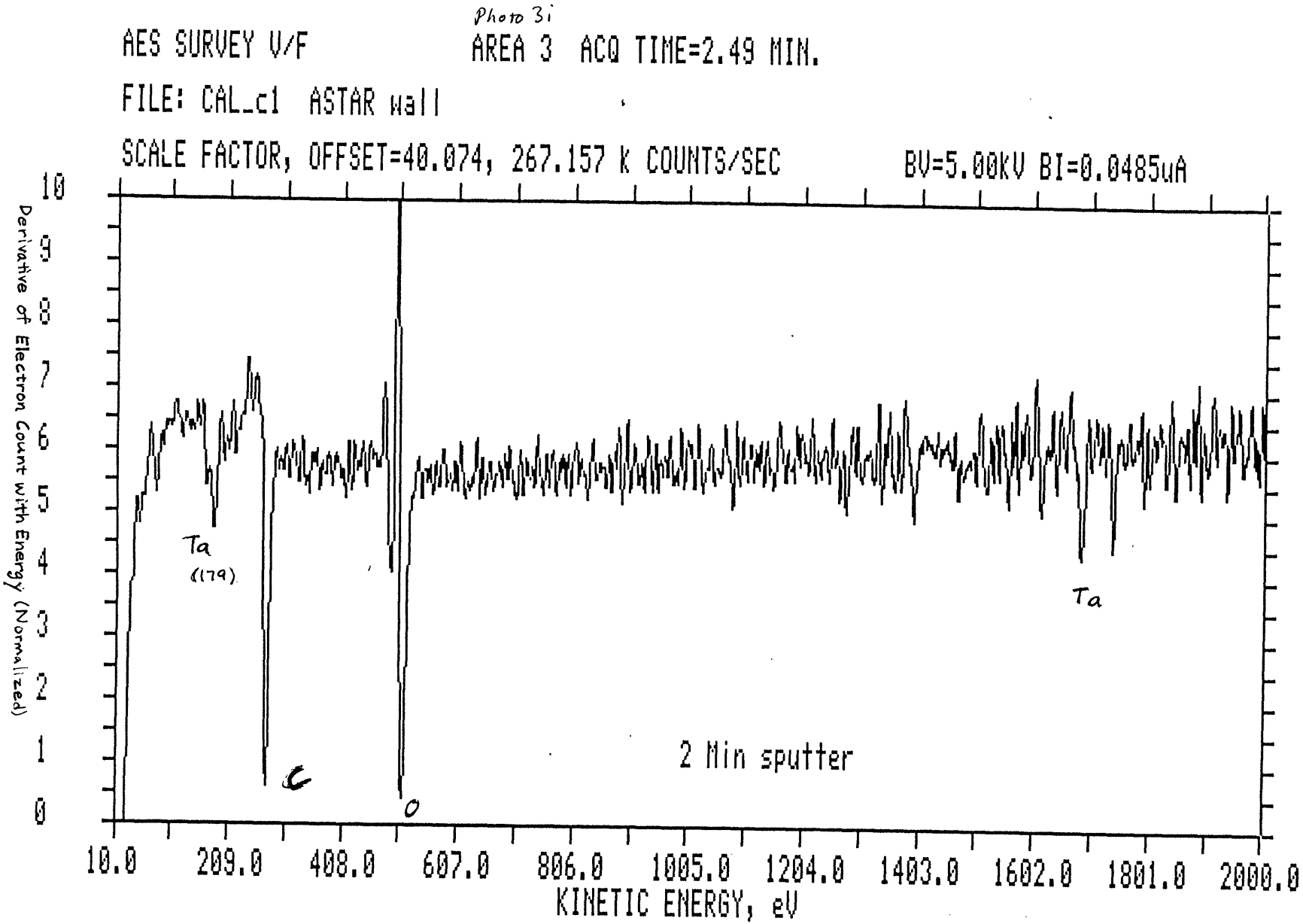

Figure 3.17a Auger Survey "Unaffected" ASTAR Wall Adjacent to Inclusion Zone

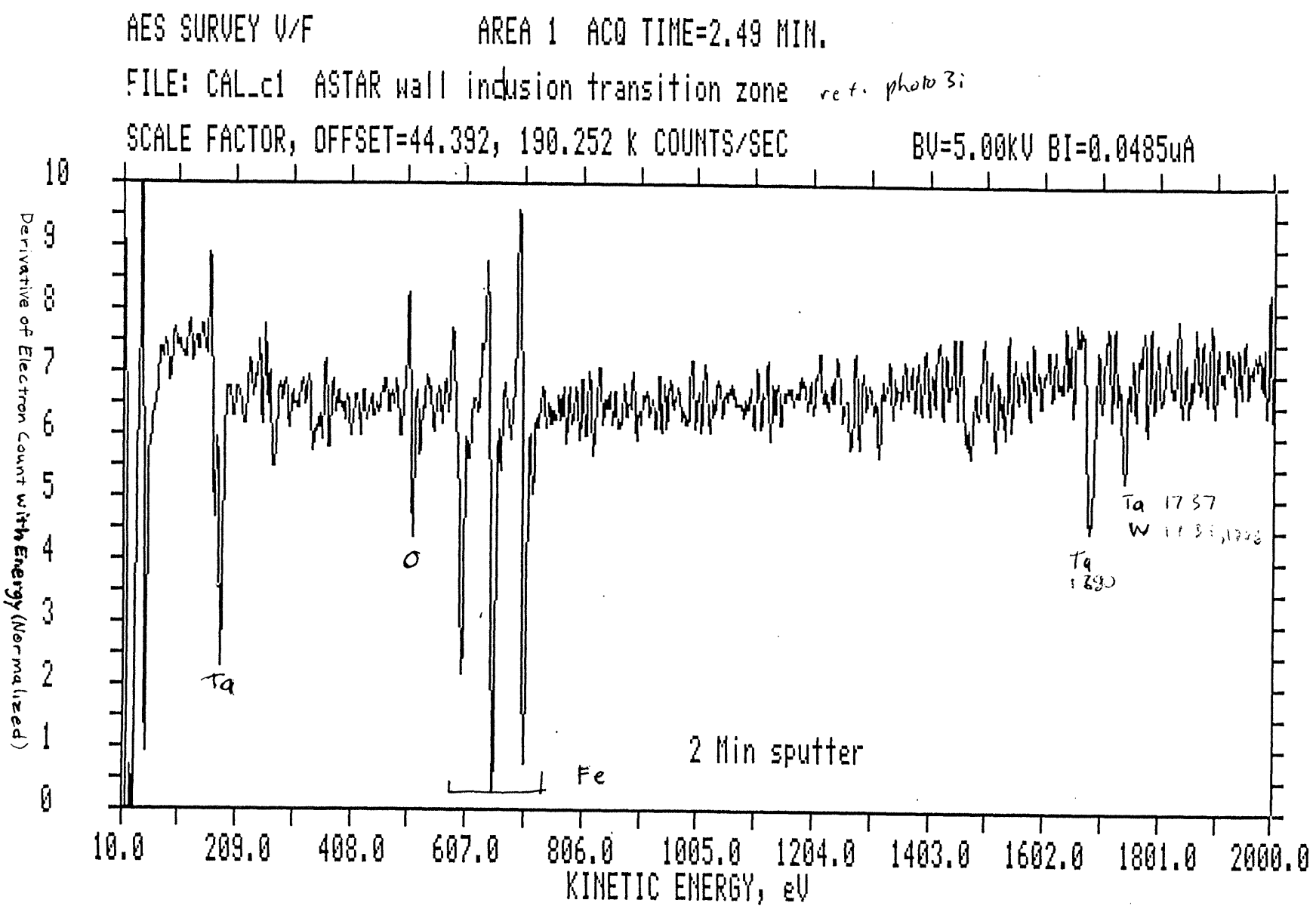

Figure 3.17b Auger Survey of Inclusion zone

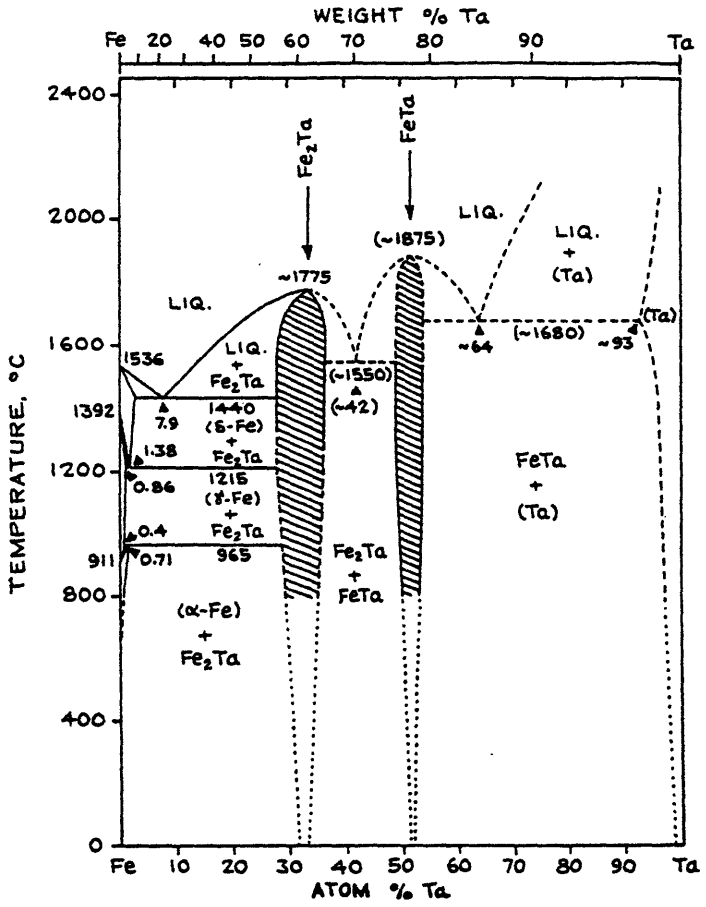

[1]Diagram redrawn from ref. , which reviews literature through 1981. Maximum solid solubility of Ta in δ-Fe is 2.8 at.%. At 1300°C, the homogeneity range of Fe_2Ta is 28 - 36 at.% Ta and that of FeTa, 49 - 54 at.% Ta. Temperatures and composition shown in parentheses, above, are not stated, but values scaled from diagram of ref.

Figure 3.18 Fe-Ta Phase Diagram

11/83

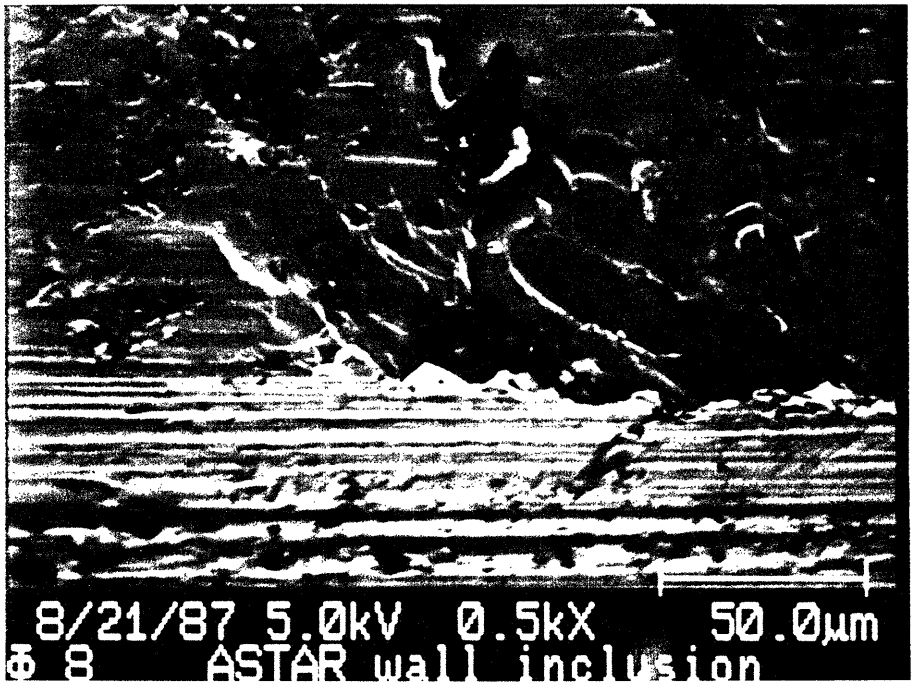

Figure3.19a: ASTAR Sample, Detail of Wall Inclusion at Transition Boundary (500X)

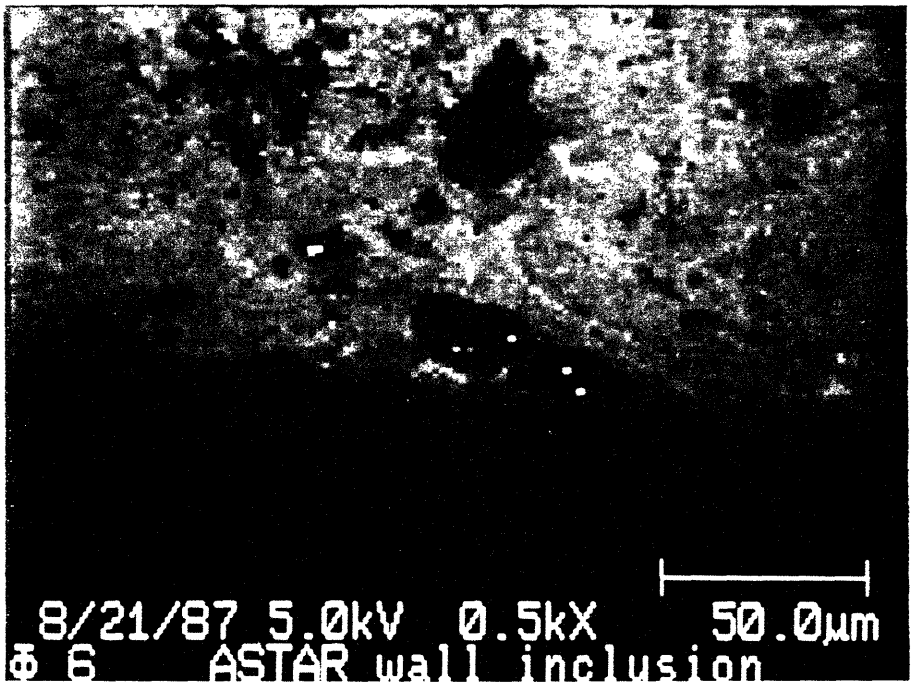

Figure 3.19b Iron Survey Map (Same Frame as 19a), ASTAR Wall Inclusion (500X)

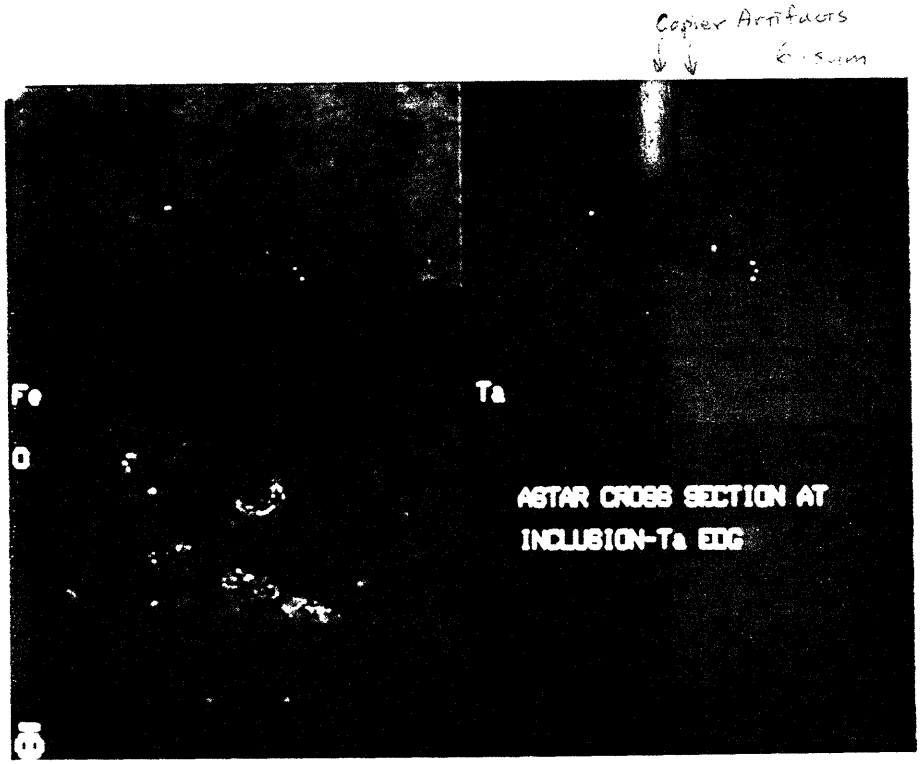

Figure 3.19c Elemental Survey Maps (Same Frame as 19a), ASTAR Wall Inclusion

within the inclusion. Oxygen shows a similar pattern with bright points on the carbon fragments that probably are oxides. (There was some indication of low electrical conductivity there.)

Consider now another region of the ASTAR-MgF_2 disc where there was no inclusion or other obvious sign of corrosion (Figure 3.20a). The rectangular region's surface conduction effect resulted from close-up scanning such as that in Figure 3.20b. (Note that both of these SEM micrographs are at a 60° angle to the surface which was chosen to try to mitigate MgF_2 charging problems.)

Surveys were made at three points: one on the metal peninsula near the center, one just adjacent in the dark area, and one near the bottom of the frame. The first showed only tantalum and carbon, the second carbon, oxygen, and aluminum, and the third magnesium and fluorine.

3.5.3.4 Conclusions from Auger Analysis

The Auger test provided tentative confirmation of the visual inspection results showing no general corrosion. The salient result of the present analysis has been a diagnosis of the local corrosion zones of the type shown in Figure 3.16 that were seen in the ASTAR sample. Iron fragments could easily have become embedded in the ASTAR wall as a result of the drilling process. As noted before, there would have been diffusion of the iron into the wall while the sample was in the heated furnace. DeVan of ORNL believes that brittle intermetallic compounds were then formed which could break off into the fluoride, particularly during melting/freezing cycles. The embedded iron could be simultaneously going into solution in both the fluoride and the wall.

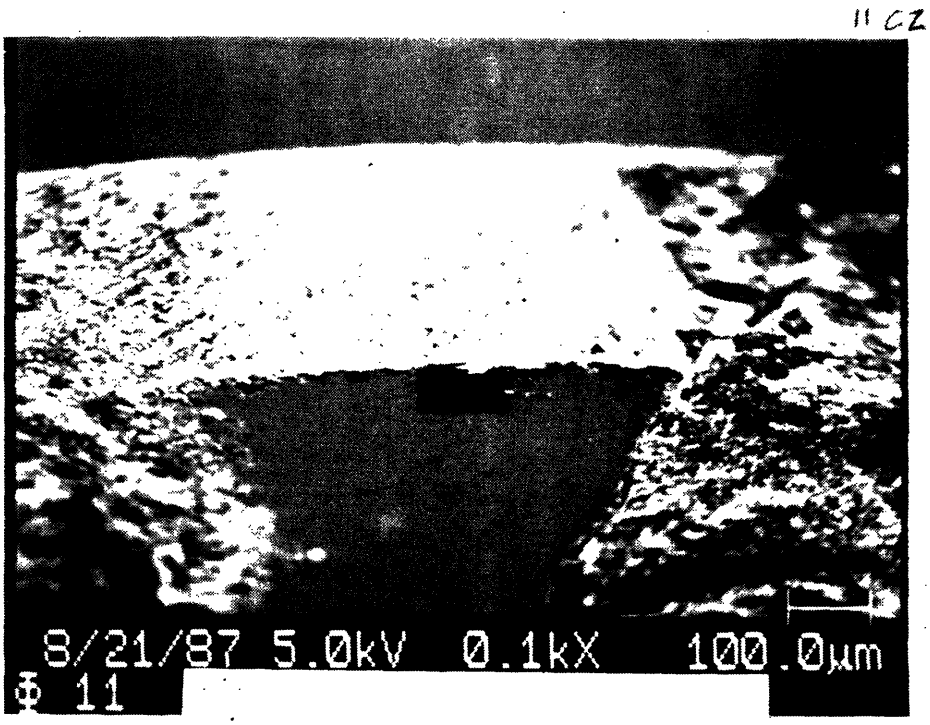

Figure 20a Region of ASTAR Sample Without Wall Inclusion (100x)

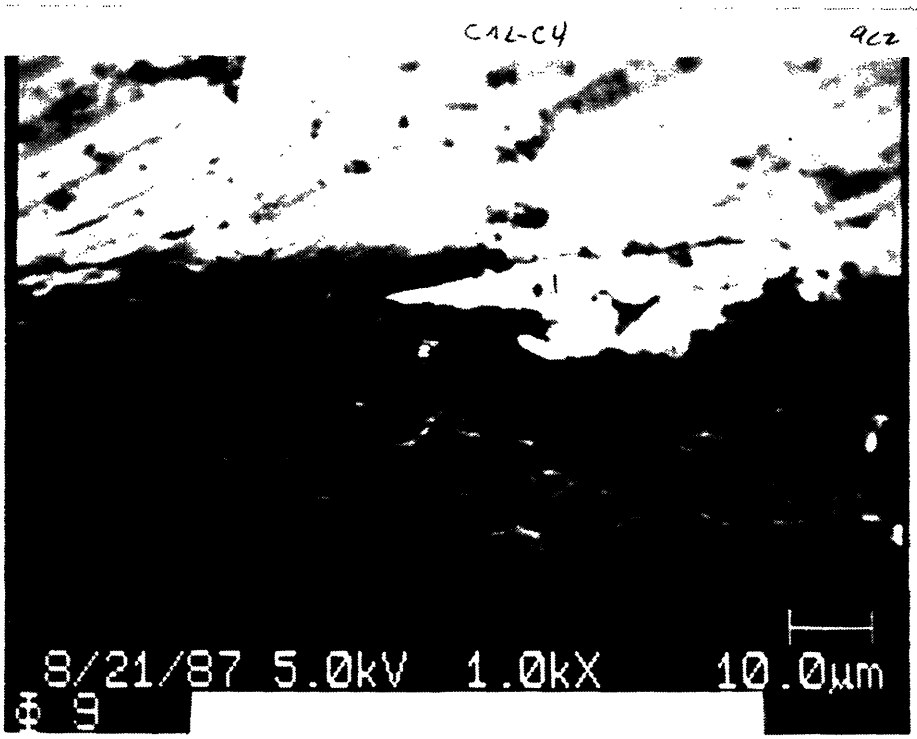

Figure 20b Close-up of Rectangle in Fig 20a (1000x)

Clearly, it would be desirable to exercise care to avoid contamination with iron of tantalum alloys to be used for liquid MgF_2 containment. Such precautions are made more difficult by the relatively soft condition of tantalum at room temperature.

As to the aluminum contamination, again it could have resulted from the manufacturing process, say as leftover fragments from other alloys processed with the same equipment; or it may have originated in assembly of the capsules. In any case there were no obvious deleterious effects.

3.5.4 Metallographic Examination

In order to carry out further investigations of the effect of MgF_2 on the refractory alloys, samples from the cylinder cross-sections were polished, etched, and examined under magnification after being set in an acrylic mounting. To improve edge retention, Coors SC alumina (~.2 mm diameter) powder was added to the acrylic mix. The following were used as etchants on recommendation of a metallographer at ORNL.

ASTAR 811C:	W-25Re:
50 ml Glycerol	50 ml Ammonium Hydroxide
30 ml Lactic acid	50 ml Hydrogen Peroxide
20 ml Nitric acid	
20 ml Hydroflouride acid	

3.5.4.1 ASTAR-811C Alloy

Figure 3.21a shows a 500× magnification of the cylinder inner wall cross-section for a sample not tested in the vacuum furnace. The long linear markings are scratches from a 6 μm diamond grit polish. Grain boundaries are distinguished; further polishing (3 μm) and a re-etch did not determine whether the spots at the boundaries represent another phase.

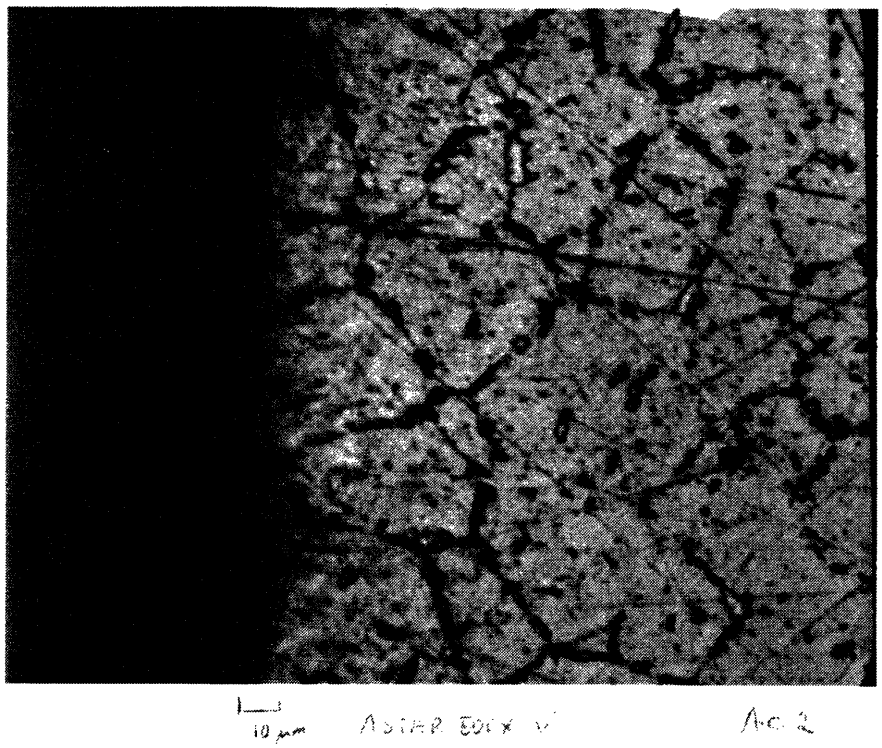

Figure 3.21a ASTAR Cylinder Wall Cross Section, Before Furnace Test (Inner Wall; Cut Across Long Axis) 500x, etched,

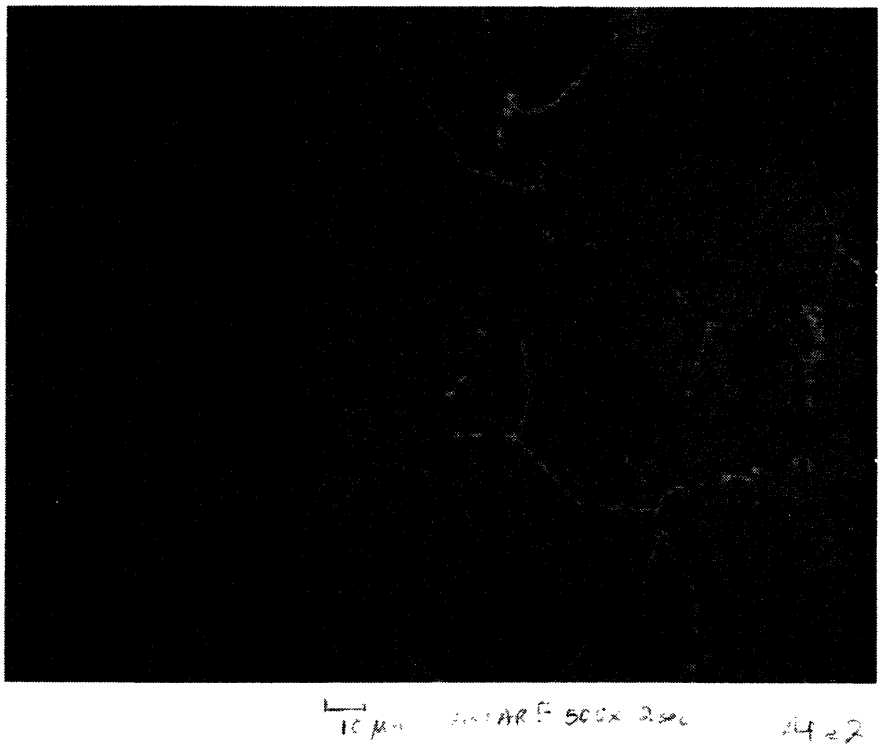

Figure 3.21b ASTAR Cylinder Wall Cross-Section, After Furnace Test (Inner Wall, Cut Along Long Axis) 500x, etched

By comparison, we see in Figure 3.21b no indication of such a phase in the furnace tested sample, or of any penetration or damage at the grain boundary that was in contact with the MgF_2. This photograph was from a wall cut made along the longitudinal axis of the cylinder. The grains appear larger than those in the previous figure, but there was considerable variation and in other areas they were of about the same size as those in the unheated sample. Figure 3.21c shows the grain distribution through a circular cut of the furnace sample, before the etchant had been applied.

3.5.4.2 W-25Re Alloy

The extrusion process by which the tungsten alloy cylinder was manufactured left clear evidence in the wall structure. In Figure 3.22a one sees an etched cylinder cross-section showing distorted grains and perhaps an intergranular phase. Figure 3.22b is from another location on the same cross-section, showing an example of a wall defect. There are some ellipsoid depressions here, which are probably due to localized overetching. It was difficult to prevent excess etchant from seeping up between the metal and the acrylic mount. Ultrasonic cleaning was found to be most effective at preventing this.

When the furnace tested sample was polished, scattered spots of lighter color were seen on the cylinder cross-sectional cut; the longitudinal cut showed similar spots, but these were mainly aligned with the cylinder long axis.

The cross-sectional cut was etched in stages. After the first, depressions were seen in a pattern resembling that of the spots seen before. After two more applications of the etchant, grain boundaries also became visible (Figure 3.23). These show no indication of deterioration at the wall adjacent to the fluoride, but clearly there has been recrystallization. The apparent second phase can be identified with the σ phase in the W-Re phase

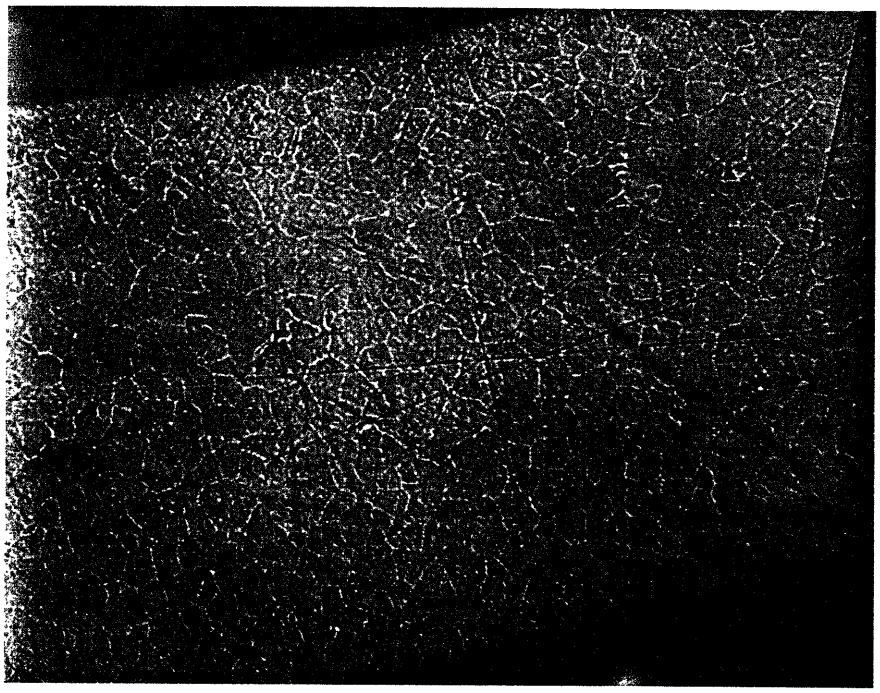

Figure 3.21c ASTAR Cylinder Wall Cross Section, After Furnace Test (Cut Across Long Axis) 500× no etch, 6μm diamond polish

Figure 3.22a W-25Re Cylinder Wall Cross-Section, Before Furnace Test (Inner wall, Cut Across's Long Axis) 500x, etched

Figure 3.22b, Defect in W-25Re Cylinder Wall Cross-Section, Before Furnace Test (Inner Wall, Cut Across Long Axis) 500x, etched

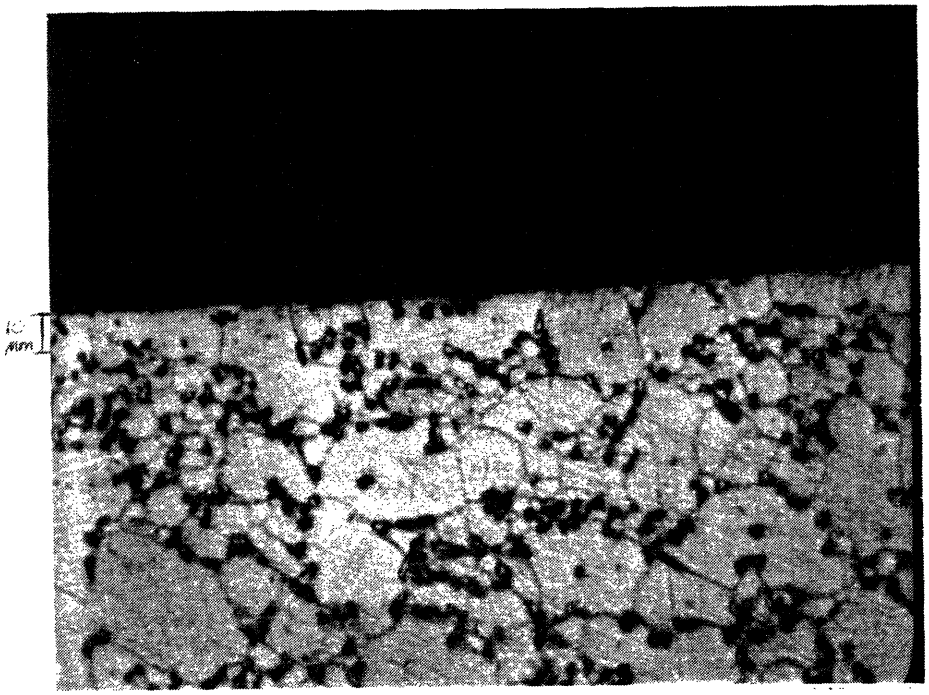

Figure 3.23 W-25 Re Cylinder Wall Cross-Section, After Furnace Test (Inner Wall, Cut Across Long Axis) 500x, etched

diagram (Figure 3.24). At 25 wt. % Re alloy this phase begins to appear at just about the melting point of MgF_2, if we extrapolate the data to that relatively "low" temperature. More appears as Re solubility drops with temperature.

3.5.5 Microprobe Analysis

With the availability of polished samples from the metallographic work, it became possible to perform a quantitative elemental analysis of the frozen MgF_2 using the electron microprobe (full name: Wavelength Dispersive Analysis using an Electron Microprobe X-ray Analyzer). A small amount of additional polishing using 0.25μm alumina was required; this was followed by deposition of a carbon layer to provide a conduction path. Several days were needed to outgas the mountings.

The bulk MgF_2 in both samples showed no residue of the respective metal alloy elements to the detection limits of the system for a 200 sec probe (Table 3.2). The limit of detection was about 250 ppm (weight percent basis). Indirect means showed also that Fe was absent to about this level. This accuracy was not required for the bulk constituents (Mg and F) so a shorter scan was used for them. Relative accuracy refers to both atomic and weight percents; e.g., the abundance of Mg in Table 3.2 is 33.24 atomic percent ± 0.6 % of the same quantity.

Despite these data, another result has caused concern. Figure 3.25 is an electron micrograph of particles that appeared in the MgF_2 of the ASTAR sample. These were of much greater density than the surrounding fluoride, which made them difficult to image sharply. They were mainly concentrated

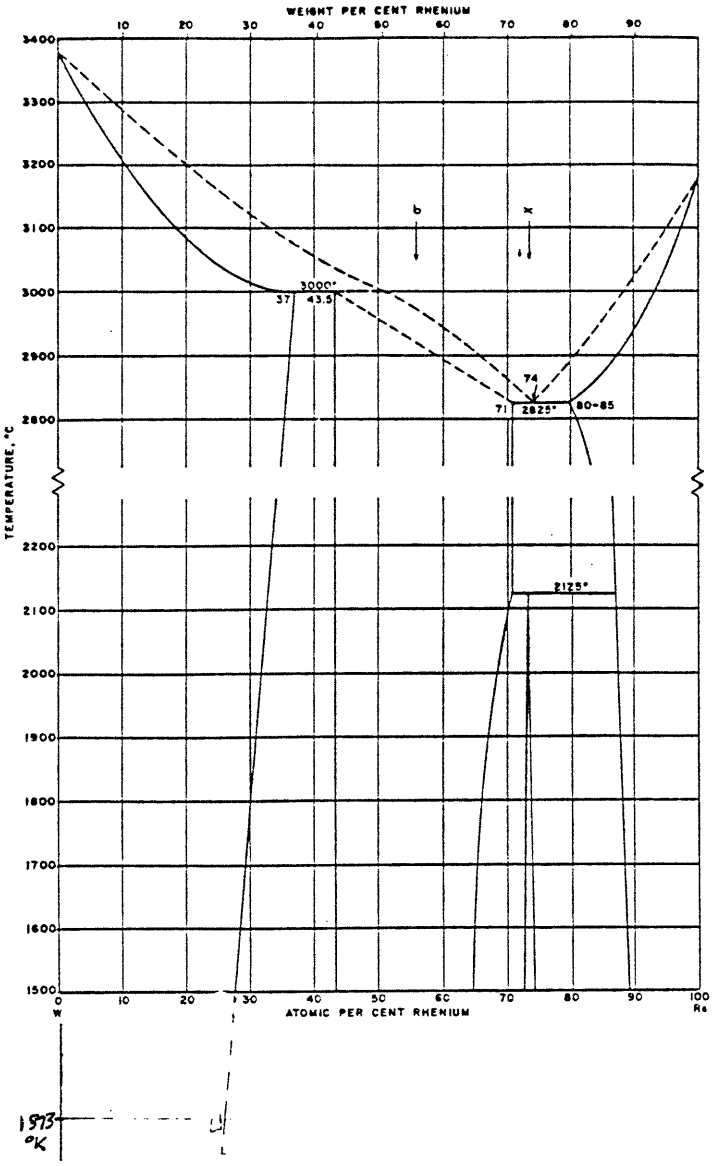

Figure 3.24 Tungsten-Rhenium Phase Diagram [50]

Table 3.2a

Abundances of Elements in ASTAR Sample Bulk MgF_2

Element	Atomic %	Weight %	Relative Accuracy %	Detection Limit (weight %)
Mg	33.24	38.50	± 0.6	••
F	66.76	61.20	± 0.4	••
Ta	undetectable	undetectable	••	0.0223
W	"	"	••	0.0236
Re	"	"	••	0.0292
Hf	"	"	••	0.0211

Table 3.2b

Abundances of Elements in W-25Re Sample Bulk MgF_2

Element	Atomic %	Weight %	Relative Accuracy %	Detection Limit (weight %)
Mg	33.24	38.23	± 0.6	••
F	66.75	60.78	± 0.4	••
W	undetectable	undetectable	••	0.0236
Re	"	"	••	0.0292

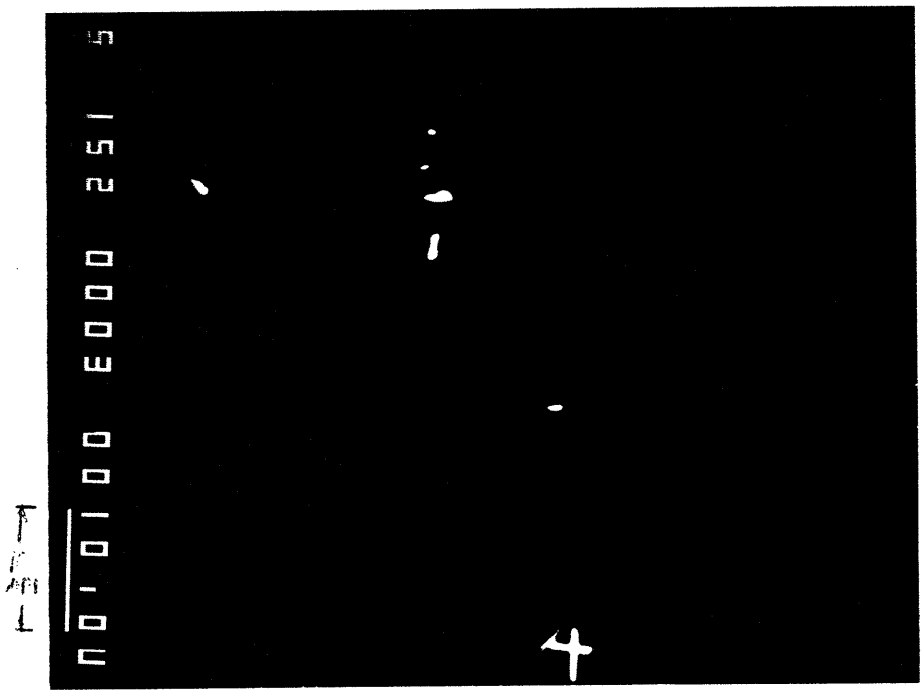

Figure 3.25 Particles in MgF_2 of ASTAR Sample (Polished MgF_2)

along grain boundaries in the fluoride. Microprobe analyses were performed, the results of one of which are in Table 3.3. The device operator believed that the percentages of Mg and F could only be taken as upper limits for the particle, due to possible scattering from the adjacent MgF_2 (because of the small size of the particle). There was no sign of the presence of any of the refractory metals or Fe except for Hf.

What does the value of ~72 wt % (± 5% relative) Hf say about the particle composition? Clearly some other element (or elements) is present. Some possible species are: HfF_4 (70.2 wt % Hf), HfO_2 (84.8 wt % Hf), HfC (93.7 wt % Hf), and HfC_2 (88.1 wt % Hf). The first comes closest to the Hf wt % measured, but we should be seeing more F. There is also the question of whether HfF_4 is a gas phase when at the MgF_2 melting point (see note, Table 2.4). Then whatever HfF_4 is present might be precipitated through the fluoride at room temperature as a result of the gas in solution at the higher temperature.

Oxygen content would have been difficult to find quantitatively using the present method. Oxygen might have originated in water contaminating the flouride. Carbon could be present but the carbon layer applied would have made a reading useless.

That the particles include Hf as their only refractory constituent is consistent with the data in Chapter 2 (Tables 2.4, 2.5) showing Hf to be the most reactive of the refractories with oxygen and fluoride. Recall also from that chapter that Hf is intentionally added to ASTAR as an agent that will increase hardness by reacting to form HfO_2.

Table 3.3

Abundances of Elements in Particles in MgF_2 of ASTAR Sample

Element	Atomic %	Weight %	Relative Accuracy
Mg*	(10.86)	(2.46)	± 5.0%
F*	(46.57)	(8.36)	"
Hf	42.57	71.55	"
Ta	undetectable	undetectable	••
W	"	"	••
Re	"	"	••

* *Percentages distorted by scattering from bulk MgF_2*

In the end, one wants to know whether the appearance of the particles will cause a debilitating effect on the metal over the projected lifetime of the power system. Clearly, the Hf has been coming out of solution in the metal and entering the fluoride, where it reacts to form another species. A very rough estimate may be made of the depth of metal affected by this process. Figure 3.25 shows an atypical region (cluster) of particles, perhaps representative of 10% of the fluoride surface. Idealizing the particles as spheres of diameter 1μm the number visible (10) are those that were within one diameter, in the normal direction, of the cut plane. One obtains a particle density of $1.27 \times 10^{-3}/\mu m^3$ fluoride. The volume of fluoride in the cylinder comes to $5.29 \times 10^{11} \mu m^3$; thus there are $\sim 6.72 \times 10^7$ particles present. If their density is close to that of HfO_2 ($9.68\ g/cm^3$ from [46], p. 192) the mass of Hf present is $\sim 6.51 \times 10^{-7}$ kg. Then the depth (d) of the wall depleted of Hf (assuming for a moment total depletion there and none beyond) is given by

$$d \approx \frac{6.51 \times 10^{-7} kg}{2\pi r_c h_c (.01) \rho_{Hf}}$$

where r_c and h_c represent the radius and height of the cylinder (the factor (.01) is included by the assumption that the volume fraction of the Hf in the alloy is close to its mass fraction). With the Hf density $\rho_{Hf} = 13310\ kg/m^3$, $r_c = 6.35 \times 10^{-3} m$, $h_c = 1.90 \times 10^{-2} m$ (height of liquid in partially filled cylinder), the result is $d \approx 6.5\ \mu m$.

A naïve extrapolation for 10 year's time gives 273 μm or about half the wall thickness. Clearly the actual affected region would include the entire wall. Presumably, wall properties would change, and the wall might actually shrink. So it will be critical to determine exactly what the particles are, what caused their formation and whether their appearance is preventable. If their formation is not preventable, one would require a determination of the effect of Hf depletion on the metal properties.

CHAPTER IV

ANALYSIS OF THERMOCOUPLE DATA

4.1 Introduction

It was noted in the previous chapter that temperature data for the test capsules were gathered during the long duration metallurgical tests. Unfortunately, due to the wire tying the thermocouples to the cylinders, this data was distorted. To clarify the data, a second, short duration furnace run was performed with a second set of cylinders and with thermocouples on each that were not tied together. This chapter discusses the evidence gathered in both test runs.

4.2 Long Duration Test Thermocouple Data

Despite the uncertainties in the thermocouple readings discussed earlier, it was possible to distinguish when the fluoride in the test capsules was undergoing a phase transformation. For example, the freezing of the fluoride is shown for the W-25Re capsule in Figure 4.1. The power setting on the furnace was turned down from a level of 68A to 50A. Temperature on the cylinder initially follows a smooth decay. After a drop of the order of 100°K, it suddenly increases by about 10°K, decays again, increases again by about 30°K, then finally decays along a curve that eventually appears to be a continuation of the initial decay. A similar behavior is shown for the ASTAR cylinder temperature in Figure 4.2, but here only one "hump," with a temperature jump of ~40°K occurs.

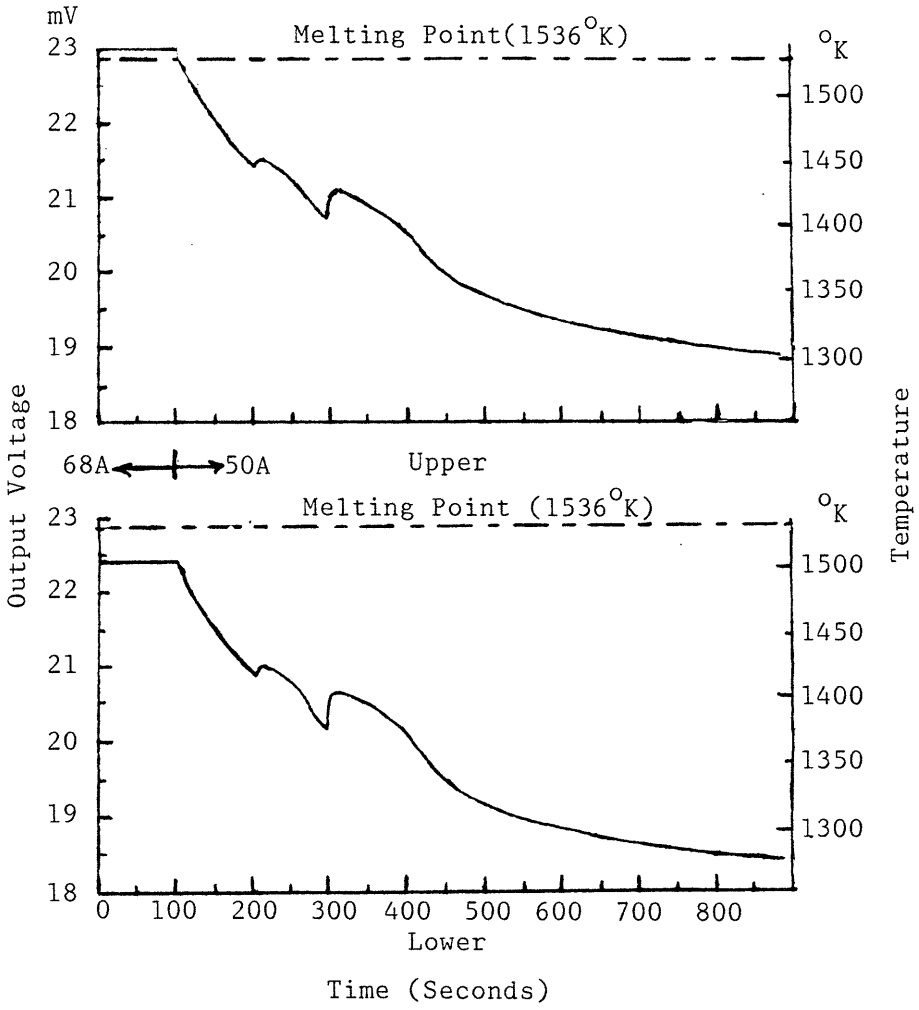

Figure 4.1 Freezing Curves, Long Duration Test
W-25 Re Cylinder (3/27/87)

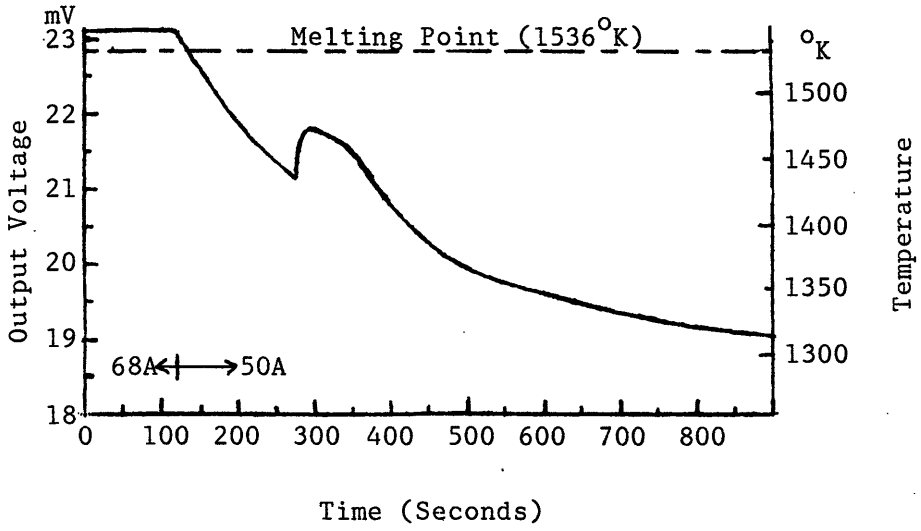

Figure 4.2 Freezing Curves, Long Duration Test, ASTAR Cylinder (Lower thermocouple only,3/2/87)

What each of these jumps represents is heat being released as distinct fluid volumes suddenly start to crystallize into the solid state, starting from a metastable condition below the melting point. Such crystallization may take place either by formation of nucleating particles in the liquid (homogeneous nucleation) or by growth from "foreign" nucleation sites such as impurities or wall surfaces [47]. In either case, energy must be used to form the solid surface (form the interface between solid and liquid) and this is provided by free energy released by the phase transition.

Under the classical theory of Gibbs, there is a critical radius that a homogeneously nucleating particle must achieve to continue growth:

$$r_k = \frac{2\sigma}{\eta h_{ls}}$$

where σ is surface tension, h_{ls} the heat of fusion per unit volume, and η the relative supercooling defined as

$$\eta = \frac{T_m - T}{T_m}$$

with T_m the melting point. If the particle size is larger than r_k, free energy will be minimized by continued growth. As the degree of supercooling increases, the size of particles required for nucleation decreases. Eventually the size is sufficiently low that aggregates of molecules (which are always forming and dissolving in the liquid and whose number increases with supercooling) grow indefinitely.

However, the fluoride distribution in the cylinders here, showing a shrinkage tube down the middle, indicates that it is most likely that crystallization began at the wall and grew inward. Nucleation on a "foreign" surface is referred to as heterogeneous. Current theories state that a

material whose solid phase has close affinity for the solid surface should crystallize with little or no supercooling. (A later section will consider what might be done to reduce supercooling for MgF_2.)

The degree of supercooling for MgF_2 is difficult to state based on these data alone, due to the thermocouple uncertainties. Generally, the ASTAR exhibited a greater delay in crystallizing after the furnace power was turned down. The number of "humps" (crystallizations) when the capsules were cooled varied. Sometimes there were as many as three for a particular capsule. This could change between freezing tests done within a short period of each other (< 1 hr.). Some of these changes seem to have been caused by random variations in the time that crystallization was triggered (humps overlap or separate on the temperature outputs) while others apparently represent real changes in the distribution of MgF_2 in the cylinder (humps change in size or number).

The last freezing recorded was similar to those shown in Figures 4.1 and 4.2, which indicate one large volume of MgF_2 in the ASTAR and two smaller ones in the W-25Re. This correlates with the distributions seen after capsules were cut open (Figure 3.8) even though the fluoride was melted again for a short period (< 2 hrs.) before the final freezing to check some other temperature data.

Melting of the fluoride presented less dramatic, but nonetheless distinct, evidence, as is shown in Figures 4.3 and 4.4 for the W-25Re and ASTAR capsules respectively. These were obtained when the power level was turned up from 65A to 70A. The lowered slopes of the curves represent a temperature deficit that shows heat being absorbed for the phase change. This

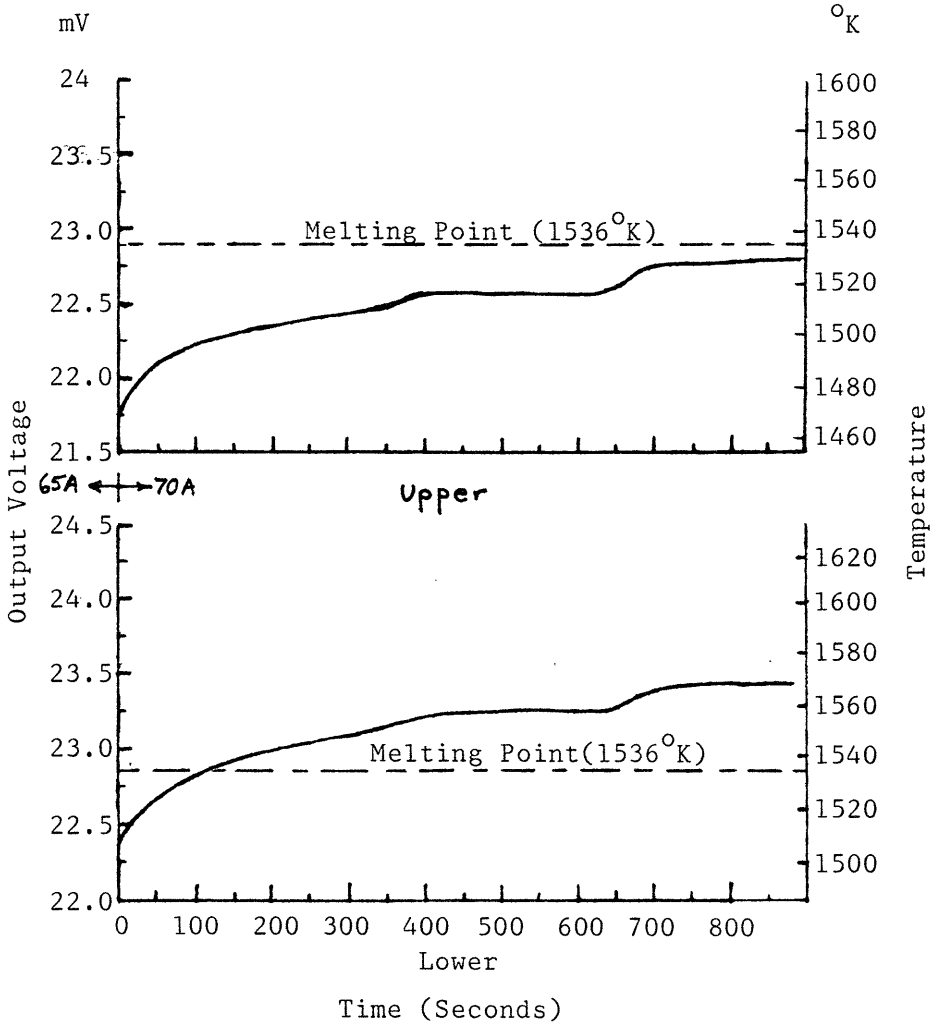

Figure 4.3 Melting Curves, Long Duration Test
W-25Re Cylinder (3/27/87)

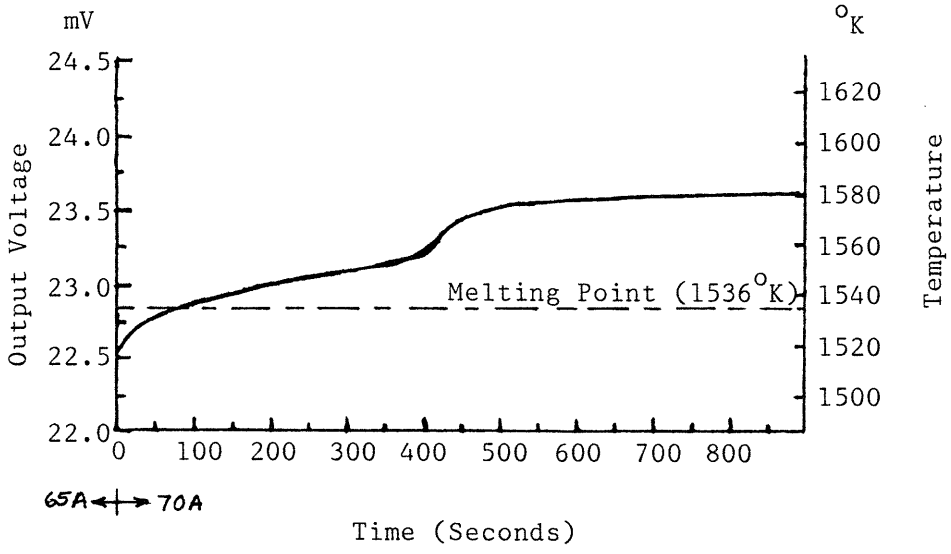

Figure 4.4 Melting Curve, Long Duration Test, ASTAR Cylinder (Lower thermocouple only, 3/28/87)

is perhaps seen more clearly in Figure 4.5. Figure 4.5a shows a series of heating steps as they affected the ASTAR thermocouple measurement. The steps before and after the phase change follow simple exponentials. If the time constant is interpolated, one can draw a curve for temperature absent the phase change, as shown in Figure 4.5b, along with the actual data.

A single compound undergoing melting would be expected to be isothermal during the phase change. One explanation for the slope exhibited by the data in Figure 4.5b is a thermal gradient radially in the cylinder if the fluoride melts only from the outside toward the center. Such a gradient would allow one to calculate a thermal conductivity of the molten fluoride. But it seems unlikely that the solid would not also melt at the bottom and sink.

The thermocouple was shorted near the tube center, so (referring to the fluoride distribution in Figure 3.8) it was less likely to be adjacent to the melt than if it had not been shorted. As the furnace heated up during fluoride melting, the temperature measured increased since the tube wall was not a perfect conductor to the melting, isothermal fluoride. Once the melting was completed, the tube temperature measured increased, with steeper slope, toward that of the furnace (as occurred at about 400 sec in Figure 4.3). Say this were followed by a second melting, of another mass of fluoride (as apparently occurred in Figure 4.3 from 400-600 sec and Figure 4.5b from 300-500 sec). The furnace would be by this time more nearly at equilibrium temperature for the particular power setting. So the thermocouple temperature would be more and more nearly isothermal, somewhere between the temperature of the melt and that of the furnace. Finally, when the second melting was completed, the measured temperature would increase again toward that of the

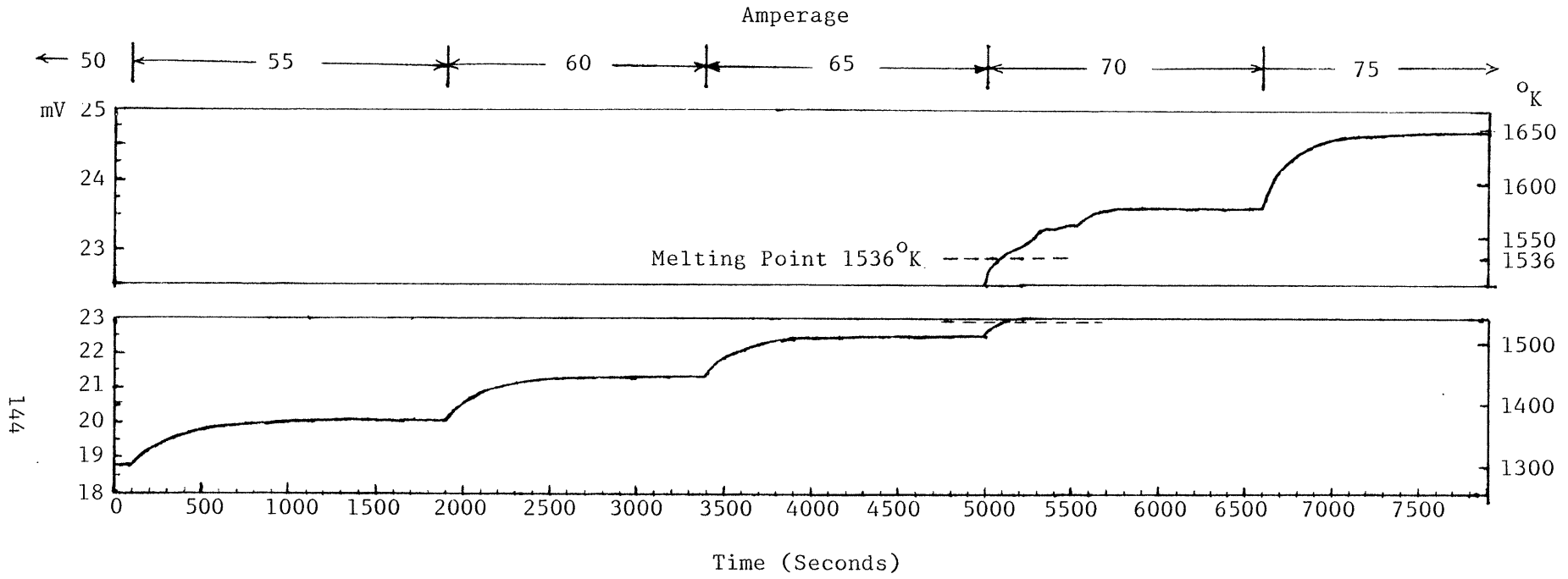

Figure 4.5a Stepped Heating of ASTAR Cylinder, Long Duration Test
(Lower thermocouple only, 3/10/87)

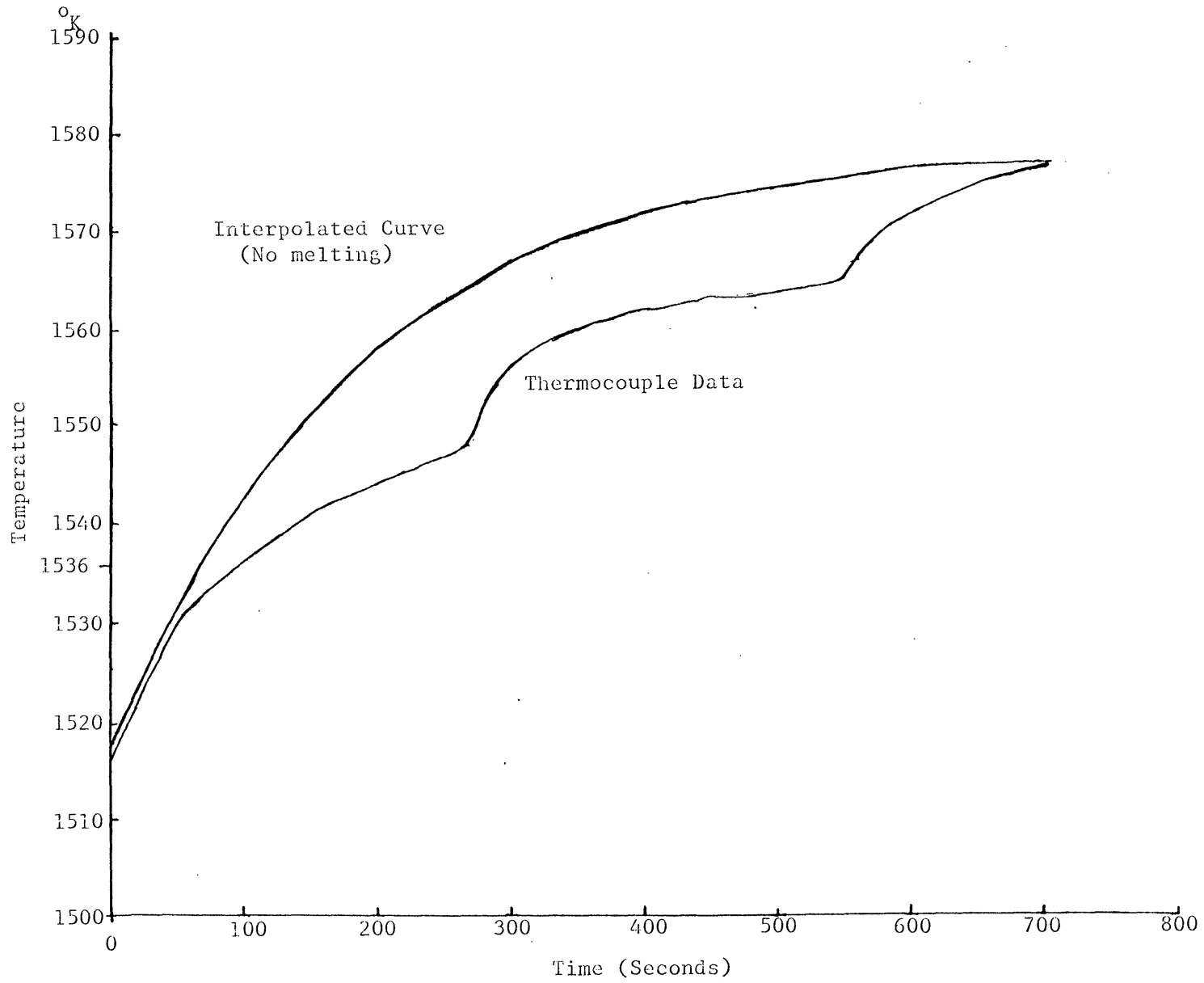

Figure 4.5b Detail of Melting from Figure 4.5a with Interpolated Curve for No Melting

furnace (as at about 400 sec and 550 sec in Figures 4.3 and 4.5b respectively). The presence of two separate masses of fluoride and two meltings is supported by freezing curves showing two humps before each of Figures 4.3 and 4.5b. (The freezing curve for the former is Figure 4.1.)

4.3 Second Test Capsule Set Furnace Run — Thermocouple Data

4.3.1 Purpose and Set-up

A second set of test capsules was used to try to clarify the thermocouple data. The placement of thermocouples on these was modified to the configuration shown in Figure 4.6. The lower thermocouples that had been welded to the cylinders were retained, but the wrapping wires were moved down as close to the weld points as possible. The upper welded thermocouples were removed, and the wires used to make new thermocouples. These were then fixed as closely as possible to the top ends of the cylinder by wrapping them with tungsten wire. The result of this was that these wires were probably shorted to the top edge of the cylinder, but care was taken to avoid shorting to the Ta sheet. This sheet was wrapped on the cylinders as shown in order to reproduce as closely as possible the thermal conditions experienced in the first test run. Considerable trial and error was required to set up the thermocouples while avoiding breakage and undesirable shorting. The alloy capsules were placed in the furnace in the same positions with respect to the heating elements as in the long duration test. The purpose was to reproduce any small variations in temperature caused by different view factors of the heating elements or furnace frame gap (see Figure 3.2).

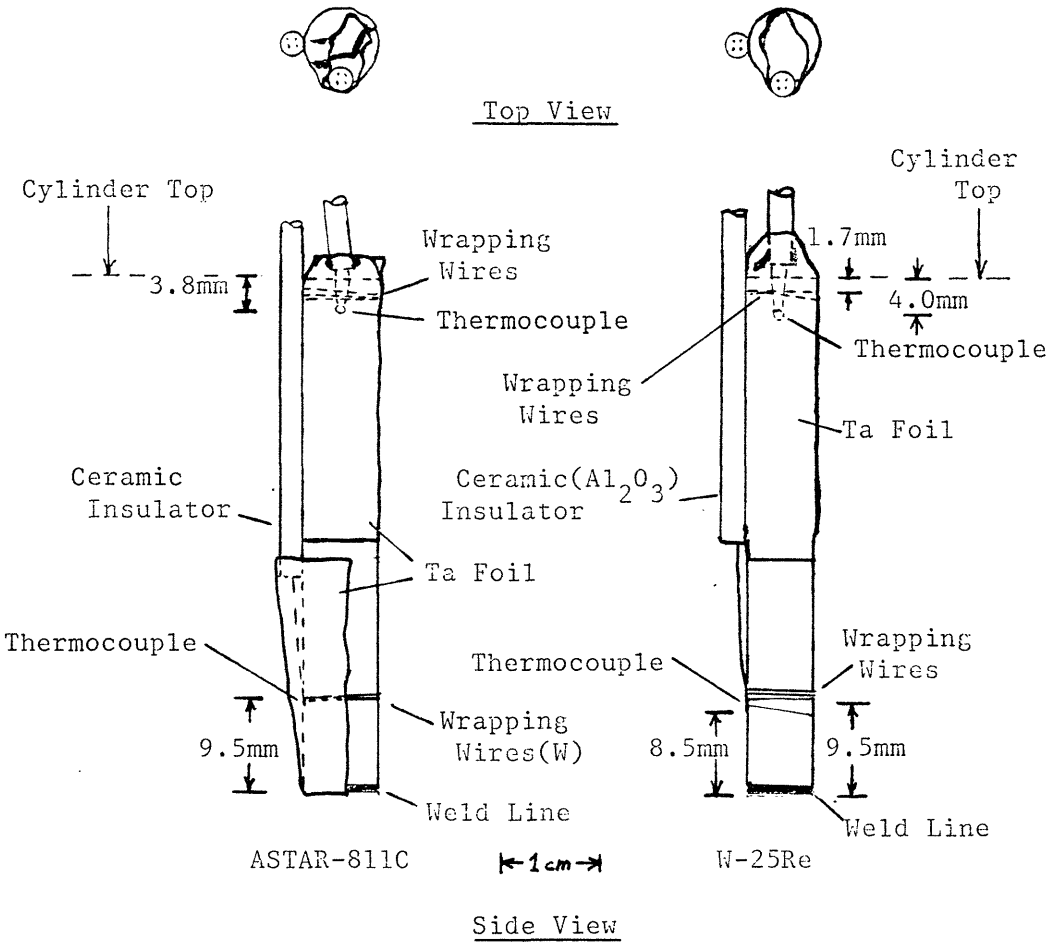

Figure 4.6 Modified Capsule Configuration for Second Test

It was hoped that by having a thermocouple at each end of the cylinder, the transfer of fluoride from one end to the other could be tracked. As a corollary it became possible to determine thermocouple errors and the temperature of one end of each cylinder.

4.3.2 Melting-Freezing Results — General Description

Figures 4.7 and 4.8 condense the temperature curves obtained in the melting-freezing cycles. (There were no cycles before these.) In both of these figures, the temperature scales are from the directly read voltages. Preceding each melting is a stepped heating sequence to the 65A level (not shown). Relatively short times in the molten state (1 hr. 43 min.; 1 hr. 32 min.) preceded the first two freezing events. Longer times as a liquid preceded the second two (42 hr. 57 min.; 42 hr. 17 min.). These times are from the beginning of the melting process (flattened curve) to the power being reduced to the 50A level from 68A.

Consistent with an isothermal phase change, the outputs for the lower thermocouples on the cylinders are nearly flat during melting except for some irregularities toward the end of each cycle. The upper ones show a lower slope than if no melting had occurred.

As the melting point (barring significant impurities in the fluoride) should be fixed, the flat curves can be used to find the error in the respective lower thermocouples. For the ASTAR, this is about $-14 \pm 3^{\circ}K$ and, for the W-25Re, $-125 \pm 3^{\circ}K$. The large value of the latter may be explainable by a short of the thermocouple. When the furnace was opened it was noted that the material preventing the W-25Re thermocouple wires from touching a radiation shield at a break in the ceramic insulation had been displaced.

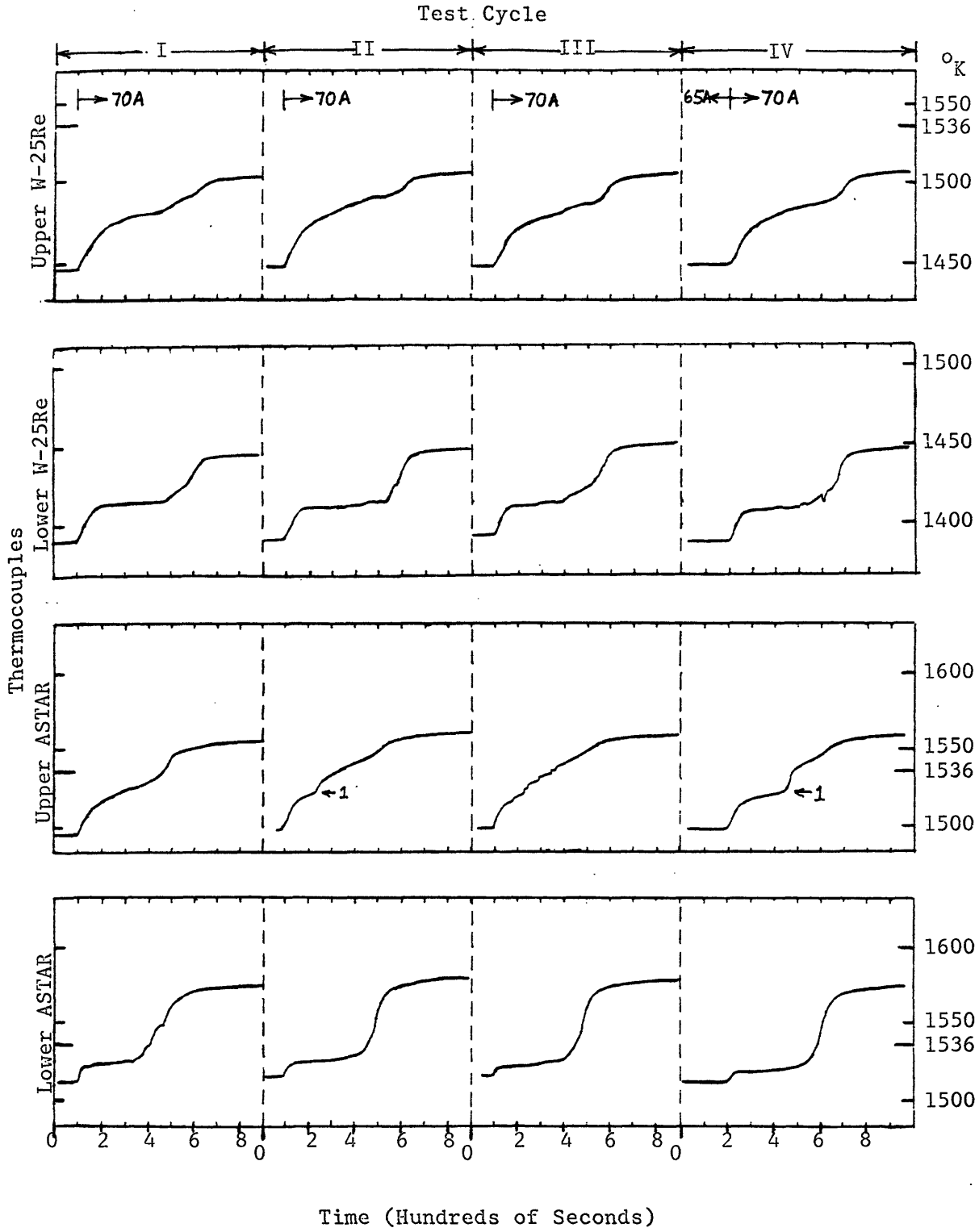

Figure 4.7 Melting Curves, Second Capsule Set Test

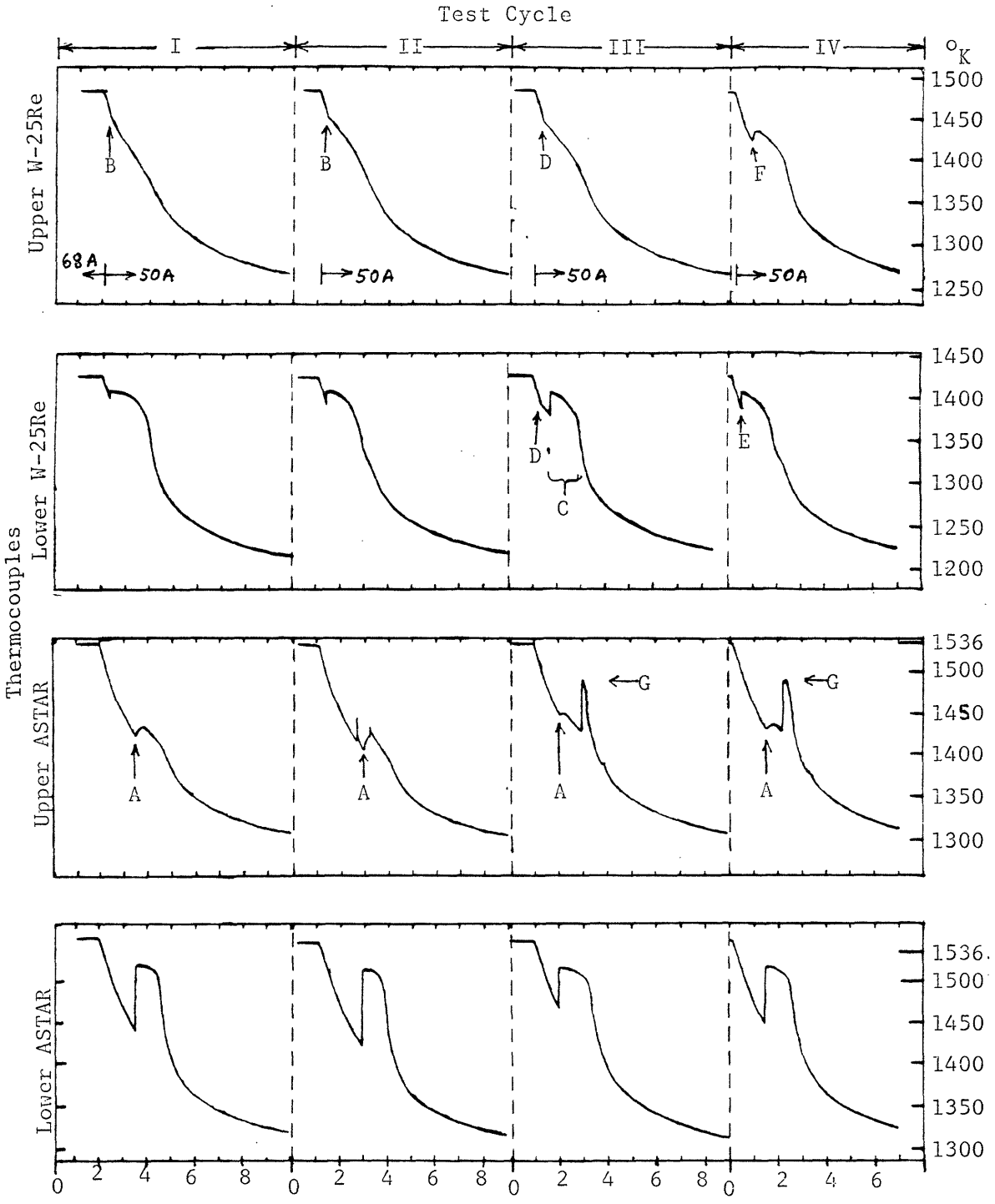

Figure 4.8 Freezing Curves, Second Capsule Set Test

The upper thermocouple curves look similar to those obtained from melting during the long duration capsule test. The curve recorded is clearly affected by the melting, but in both cases the temperature measurement point was separated from the melt along the tube. Note that in the data from the upper ASTAR thermocouple in each of cycles II and IV, there is an initial section followed by a kink at the points marked "1," which are both at the same temperature level. (During cycle III the chart recorder pen was partially malfunctioning.) The longer flattening in the fourth cycle implies an increase of material undergoing phase change near the thermocouple, though not enough to be so overwhelming an influence that the curve is perfectly flat. (Or it may be that the upper thermocouples, which are not welded to the tube and have a bead of about 1 mm diameter, are just not as well coupled to the tube temperature.) Using this flattening as a benchmark for the melting point gives a thermocouple error of $-18 \pm 3^{\circ}K$.

Turning now to the freezing parts of the cycle, consider the outputs from the lower thermocouples of each capsule. As in the long duration tests, one sees the "humps" showing heat released on crystallization, but now they all peak at the same level for a given cylinder, a level which is at or slightly below the melting levels in the previous figure. This correlation is reasonable. When the supercooled fluoride begins to freeze, it releases energy in the phase change which provides sensible heat to raise the temperature back to the melting point. If the cylinder were now perfectly insulated, freezing would stop.

Consider the upper ASTAR thermocouple data. The point labeled "A" in each cycle corresponds in time with the start of the crystallizations recorded

by the lower thermocouple. In the first cycle, the hump following "A" decays smoothly, and it appears that what is being seen is the transmitted heat pulse from the lower end of the cylinder (Appendix C). In the next cycles there is superposed a growing spike which was most likely caused by material accumulating over time at the top end of the cylinder. Note that the spike peak at G is below the level of the melting on the same thermocouple. (If used as a melting point benchmark, the thermocouple error would be -46°K.)

The data from the upper W-25Re thermocouple is more difficult to interpret. The points labeled "B" where the slope decreases in magnitude correspond in time to the crystallizations (with little supercooling) recorded by the lower thermocouple. However, there is no correspondence of the large hump labeled "C" and recorded in cycle III with a slope change in the upper thermocouple temperature. There are simultaneous decreases in slope magnitude in both the upper and lower W-Re thermocouple traces at D and D' respectively. In the fourth cycle also, the crystallization starting at point E does not show up at the upper end, but a hump does appear about 50 seconds later.

It is reasonable to assert that, given the smaller temperature jump on MgF_2 freezing at the lower end (less supercooling) of the W-25Re cylinder compared with the other cylinder, the effect at the top end should be attenuated. (This would be reinforced by lack of the lower half tantalum sheet cover, which acts as an insulator on the ASTAR cylinder.) So the muted responses at the points marked "B" are not suprising. However, the lack of time correlation in the final two cycles suggests the possibility of separate processes going on at the two ends.

At least for the ASTAR cylinder, transport of fluoride from the bottom to the top end has certainly been traced here. The impression is of a process that is proportional to time, probably attributable to transport caused by temperature and thus vapor pressure differences between the two ends of the cylinder.

In Table 4.1a are listed temperatures as read from the raw data. Error bars in each box indicate variations in readings at particular power settings, not absolute errors. Table 4.1b shows "corrected" temperatures using the absolute errors calculated above from melting point levels. Given the reproduction of thermal conditions in this test, the values in Table 4.1b should be close to the actual temperatures, for corresponding positions on the cylinders and power settings, that the cylinders experienced during the long duration test. (The correction factor for the upper ASTAR measurement has an error bar determined by the top and bottom of the depressed slope section in cycle IV). Since the thermocouple will be "leading" the temperature of the melting fluoride during the furnace temperature rise, the correction factor is taken at the upper limit, or 21°K. A 3°K error bar is then added as an estimate. All error bars in the corrected temperatures are from adding correction errors to existing ones in part a of the table. No error bar is added at the 75A level since there was only one data point (the data at 76A are extrapolated).

The "corrected" temperatures all are above those tabulated previously for the long duration test (Chapter III). The exception is at 68A, where the earlier value is between that for the upper and lower thermocouples shown here. It also should be mentioned that temperature corrections are probably a

Table 4.1a

Uncorrected Temperatures from Second Capsule Set Furnace Run (°K)

Current (A)	Lower W-25Re	Upper W-25Re	Lower ASTAR	Upper ASTAR
50	1204 ± 3	1249 ± 1	1300 ± 2	1290 ± 1
55	1262 ± 2	1315 ± 3	1375 ± 3	1360 ± 3
60	1329 ± 1	1382 ± 1	1446 ± 3	1430 ± 2
65	1391 ± 2	1446 ± 1	1514 ± 3	1498 ± 2
68	1426 ± 1	1484 ± 1	1551 ± 2	1535 ± 1
70	1449 ± 2	1505 ± 3	1577 ± 2	1559 ± 2
75	1506	1566	1641	1620
melt	1411 ± 3	•••	1522 ± 3.3	1518 ± 3
correction	+125 ± 3	•••	+14 ± 3.3	+18 ± 3 (center) 21°K (upper limit)*

*From low end of temperature plateau during melting (Cycle IV, Figure 4.7)

Table 4.1b

"Corrected" Temperatures from Second Capsule Set Furnace Run (°K)

Current (A)	Lower W-25Re	Lower ASTAR	Upper ASTAR
50	1329 ± 6	1314 ± 5	1311 ± 4
55	1387 ± 5	1389 ± 6	1381 ± 6
60	1454 ± 4	1460 ± 6	1451 ± 5
65	1516 ± 5	1528 ± 6	1519 ± 5
68	1551 ± 4	1565 ± 5	1556 ± 4
70	1574 ± 5	1591 ± 5	1580 ± 5
75	1631	1655	1637
76*	(1643)	(1667)	(1652)
melt	1536	1536	1536

* *Extrapolated for comparison with data of first capsule set furnace run (Chapter III).*

NOTE: Error bars in each box indicate variation in readings at each temperature, not absolute errors over the four test cycles. To obtain "corrected" temperature error bars, correction errors are added to original errors (no error bar at 75A level since data from only one cycle due to power supply problem).

function of temperature, and thus their use substantially away from the melting points introduces its own error.

4.3.3 Supercooling Behavior and Control

Using the lower thermocouple data from each cylinder, the supercooling ΔTs for each cycle were tabulated in Table 4.2. Clearly there is substantial scatter in these values, 50% or more. Misra and Whittenberger [13] encountered similar scatter for supercooling of various fluoride salt mixtures for particular samples, although Eichelberger ([17], p. 199) claims that only "impure" MgF_2 will supercool.

The problems with the long duration test temperatures make it difficult to quantatively evaluate the subcooling seen there. If a thermocouple is not directly adjacent to the freezing fluoride, the peak temperature measured in a freezing "hump" will be below the melting point of the fluoride: due to radiative loss along the tube length, the ΔT measured is low. During the long duration test the thermocouples were shorted near the tube center, and were thus probably most of the time separated by some length from the fluoride. Nonetheless, qualitatively one sees similar supercooling behavior when comparing the two metal containers -- generally, substantially more supercooling in ASTAR than in W-25Re.

What are the consequences of supercooling for a power generation system? During the supercooling period there will be lowered system conversion efficiency. In [48] we showed a 27% reduction in cycle efficiency with a 400°K peak temperature drop from 1900 to 1500°K, which forced the system into an off-design condition. The consequences here should be less significant, since even the worst supercooling in the ASTAR cylinder was under 100°K.

Table 4.2

Supercooling Data

	Supercooling, °K	
Cycle Number	**ASTAR 811-C**	**W-25Re**
I	80	9
II	92	17
III	50	31
IV	68	20

As is evident from Figure 4.8, the time spent in supercooled condition varies in proportion to the amount of supercooling. So even though the precise supercooling is unpredictable each time, one could devise a control law for compensating, which would presumably require a battery storage system. However, thermal dampening effects in the receiver might render such a system unnecessary.

However, it would clearly be more desirable to avoid the initial problem, so the question arises as to what could be done to decrease the supercooling. One option is simply to prefer the tungsten alloy over the ASTAR.

Another possibility is to add to the fluoride a substance that will promote nucleation. One procedure, as outlined by Lane in [47], involves selecting materials with similar crystalline structures and dimensions on the theory that they will have an affinity for the heat storage material, i.e. act as templates for crystallization. However, it is often found that, due to the complexities of nucleation and growth, other materials, with no apparent structural similarity to the storage material, will work as well or better.

A problem is that historically it has been found difficult to obtain nucleators whose effectiveness will persist over thousands of cycles. A further difficulty *a priori* for MgF_2 nucleation is that the high temperature implies relatively fewer solid materials available as candidate nucleators.

Nonetheless, Table 4.3 presents two candidate nucleators selected by the process suggested by Lane. Magnesium fluoride has a tetragonal lattice (base length a, vertical dimension length c, all angles 90°), and substances with dimensions within a few percent have been chosen based on the data in Donnay [49].

Table 4.3

Some Candidate Nucleators for MgF_2

	Cell Dimension Å		
Substance	**a**	**c**	**Melting Point**
Magnesium Fluoride	4.621	3.050	1536°K
Nickel Fluoride (NiF_2)	4.710	3.118	1747°K
Titanium Dioxide (TiO_2)	4.593	2.959	2098°K

CHAPTER V

SUMMARY, CONCLUSIONS, AND RECOMMENDATIONS

The purpose of this work has been to consider the feasibility of using MgF_2 for heat-of-fusion energy storage in a space solar thermal electrical generating system. The following steps have been accomplished:

1. *Systems Level Comparison of Solar Thermal System Using MgF_2 vs. one using LiF*

   This has shown that the system using MgF_2 heat storage can reduce system mass for a given power output by about 15%, despite increased insulation requirements for the higher temperature system. The mass comparison is very sensitive to mirror mass/area. A firmer result is a reduction in mirror area (and thus drag penalty) by about 22%.

2. *Theoretical Material Compatibility Evaluation of MgF_2 Storage*

   Available literature and expertise suggests that refractory metal alloys will be most suitable for MgF_2 containment, though long-term embrittlement will be a problem for tantalum-based alloys. Thermochemical calculations indicate the compatibility of MgF_2 with refractory metals. The permeability of these metals to hydrogen shows that pressure buildup in containers due to reactions with residual water should only be a transient phenomenon.

3. *Experimental Compatibility Test*

   A vacuum furnace capable of temperatures exceeding the melting point of MgF_2 was designed and constructed. Two capsules containing MgF_2, one each of the alloys W-25Re and ASTAR-811C, were kept above the MgF_2

melting point of 1536°K for over 2000 hours. Subsequent examinations of the capsules showed no indication of deleterious effects on the tungsten alloy. The ASTAR wall had deterioriated at isolated inclusions, apparently because of iron contamination during the manufacturing process. Later tests on the same capsule revealed the presence of an apparent hafnium compound as particles frozen into the fluoride. This is consistent with the relatively high reactivity of Hf.

4. *Data on Melting-Freezing Behavior of MgF_2*

Tests in the vacuum furnace showed clearly both the isothermal melting of MgF_2 and its supercooling when frozen. The melting point was used to extract corrected thermocouple temperatures. The magnitude of the latter was ~50-80°K for the ASTAR capsule and ~10-30°K for the W-25Re. There was flouride migration in the capsule indicated both by the distribution of the frozen melt and the thermocouple data.

Thus, no basic obstacles have been found to the use of MgF_2 for solar thermal energy storage. To extend the results given here, the following steps are suggested.

- A more detailed thermo-optical design of the mirror-receiver system, paying particular attention to whether relaxed mirror qualities for lower temperature systems will reverse the advantage of the MgF_2 system;
- Further testing to understand the nature of the particles found in the ASTAR sample and the effect of their formation on the metal properties. One would like to be able to do standard mechanical properties tests on metal slices held in MgF_2 for sufficient periods

to cause Hf depletion, but this may be too slow to be practical. On the other hand, it may be found that the particle formation can be controlled by controlling contaminant levels (e.g. of O_2, N_2, C) in and around the container.

- Accelerated thermal cycling tests of alloys containing MgF_2. DeVan suggests that the solubility of refractory metals in liquid MgF_2 may be sufficient that over the power system lifetime thermal gradients would cause net transport of metal through the liquid. In testing one would have to reproduce as many cycles of the system life as possible. Zero-g testing to eliminate convective effects is probably required. An intermediary experiment to find metal solubility in liquid MgF_2 could be performed by melting the fluoride in a metal container, pouring it into a vessel of another material (probably ceramic) then counting metal deposited there and left in the solidified MgF_2.
- Effects of supercooling. The actual effects on system performance of supercooling, given thermal inertia effects and various cooling rates, should be studied.

REFERENCES

1. Hallinan, G.J., *Space Station WP-04 Power System, Volume 2: Study Results, Final Study Report.* NASA-CR-179587, Rockwell International Corporation, 19 January 1987.

2. Lane, George A., editor, *Solar Heat Storage: Latent Heat Materials, Volume I: Background and Scientific Principles.* CRC Press, Inc., Boca Raton, FL 1983.

3. Jaffe, L.D., *Optimization of Dish Solar Collectors With and Without Secondary Concentrators.* JLP Publication 82-103, N83-19224, Jet Propulsion Laboratory, Pasadena, CA, 15 May 1982.

4. McKenna, R., Niggemann, R., and Thollot, P., "Solar Dynamic Power for Space Station." IECEC 84154, *Proceedings of the Intersociety Energy Conversion and Engineering Conference.*

5. *Space Photovoltaic Research and Technology 1986: High Efficiency, Space Environment, and Array Technology.* Proceedings of a conference held at NASA Lewis Research Center, 7-9 October 1986, NASA CP-2475, 1986.

6. *The 1985 Goddard Space Flight Center Battery Workshop.* Proceedings of a workshop held at NASA Goddard Space Flight Center, NASA CP-2434, 1986.

7. Baraona, Cosmo R., *Space Station Power System.* N87-26447 (included in Reference 5, p. 321).

8. *SNAP-8 Electrical Generating System Development Program,* NASA CR-1907, Aerojet-General Corporation, November 1971.

9. Burns, R.K., *Preliminary Thermal Performance Analysis of the Solar Brayton Heat Receiver,* NASA TND-6268.

10. Namkoong, D., *Measured Performance of a 1089°K (1500°F) Heat Storage Device for Sun-Shade Orbital Missions.* NASA TN D-6665, February 1972.

11. Mendelson, I., ed., *Design and Fabrication of Brayton Cycle Solar Heat Receiver.* Final report, NASA CR-72872, General Electric Nuclear Systems Programs, Space Systems, Cincinnati, OH, July 1971.

12. Harrison, R.W., and Hendrixson, W.H., *Compatibility of Columbium Base Alloys with Lithium Flouride.* NASA CR-1526, General Electric Company Space Division, Cincinnati, OH, March 1970.

13. Misra, Ajay K., and Whittenberger, J. Daniel, *Flouride Salts and Container Materials for Thermal Energy Storage Applications in the Temperature Range 973 to 1400°K.* NASA TM-89913 N87-24026, 22nd Intersociety Energy Conversion Engineering Conference, August 10-14, 1987.

14. Lurio, Charles A., *An Evaluation of Solar Mercury Rankine Space Power.* S.M. Thesis, MIT Space Systems Laboratory Report #3-83, January 1983.

15. Whittinghill, George R., *Preliminary Design of a High Temperature Solar Space Power System.* S.M. Thesis, MIT Space Systems Laboratory Report #17-83, February 1983.

16. Personal communication with Dr. Robert Gidding, General Electric Corporate Research Development Center, Schnenectady, NY.

17. Eichelberger, J.L., *Investigation of Metal Flouride Thermal Energy Storage Materials: Availability, Cost, and Chemistry.* Final Report, COO-2990-6, Pennwalt Corporation Technology Center, King of Prussia, PA, December 1976.

18. Janz, G.J., Physical Properties Data Tables; properties of MgF_2, obtained by personal communication, Rensselaer Polytechnic Institute, Troy, NY, 1983.

19. Joint Army, Navy, Air Force (JANAF) Thermochemical Tables. 1964 to date.

20. Fraser, Wilson M. Jr., Chairman, *Proceedings of the Solar Dynamic Systems Workshop Part II -- Collection and Thermal Storage.* August 1-3, 1984, NASA Johnson Space Center Propulsion and Power Division, 1984.

21. Annen, K.D., Martinez-Sanchez, M., et al, *A Study of Pulsed Solar Brayton Space Power Systems, Volume I.* ARI-RR-396, Aerodyne Research, Inc., Billerica, MA, June 1984.

22. Pitts, Donald R., and Sissom, Leighton E., *Theory and Problems of Heat Transfer.* Schaum's Outline Series, McGraw Hill Book Co., NY, 1977.

23. Rohsenow, Warren M., and Hartnett, James P., eds., *Handbook of Heat Transfer.* McGraw Hill Book Co., NY, 1973.

24. Cooper, R.H., Jr., and Hoffman, E.E., Eds., *Refractory Alloy Technology for Space Nuclear Power Applications.* Proceedings of a Symposium held at Oak Ridge, Tennessee, August 10-11, 1983, CONF-8308130 Technical Information Center, Office of Scientific and Technical Information, U.S. Dept. of Energy, January 1984.

25. Barin, H., and Mayer, S.W., "Law of Corresponding States for Fused Salts," *The Journal of Chemical Physics.* Vol 35, No. 3, Sept. 1961, pp. 820-826.

26. *Optical Crystals by Optovac* -- Handbook 82. Optovac, Inc., North Brookfield, MA, 1982.

27. Barin, L., and Knacke, O., *Thermochemical Properties of Inorganic Substances.* Springer-Verlag, Berlin, 1973.

28. Barin, L., Knacke, O., and Kubaschewski, O., *Thermochemical Properties of Inorganic Substances, Supplement*. Springer-Verlag, Berlin, 1977.

29. Personal communications with Walter Hargreaves and Robert Sparrow, Optovac, Inc., North Brookfield, MA.

30. Personal communication with Patrick J. Early, Rembar, Inc.

31. Iwamoto, Hiromi, and Higuchi, Fumiaki, *Crucibles for Vapor Depositions*. Sumitomo Electric Industries Ltd., Appl. 85/54854, 19 March 1985, Jpn. Kokai Tokkyo Koho JP 61/213371 A2[86/213371], 22 Sept. 1986, 5 pp.

32. Wilkinson, Walter D., *Properties of Refractory Metals*, Gordon and Breach, NY, 1969.

33. Machlin, I., Begley R.T., and Weisert, E.D., Eds., *Refractory Metal Alloys: Metallurgy and Technology* (Proceedings, Symposium on Metallurgy and Technology of Refractory Metal Alloys, Washington, DC, 1968). Plenum Press, New York, 1968.

34. Brewer, L., "The Thermodynamic Properties of the Oxides and Their Vaporization Processes," *Chemical Review*. Vol. 52, p. 1, 1953.

35. Chang, Luke L.Y., and Phillips, Bert, "Phase Relationships in Refractory Metal-Oxygen Systems," *Journal of the American Ceramic Society*. Vol. 52, No. 10, pp. 527-33.

36. Liu, C.T., Inouye, H., and Carpenter, R.W., "Structure and Properties of Internally Oxydized Ta-8% W-2% Hf(T111) Alloy," *Metallurgical Transactions*. Vol. 4, August 1973, pp. 1839-49.

37. Gaskell, David R., *Introduction to Metallurgical Thermodynamics*. Scripta Publishing, Washington, DC/McGraw Hill, NY, 1973.

38. Lupis, C.H.P., *Chemical Thermodynamics of Materials*. Elsevier Science Publishing Co., NY, 1983.

39. Denbigh, Kenneth, *The Principles of Chemical Equilibrium*, Second Edition. Cambridge University Press, 1966.

40. Hurz, G., Speck, H., Fromm, E., and Jehn, H., *Physics Data, Gasses and Carbon in Metals: Thermodynamics, Kinetics, and Properties*. Part IX, Group V A Metals (3); Tantalum (Ta), 1981, No. 5-9/Part X Group IV A Metals (1); Chromium, Tungsten (Cr, W), 1980, No. 5-10, Max-Plank Instutit fur Metallforschung, Institut fur Werkstoffwissenschaften, Stuttgart, Germany, Fachinformationszentrum Energie, Physik, Mathematik, GMBH, Karlsruhe, Germany.

41. Galasso, Francis S., *Structure and Properties of Inorganic Solids*. Pergamon Press, NY, 1970.

42. Myshkis, A.D. et al, *Low Gravity Fluid Mechanics*. Springer-Verlag, Berlin, 1987. (Translation of *Gidromekhanika Nevesomosti* © Nauka Moscow 1976.)

43. Reynolds, William C., and Satterlee, Hugh M., "Liquid Propellant Behavior at Low and Zero g," in NASA SP-106, *The Dynamic Behavior of Liquids in Moving Containers (with Applications to Space Vehicle Technology)*. H. Norman Abramson, Ed., 1966.

44. Kubaschewski, O., *Iron Binary Phase Diagrams*. Springer-Verlag, Berlin, 1982.

45. Moffat, William G., *The Handbook of Binary Phase Diagrams*, Vol. 3. Genium Publishing Co.

46. Touloukian, Y.S., *Thermophysical Properties of High Temperature Solid Matter*, Vol. 4. MacMillan, New York, 1967.

47. Lane, George A., "Crystallization" in [2].

48. Lurio, C.A., and Martinez-Sanchez, M., *Evaluation of a Solar Brayton Space Power System Using Thermal Storage at Reduced Temperature*. Space Systems Laboratory Report SSL#21-83, June 1983.

49. Donney, J.D.H., and Ondik, Helen, M , *Crystal Data, Determinative Tables*. 3rd Ed., Vol. 2, U.S. Dept. of Commerce, National Bureau of Standards, Washington, DC, 1973. (Other volumes at later dates)

50. Elliott, Rodney P. Constitution of Binary Alloys, 1st Supplement, McGraw-Hill, New York, 1965

APPENDIX A

Thermal Conductivity of Solid LiF and MgF_2

As noted above, properties data for the fluorides considered here is sparse. Figure A1 shows data on thermal conductivity from several sources. Koyama [A1] determined the conductivity of polycrystaline opacified MgF_2 between 298 and 1173°K which follows the relation

$$K = \frac{3.17}{(T(^{\circ}K)\times 10^{-3})} + 0.85 \qquad (\frac{W}{m-^{\circ}K}) \qquad (A1)$$

Without specifying the crystal structure, Sreenivasan and Altman [A2] show a similar curve for LiF to the same temperature which, however, exhibits considerable flattening before the melting point. By contrast, the data reproduced by Touloukian [A3] shows increasing conductivity of LiF. This last set of data was derived from work on monocrystalline LiF. There may be radiative transmission effects present here.

In view of the polycrystalline nature of the fluoride in the thermal energy storage system, Koyama's data was extrapolated to obtain conductivity at the melting point. (The frozen MgF_2 after the vacuum melting was polycrystalline.) Given the similarity of the curves, the LiF data from Sreenivasan is also accepted and extrapolated. Note that due to the higher temperatures, radiative effects might increase the effective conductivity of MgF_2 relative to that of LiF.

No data on molten conductivity of MgF_2 has been found.

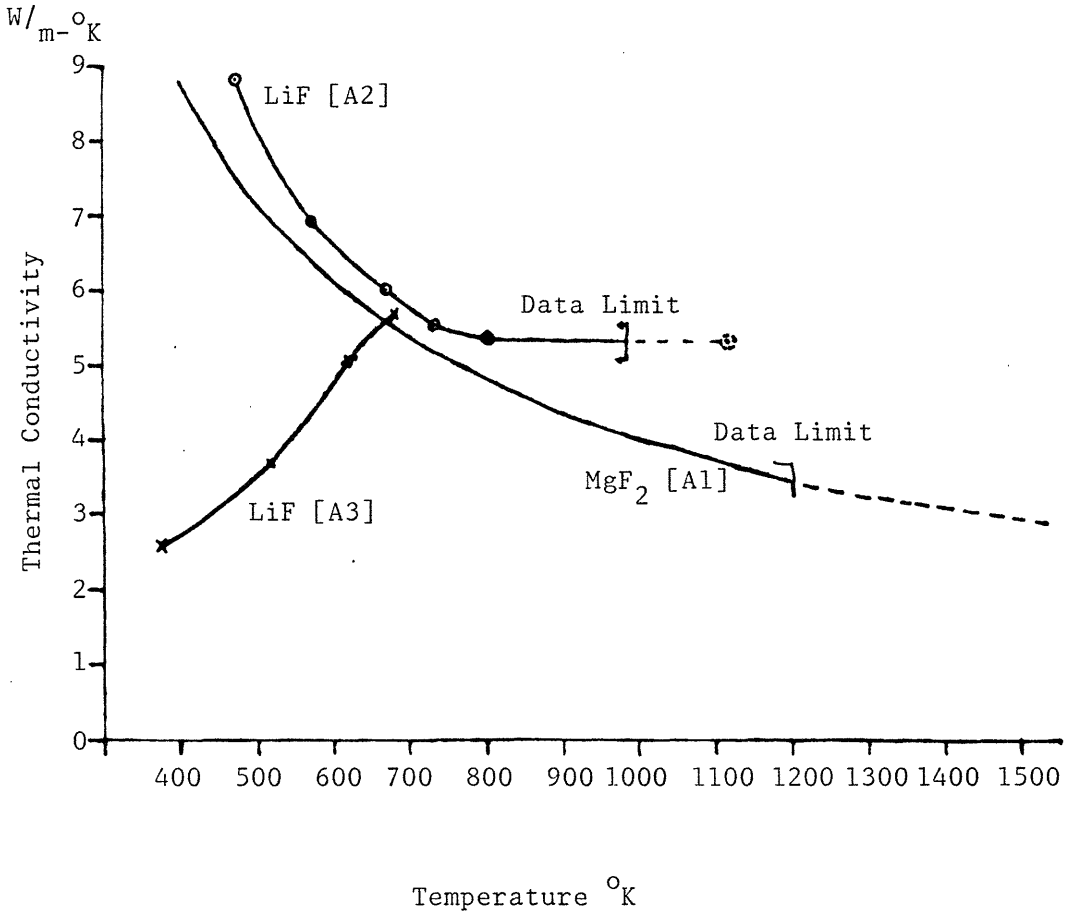

Figure A1 Thermal Conductivity Data for Solid LiF and MgF_2

References

A1. Koyama, Karl, "Thermal Conductivity of Magnesium Fluoride Between 25° and 900°C," *Journal of the American Ceramic Society*. Vol. 52, No. 4, April 1969, pp. 223-4.

A2. Sreenivasan, K., and Altman, M., "The Determination of Thermal Diffusivities of Thermal Energy Storage Materials. Part II: Molten Salts Beyond the Melting Point," *Transactions of the ASME: Journal of Engineering for Power*. July 1969, pp. 189-97.

A3. Touloukian, Y.S. et al, *Thermophysical Properties of Matter, Volume 2: Thermal Conductivity, Non-Metallic Solids*. TPRC Data Series IFI/Plenum, NY, 1970, pp. 636-40.

APPENDIX B

Effect of Thermocouple Circuit Errors

Faults in thermocouple circuits can cause significant errors. A few examples are given here along with the ideal circuit. These are only formally correct, and intended to show some of the characteristics of the circuit errors.

B.1 Ideal Circuit

The thermocouple operates by taking advantage of the Seebeck voltage generated by a wire in a thermal gradient, i.e.

$$dE = \alpha_A dT \tag{B1}$$

where

E = emf

T = temperature

α = Seebeck coefficient for a homogeneous wire

Consider the circuit in Figure B1a, consisting of two types of wire welded together at two points: where the temperature is to be measured at T_2, and at a reference point with lower temperature T_o. The circuit is open, the voltage measured with a voltmeter, the reference point being in the "negative" let as seen from there. Assuming that α_A, α_B are both positive and adding voltage drops clockwise around the circuit

$$- V - \alpha_A(T_2-T_m) + \alpha_B(T_2-T_o) - \alpha_A(T_m-T_o) = 0 \tag{B2a}$$

$$V = (\alpha_B-\alpha_A)(T_2-T_o) \tag{B2b}$$

$$\equiv \alpha_{BA}(T_2-T_o) \tag{B2c}$$

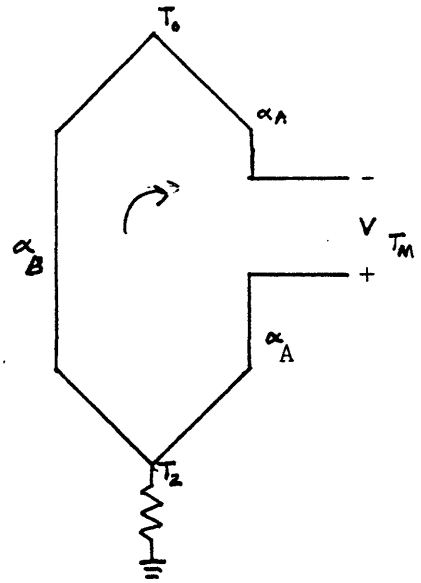

Figure B1a 'Ideal' Thermocouple

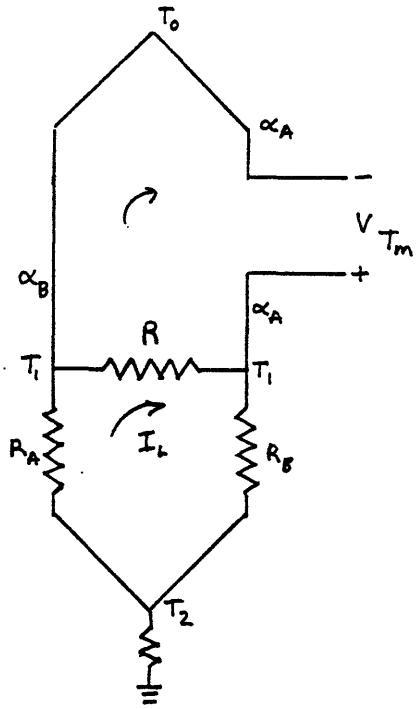

Figure B1b Thermocouple with Short

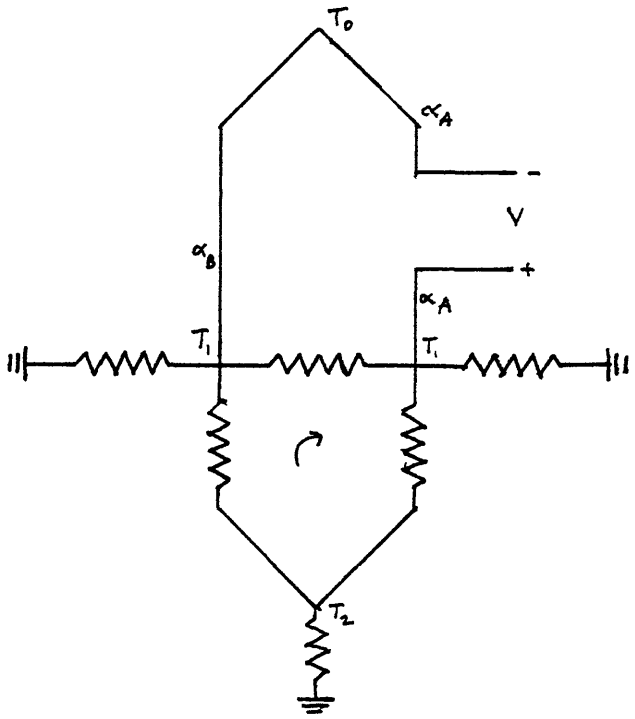

Figure B1c Thermocouple with Short Connected to Ground

where α_{BA} is the relative Seebeck coefficient (actually a function of T) used to determine temperatures relative to a standard (most often 0°C), and the temperature at the voltmeter T_m drops out. For the temperature measurements carried out in this research the ideal circuit would be unavoidably grounded at the measurement point T_2, because the capsules were metal and supported by the metal, grounded part of the furnace isolated from the heating circuit. This should have no effect on temperature measurements, as long as the rest of the circuit is kept isolated from ground.

B.2 Circuit Faults

Faults in the thermocouple wiring cause currents in parts of the circuit, which by Ohm's law change the voltage read at the voltmeter. For example, consider the circuit shown in Figure B1b, which includes a short across the leads at temperature T. There are two voltage loops to be considered; in the lower one there is a current I_L. Adding voltage drops in the upper and lower circuits gives, respectively,

$$- V - \alpha_A(T_1-T_m) + \alpha_B(T_1-T_o) - \alpha_A(T_m-T_o) - I_L R = 0 \qquad \text{(B3a)}$$

$$I_L(R+R_A+R_B) - \alpha_A(T_2-T_1) + \alpha_B(T_2-T_1) = 0 \qquad \text{(B3b)}$$

Solving for I_L in (B3b) and substituting into B3a gives

$$V = \alpha_{AB}(T_1-T_o) - \left(\frac{R}{R+R_A+R_B}\right)\alpha_{BA}(T_2-T_1)$$

which formally shows that the effect of this type of short will be to read out the temperature of the short, as long as $(T_2-T_1) \ll (T_1-T_o)$. This is similar to, but not precisely identical with, the condition encountered in both furnace tests. (The difference between the tests was in the quantity T_2-T_1 which was potentially greater in the first than in the second due to the

larger physical separation of the thermocouple head and the shorting wire.) In both tests, the wrapping wire caused a short to ground which is represented schematically in Figure B1c. This introduces additional potential biasing currents which depend upon the peculiarities of the grounding connection.

Another example of a circuit fault is shown in Figure B2. In this case there is an inadvertent ground in the circuit, similar to what might have occurred in the second furnace test where, as stated in the main text, there was a possibility of a short to the insulation (here assumed to be at temperature T_1). Formally counting voltage drops around the loop for the upper part and lower right one respectively gives

$$- V - \alpha_A(T_2-T_m) + \alpha_B(T_2-T_o) - \alpha_A(T_m-T_o) - I_oR_1 = 0$$

$$I_o(R_{g_1}+R_{g_2}+R_1) + \alpha_A(T_2-T_1) = 0$$

Combining and cancelling terms,

$$V = \alpha_{BA}(T_2-T_o) + \frac{R_1}{R_{g_1}+R_{g_2}+R_1}\alpha_A(T_2-T_1)$$

While R_{g_1}, R_{g_2} are unknown (they are probably from contact resistance) and R_1 is just the wire resistance, one could plausibly argue that the resistance ratio may not be far below 1. The value of $(T_1-T_m)/(T_2-T_m)$ depends upon exactly where the short is, but might be about 1/3. Then also α_A is by definition larger than α_{BA}. So it is quite reasonable that substantial errors in the signal (such as those in the W-25Re thermocouples in the second furnace run) could occur in this or a similar way.

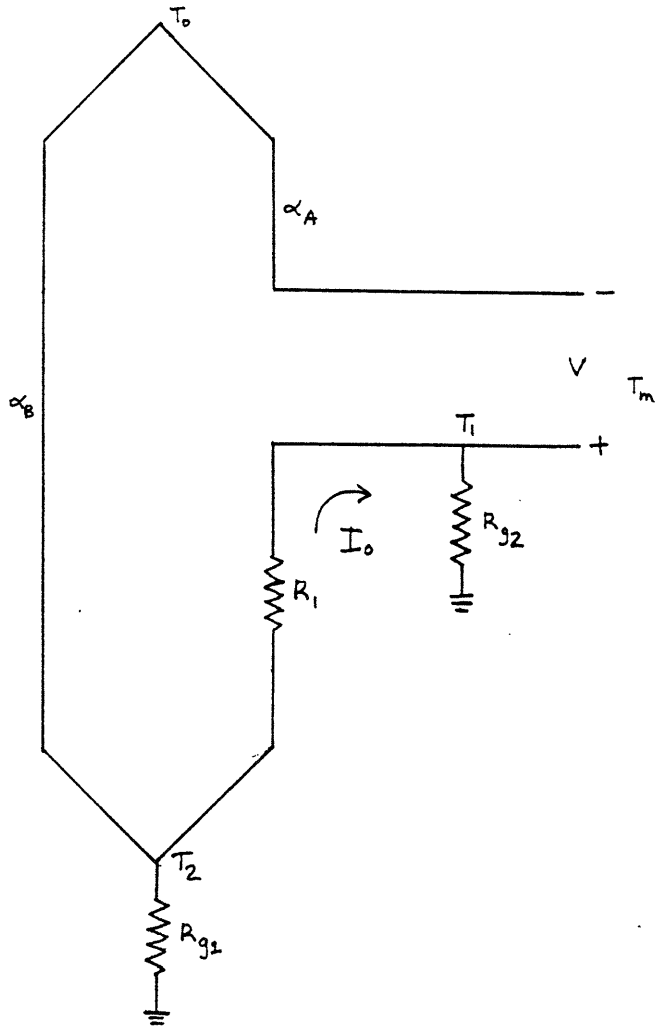

Figure B2 Thermocouple With Short to Ground on Single Lead

APPENDIX C

Heat Transmission and Loss During Phase Change

Figure 4.8 showed thermocouple data during freezing of the fluoride in the two samples. As noted in the main text, the heat pulses recorded by the lower thermocouples during freezing seemed to be detected at the same time by the upper thermocouples, though with lower temperature peaks.

One plausible mechanism for this is transmission of heat by conduction along the tube, accompanied by losses by radiation to the sides. The model below considers these effects.

Start with a tube of length L and thickness δ. At any point along the length the heat balance per unit length may be stated as

$$Ac_p\rho \frac{\partial T}{\partial t} = Ak \frac{\partial^2 T}{2x^2} - \pi D\sigma\epsilon(T^4-T_{bk}^4) \qquad (C1)$$

where

A = cross-sectional area, m^2

c_p = specific heat J/kg-$^\circ$K

ρ = metal density kg/m^3

k = thermal conductivity W/m-$^\circ$K

T = local temperature, $^\circ$K

T_{bk} = temperature of surrounding background environment, $^\circ$K

D = tube diameter

ϵ = tube emmisivity

σ = Stefan-Boltzmann constant

It is assumed that the wall thickness is relatively small, i.e. that $A \approx \pi D\delta$ and also that $(T-T_{bk})$ is small enough that the radiation term may be linearized ($(T^4-T_{bk}^4) \approx 4T_{bk}^3(T-T_{bk})$). Then this becomes

$$\frac{\partial T}{\partial t} = \alpha \frac{\partial^2 T}{2x^2} - \frac{4\epsilon T_{bk}^3}{c_p \rho \delta} (T-T_{bk}) \qquad (C2)$$

where the thermal diffusivity $\alpha \equiv k/\rho c_p$. As the coefficient of the second term has the units 1/time a characteristic radiation time τ_R is defined. Also, let $T' = T-T_{bk}$ be used instead of T,

$$\frac{\partial T'}{\partial t} = \alpha \frac{\partial^2 T'}{\partial x^2} - \frac{(T')}{\tau_R} \qquad (C3)$$

Assume that initially the value of $T' = 0$ throughout the tube, then take the Lapace transform of (C3), which gives

$$s\hat{T} = \alpha \frac{d^2\hat{T}}{dx^2} - \frac{\hat{T}}{\tau_R} \qquad (C4)$$

where the transform is represented by $\hat{T}$. This can be restated as

$$\frac{d^2\hat{T}}{dx^2} - \left(\frac{s}{\alpha} + \frac{1}{\alpha\tau_R}\right) \hat{T} = 0 \qquad (C5)$$

Then let the solution of this be given as

$$\hat{T} = A(s)e^{\beta(s)x} + B(s)e^{-\beta(s)x} \qquad (C6a)$$

with

$$\beta(s) \equiv \sqrt{\frac{s}{\alpha} + \frac{1}{\alpha\tau_R}} \qquad (C6b)$$

At $x = 0$, $\hat{T} = A + B$ sets a boundary condition if the transform of the value of T' over time is known. Let it be that T' follows a step function that at $t = 0$ jumps to the value T_1' (the difference between the fluoride melting point T_m and T_{bk}) and then drops to back to zero at a time t_1. This represents the jump in temperature at the end of the experimental cylinder

that contains the freezing MgF_2. The transform of this jump is

$$\hat{T}(x=0) = \int_0^\infty e^{-st} f(t)dt = \frac{T_1'}{s}(1-e^{-st_1}) \qquad (C7a)$$

where

$$f(t) = T_1' \qquad 0 < t < t_1$$
$$= 0 \qquad t > t_1$$

Thus

$$\frac{T_1'}{s}(1-e^{-st_1}) = A + B \qquad (C7b)$$

Another boundary condition may be set by assuming the tube end is insulated,

$$\left(\frac{\partial T'}{\partial x}\right)_{x=L} = 0 \quad \text{or} \quad \left(\frac{d\hat{T}}{dx}\right)_{x=L} = 0 \qquad (C8a)$$

which gives

$$Ae^{\beta(s)L} - Be^{-\beta(s)L} = 0 \qquad (C8b)$$

Resolving (C7b) and (C8a) results in

$$A = \frac{\frac{T_1'}{s}(1-e^{-st_1})}{1+e^{2\beta L}} \quad , \quad B = \frac{T_1'}{s}(1-e^{-st_1})\frac{e^{2\beta L}}{1+e^{2\beta L}} \qquad (C9)$$

which is then substituted into (C6a) to give

$$\hat{T} = \frac{\frac{T_1'}{s}(1-e^{-st_1})}{1+e^{2\beta L}}\left[e^{\beta x} + e^{\beta[2L-x]}\right] \qquad (C10)$$

but since our interest is in the temperature at the tube end, set x = L which results in the simplification

$$\hat{T} = \frac{T_1'}{s}(1-e^{-st_1})\frac{1}{\cosh\beta L}$$
$$= \frac{T_1'}{s}\frac{1}{\cosh\left(\sqrt{s+\frac{1}{\tau_R}}\frac{L}{\sqrt{\alpha}}\right)} + \frac{T_1'}{s}\frac{e^{-st_1}}{\cosh\left(\sqrt{s+\frac{1}{\tau_R}}\frac{L}{\sqrt{\alpha}}\right)} \qquad (C11)$$

The basic reverse transform is achieved with the first term; the second will be the same but for a shift in time to t_1 so that it is present only for $t > t_1$ and evaluated at $t - t_1$ rather than t.

Referring to Bateman, p. 259 [C1], transform #40 is useable with the identification of this quantities as $p = s + \frac{1}{\tau_R}$, $l = \frac{L}{\sqrt{\alpha}}$, $i\omega = \frac{1}{\tau_R}$, $x = 0$ where p is his transform variable. Thus there is required an exponential term in the reverse transform by the identity for a general reverse transform $\hat{f}^{-1}$ that

$$\hat{f}^{-1}(p - a) = e^{at}f(t) \tag{C12}$$

where here $a = -\frac{1}{\tau_R}$.

Then the first term of (C11) transforms to

$$T'_{(t<t_1)}(t,L) = T'_1 e^{-t/\tau_R}\left[\frac{e^{t/\tau_R}}{\cosh\left(\frac{L}{\sqrt{\alpha\tau_R}}\right)} - 2\pi\sum_{n=0}^{\infty}\frac{(n+\frac{1}{2})(-1)^n}{(n+\frac{1}{2})^2\pi^2 + \frac{1}{\tau_R}\frac{L^2}{\alpha}}e^{-(n+\frac{1}{2})^2\pi^2\frac{\alpha}{L^2}t}\right]$$

$$= T'_1\left[\frac{1}{\cosh\left(\frac{L}{\sqrt{\alpha\tau_R}}\right)} - 2\pi\sum_{n=0}^{\infty}\frac{(n+\frac{1}{2})(-1)^n}{(n+\frac{1}{2})^2\pi^2 + \frac{1}{\tau_R}\frac{L^2}{\alpha}}e^{-[(n+\frac{1}{2})^2\pi^2\frac{\alpha}{L^2} + \frac{1}{\tau_R}]t}\right] \tag{C13}$$

The large bracketed factor will henceforward be designated as g(t). Thus the full expression for T'(t,L) can be stated as

$$T'(t,L) = T'_1\left[0.4280 - 2\pi(0.1065e^{-0.1165t} - 0.06139e^{-0.6065t} + 0.03912e^{-1.5865t} - 0.02842e^{-3.0505t} + \cdots)\right] + T'_1 u(t-t_1)g(t-t_1) \tag{C14}$$

where $u(t-t_1)$ is a unit step function that is zero before $t = t_1$. Here some

reasonable estimates of the constants have been made: $\alpha = 2.5 \times 10^{-5}$ m^2/sec [C2] (for tantalum), $L \approx 3.175 \times 10^{-2}$ m (from the empty tube length in the test capsules), $t_1 \approx 90$ sec (from Figure 4.8, cycle I, thermocouple 16). Also, with $c_p \approx 157$ J/kg°K, $\delta \approx .8 \times 10^{-3}$m, $\epsilon = .15$, and $T_{bk} \approx 1500$°K there results $\tau_R = 18.1$ sec.

One can compare the result (C14) with that from the case of zero radiation loss, i.e. with $\epsilon = 0$ or $\tau_R \longrightarrow \infty$, which is

$$T'(t,L)_{\text{(no radiation loss)}} = T_1' \left[1 - 2\pi(0.2026e^{-0.06125t} - 0.06755e^{-0.5513t} + 0.04053e^{-1.5313t} - 0.02895e^{-3.0013t} + \cdots) \right] \quad \text{(C15)}$$

Both (C14) and (C15) are plotted (normalized) in Figure C1. It is seen that the radiant loss both slows the temperature increase and limits the peak value of T'(L) which is determined by the first term in (C13). Recalling the data in Figure 4.8, cycle I for the upper ASTAR thermocouple, #17, clearly the peak reached was not close to 40% of the temperature jump on the lower thermocouple. Nonetheless, the general shape, though superposed on a rapidly decreasing background temperature, is similar.

Changes in the constants contributing to the first term of (C13) can have an effect on the achievable value of T'. For example, if α drops to 2×10^{-5} m^2/sec (the lower end of the range given in the reference) then the peak of T' is 0.364T'. An increase in emissivity would also reduce T' (for example. for $\epsilon = .2$ the peak is at 0.346T').

The effect of a change in T_{bk} correlates well with the data. Referring back to Figure 4.8, the jumps marked "A" are larger the larger the corresponding jumps on the lower thermocouple #16. Then consider the

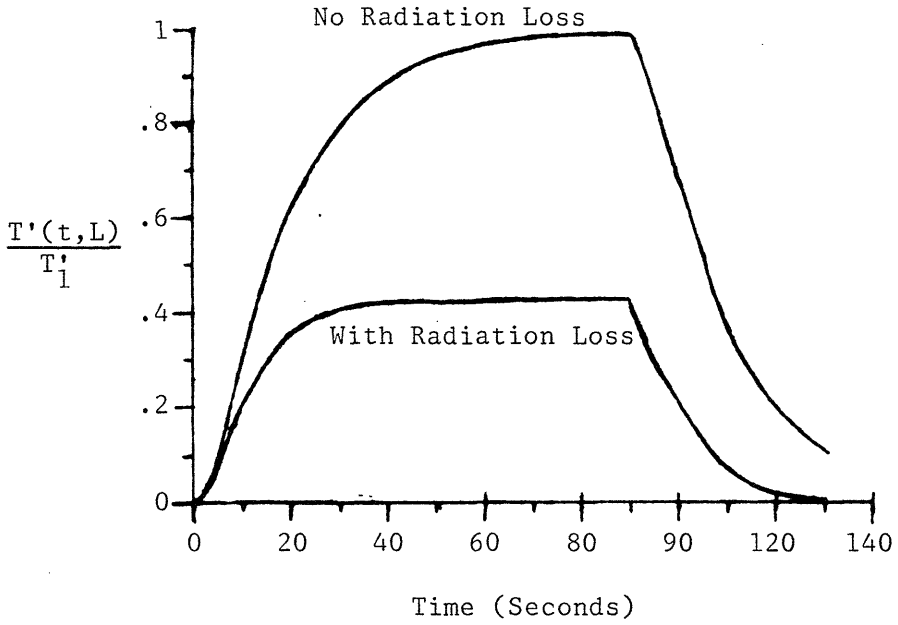

Figure C1 Normalized Temperature Pulse at End of Tube

derivative of $T'(L)$ with T_{bk}

$$\frac{\partial T'(L)}{\partial T_{bk}} = \frac{-1}{\cosh(aT_{bk}^{3/2})} - \frac{(T_m - T_{bk})\frac{3}{2}T_{bk}^{1/2}}{\cosh^2(aT_{bk}^{3/2})} \sinh(-aT_{bk}^{3/2})$$

where a is a constant. Clearly as T_{bk} grows larger (the jump at the lower thermocouple becomes less) the value of the jump represented by $T'(L)$ does as well.

References

C1. Bateman, Harry and Staff of the Bateman Manuscript Project, *Tables of Integral Transforms, Vol. 1.* McGraw Hill Book Company, New York, 1954.

C2. Touloukian, Y.S., *Thermophysical Properties of High Temperature Solid Materials, Vol. 1.* Elements, Macmillan Co., New York, 1967.